

**Journal of
Mechanics of
Materials and Structures**

Volume 8, No. 1

January 2013



JOURNAL OF MECHANICS OF MATERIALS AND STRUCTURES

msp.org/jomms

Founded by Charles R. Steele and Marie-Louise Steele

EDITORS

CHARLES R. STEELE Stanford University, USA
DAVIDE BIGONI University of Trento, Italy
IWONA JASIUK University of Illinois at Urbana-Champaign, USA
YASUHIRO SHINDO Tohoku University, Japan

EDITORIAL BOARD

H. D. BUI École Polytechnique, France
J. P. CARTER University of Sydney, Australia
R. M. CHRISTENSEN Stanford University, USA
G. M. L. GLADWELL University of Waterloo, Canada
D. H. HODGES Georgia Institute of Technology, USA
J. HUTCHINSON Harvard University, USA
C. HWU National Cheng Kung University, Taiwan
B. L. KARIHALOO University of Wales, UK
Y. Y. KIM Seoul National University, Republic of Korea
Z. MROZ Academy of Science, Poland
D. PAMPLONA Universidade Católica do Rio de Janeiro, Brazil
M. B. RUBIN Technion, Haifa, Israel
A. N. SHUPIKOV Ukrainian Academy of Sciences, Ukraine
T. TARNAI University Budapest, Hungary
F. Y. M. WAN University of California, Irvine, USA
P. WRIGGERS Universität Hannover, Germany
W. YANG Tsinghua University, China
F. ZIEGLER Technische Universität Wien, Austria

PRODUCTION production@msp.org

SILVIO LEVY Scientific Editor


Cover photo: Ev Shafir

See msp.org/jomms for submission guidelines.

JoMMS (ISSN 1559-3959) at Mathematical Sciences Publishers, 798 Evans Hall #6840, c/o University of California, Berkeley, CA 94720-3840, is published in 10 issues a year. The subscription price for 2013 is US\$555/year for the electronic version, and \$705/year (+\$60, if shipping outside the US) for print and electronic. Subscriptions, requests for back issues, and changes of address should be sent to MSP.

JoMMS peer-review and production is managed by EditFLOW® from Mathematical Sciences Publishers.

PUBLISHED BY

 **mathematical sciences publishers**

nonprofit scientific publishing

<http://msp.org/>

© 2013 Mathematical Sciences Publishers

NUMERICAL AND EXPERIMENTAL INVESTIGATION OF THE DYNAMIC CHARACTERISTICS OF CABLE-SUPPORTED BARREL VAULT STRUCTURES

SUN GUO-JUN, CHEN ZHI-HUA AND RICHARD W. LONGMAN

The cable-supported barrel vault (CSBV) structure system is a new style hybrid spatial steel structure, based on beam string structures (or truss string structures) and cylindrical latticed shell structures. A numerical investigation of the dynamic characteristics of a CSBV structure is presented, and an experimental test was created to validate the model's ability to obtain good predictions of the dynamic behavior. In order to simulate the construction process of a CSBV structure, the numerical investigation progresses in three phases: the first phase models the barrel vault without struts and cables, the second includes the influence of the cables, and the third introduces the added mass of a roof. The first nine vibration modes were obtained. The cables and struts in the CSBV improve the seismic behavior. The experimental results validate the numerical model, allowing us to study the influence of the rise-span and sag-span ratios.

1. Introduction

The cable-supported barrel vault (CSBV) is a new type of space structure that introduces tensegrity into thick double-layer or multilayer barrel vaults [Chen et al. 2008], as shown in Figure 1. It is composed of a single-layer or thin double-layer barrel vault, with struts and cables. On the one hand, due to the action of struts and cables, the rigidity of the whole structure is improved, as is the out-of-plane stability of the structure. Therefore, producing large spans is facilitated. On the other hand, by adopting the single-layer or the thin double-layer barrel vault, less steel is used, reducing costs. The difficulty of construction is also reduced, and the horizontal arch thrust is effectively reduced by the prestressed cables, so the heavy burden on the lower structures supporting the barrel vault is substantially reduced.

At present, the static and dynamic performance of barrel vault structures has been studied [Dong and Yao 1994; Wang and Li 1999; Langbecker and Albermani 2001; He et al. 2004; Cao et al. 2009; Kumagai et al. 2009], but only the static performance has been addressed [Chen et al. 2010]. The dynamic response of a cable-supported structure under dynamic loads, such as wind, earthquakes, or traffic, is very complex and requires special study. The dynamic characteristics of cable-supported spherical shells have been studied experimentally in [Tatemichi et al. 1997; Chen et al. 2004; Zhang et al. 2007]. The structural response under dynamic loads not only depends on the load, but also on the dynamic characteristics of the structure. The natural frequency of vibration is extremely significant, as it influences directly the

Chen Zhi-hua is the corresponding author.

Special appreciation is due to every student in the steel research group of Tianjin University for their assistance with the laboratory work. This work is sponsored by the Program for New Century Excellent Talents in University of the Ministry of Education of China (grant no. NCET-06-0228) and the National Natural Science Foundation of China (no. 50778122).

Keywords: cable-supported barrel vault, dynamic characteristics, natural frequency, rise-span ratio, sag-span ratio.

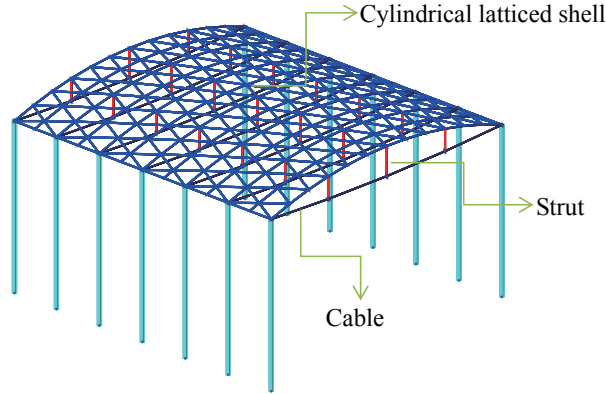


Figure 1. Cable-supported barrel vault (CSBV) structure.

dynamic response of the structure. Therefore, for CSBV structures, the natural frequencies of vibration and the mode shapes need further study. In this paper, a model of a CSBV structure was designed, and the natural frequencies of vibration and the mode shapes were found by numerical analysis followed by experiments on a test facility created for this purpose. The results of the numerical analysis and experiments are analyzed and compared. A parametric study of the dynamic characteristics of the CSBV structure was also conducted. From the numerical and experimental results, some conclusions are drawn for practical engineering applications.

2. Numerical model

For this paper, the cable-supported barrel vault (CSBV) structure shown in [Figure 2](#) was designed. It has a span of 3.333 m, length of 3.587 m, rise of 0.3 m, and sag of 0.05 m. The upper barrel vault model is composed of three kinds of steel tube sections, $\varnothing 8 \times 1$, $\varnothing 10 \times 1$, and $\varnothing 12 \times 1$. The sections of all struts are steel tube $\varnothing 12 \times 1$. The cables are all steel bar $\varnothing 6$. The sections of the columns are all steel tube 50×2 with a length of 2.1 m. All the steel tubes are Q235B and the steel bar's ultimate strength is 1860 MPa. The design of the cable-supported structure is different from other steel structures not only in that the sections are modified, but also because of the need to determine the cable force. Some

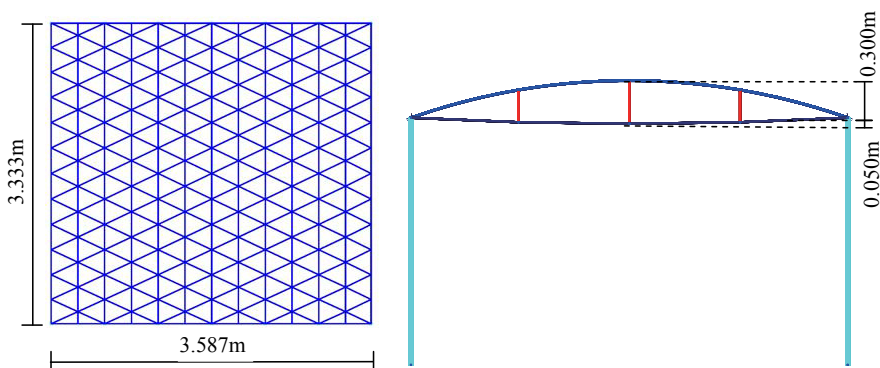


Figure 2. Elevation drawing and plane graph.

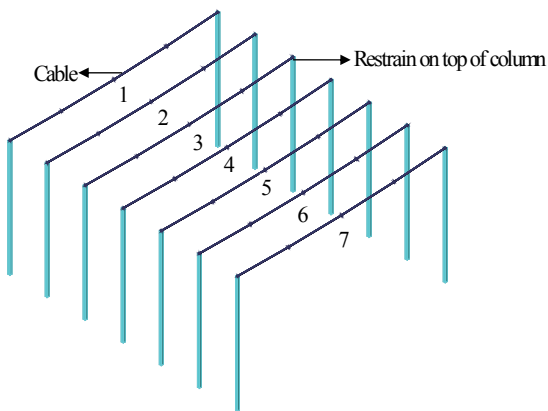


Figure 3. Cable numbering.

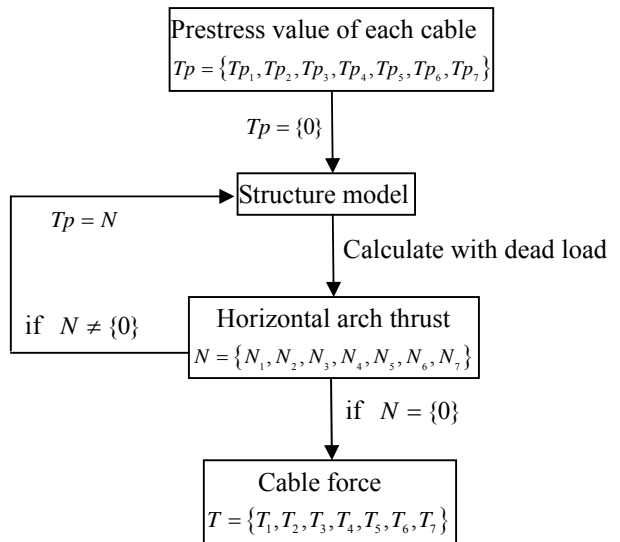


Figure 4. Iteration flow chart.

design principles and optimizations of cable-supported structures have been presented in the literature [Kawaguchi et al. 1999; Kang et al. 2003; Chen and Li 2005; Xue and Liu 2009].

In this paper, the cable prestress design principle for CSBV structures, in which the peripheral restriction is usually the spatial pin, is that the horizontal arch thrust is zero. Figure 3 labels the seven cables in the CSBV, and the cable prestress is set to zero, $Tp = \{Tp_1, Tp_2, Tp_3, Tp_4, Tp_5, Tp_6, Tp_7\} = \{0\}$. Being subjected to the dead weight of the structure, the horizontal arch thrusts can be calculated, and are denoted by $N = \{N_1, N_2, N_3, N_4, N_5, N_6, N_7\}$. Then, the structure is reanalyzed; this time N is considered to be the cable force, and is applied on each cable correspondingly, and the horizontal arch thrust is recalculated. This process is repeated until the horizontal arch thrust is zero or close to zero, resulting in the target values of the cable prestress, $T = \{T_1, T_2, T_3, T_4, T_5, T_6, T_7\}$. It should be noted that the nonlinearity of the geometry of the structure must be considered in the calculation process above. The computation can be accomplished using general finite element analysis software such as ANSYS. The iteration calculation flow chart is shown in Figure 4. The iterative process for the research model (see Figure 2) converged within three iteration steps; see Figure 5.

3. Numerical analysis

Following the finite element software package ANSYS 12.0 user manual [ANSYS 2010], the element BEAM188 was adopted to simulate the steel members in the upper vault structure, while the struts and the cables were simulated by LINK8 and LINK10, respectively. The finite element model of the CSBV is shown in Figure 6. The subspace iteration method [Jung et al. 1999] for the dynamic characteristic was used. The research process can be divided into three phases: in the first phase the barrel vault without struts and cables is modeled; in the second, the CSBV structure is modeled; and in the third, the CSBV structure is modeled, with an added mass of 15 kg to simulate the case with a roof. The added mass distribution is shown in Figure 7. The difference in rigidity between the barrel vault and

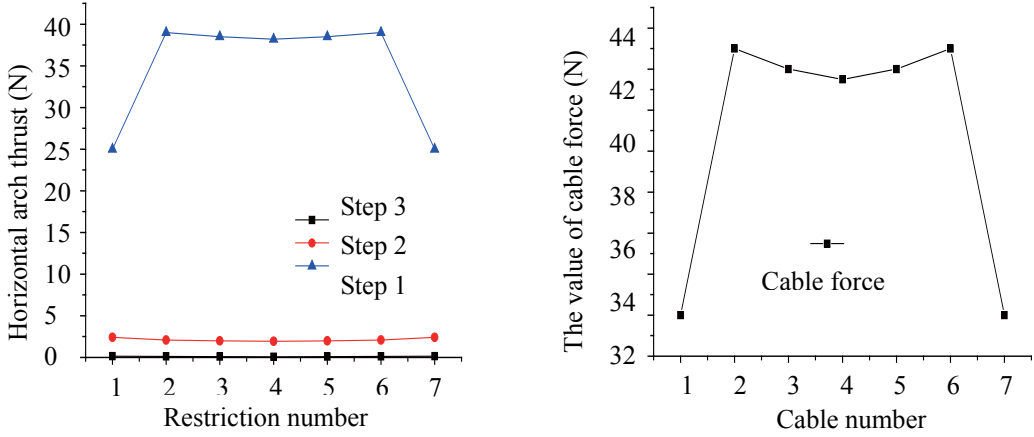


Figure 5. Values of cable forces: three iterations to convergence (left), and final values (right).

CSBV structures can be obtained from the first and second phases. The difference in rigidity between the construction and operational phases can be obtained from the second and third phases.

The first nine mode frequencies for each phase of the above numerical analysis are shown in [Table 1](#) and the corresponding mode shapes for each phase are shown in [Figures 8–10](#). Comparing the first and second phases, the frequencies of the CSBV are higher than those of the barrel vault structure, that is, the rigidity of the CSBV structure is greater than that of the barrel vault structure. Comparing the second

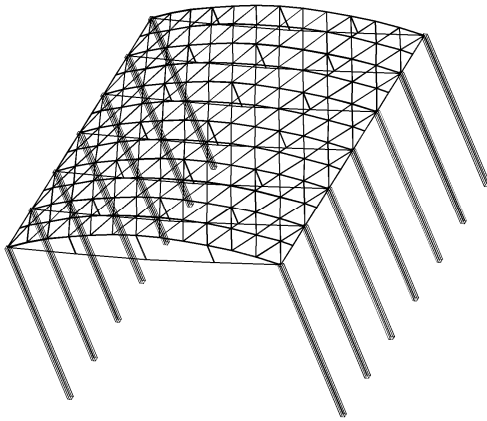


Figure 6. Finite element model of the CSBV.

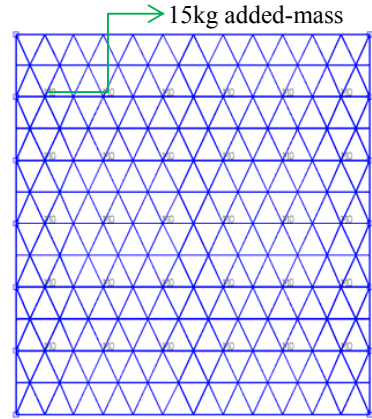


Figure 7. Added mass distribution.

Mode number	1	2	3	4	5	6	7	8	9
First phase	6.33	7.24	8.88	10.10	10.98	13.01	14.21	25.25	26.81
Second phase	8.72	11.27	13.62	14.35	15.83	24.82	26.05	28.43	33.26
Third phase	2.44	3.03	3.41	3.81	4.76	4.94	5.68	7.04	7.38

Table 1. The first nine mode frequencies, in Hz, for each phase of the analysis.

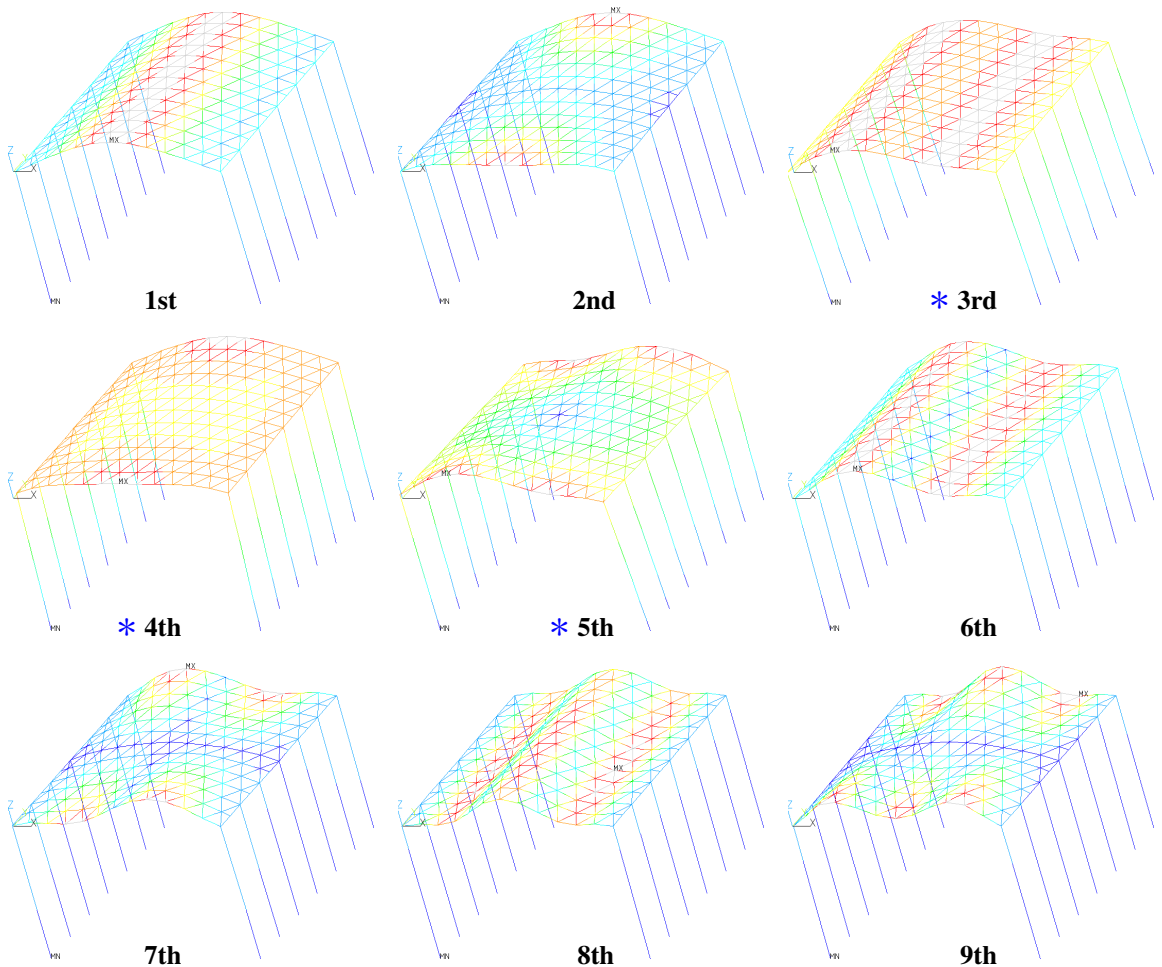


Figure 8. Mode shapes of the first nine mode frequencies for the first phase.

and third phases, with the CSBV having added mass, the frequency of the CSBV is reduced. It can be observed from the mode shapes for each phase that each mode involves vibration of the whole structure, and is not a local mode. The barrel vault structure vibrates with smaller wave numbers than the CSBV, because of the cables and struts. In the first phase, the natural vibration property of the barrel vault is not only related to the roof, but also the stiffness of the bottom structure, as illustrated in the 3rd to 5th modes in Figure 8, marked with *. The same conclusion applies to the parts of Figures 9 and 10 marked with *. This indicates that global analysis is necessary for the CSBV.

4. Experimental work

Test model. In order to validate the above numerical modeling of CSBV structures, an experimental test facility was created. All the bars of the upper barrel vault in Figure 1 were connected with welded hollow pipe joints. The ends of the upper barrel vault were welded to the tops of the columns. The tops of the

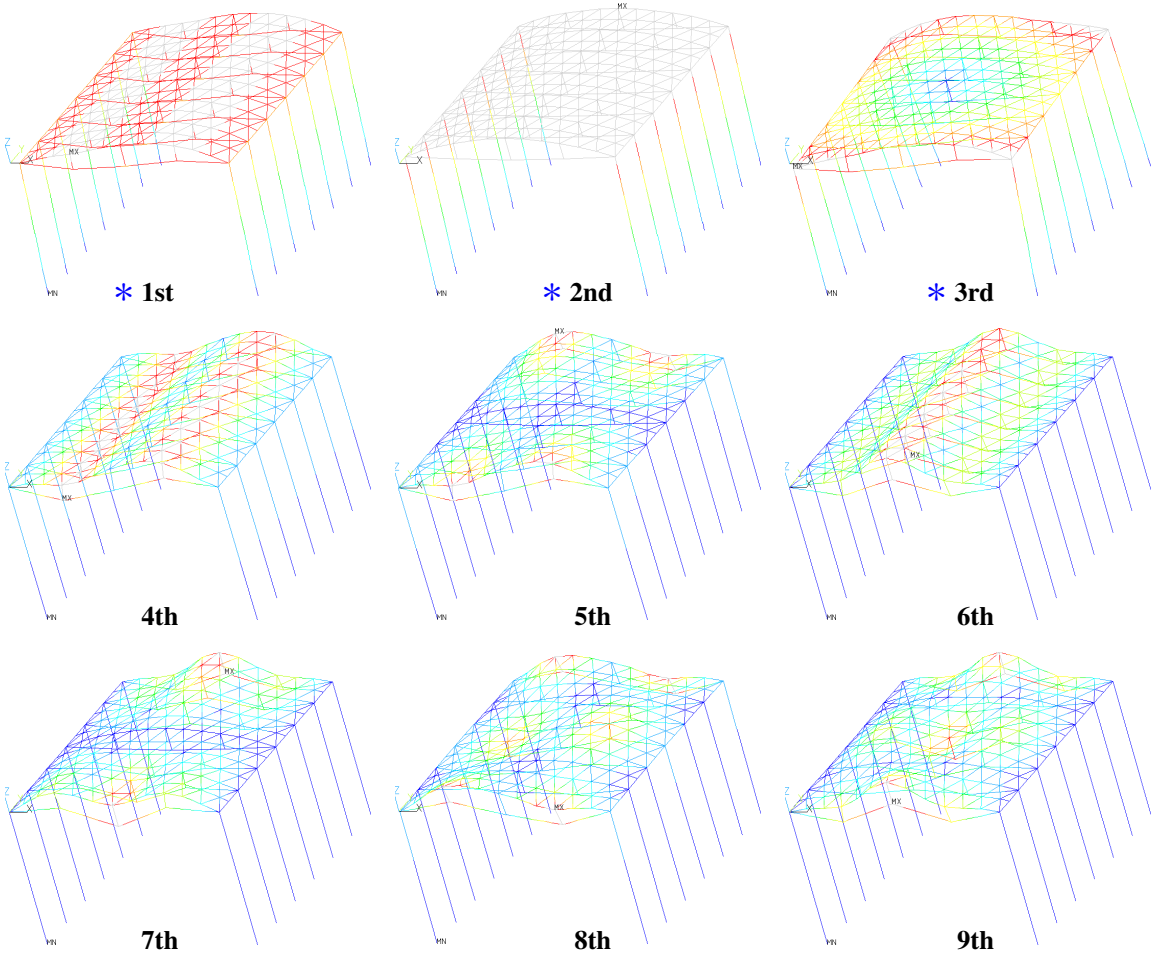


Figure 9. Mode shapes of the first nine mode frequencies for the second phase. (See page 7 for the asterisks.)

struts were connected to the upper barrel vault with one-way hinge bolt joints. The cable groove was used as a connection at the bottom end of the struts while bolts were adopted to link the end of the cable with the top of column. By twisting the bolts, the cable forces could be adjusted to the design values mentioned above. Then the cables were fixed by cable buttons on each side of the struts to avoid slipping.

Test program. The purpose of the test was to obtain the fundamental natural frequencies and vibration modes. In order to avoid wind disturbances, the model was tested in a tent. Vibration data was generated by applying impacts to the structure to obtain the frequency response function. Piezoelectric acceleration sensors were used to collect data at chosen measurement points. There were three phases of experimental tests. In the first phase, 35 measurement locations were chosen on the structure so that accurate mode parameters could be obtained. In the second and third phases, 56 measurement points were chosen to obtain accurate mode parameters. The chosen locations are shown in [Figure 11](#). Because the stiffness

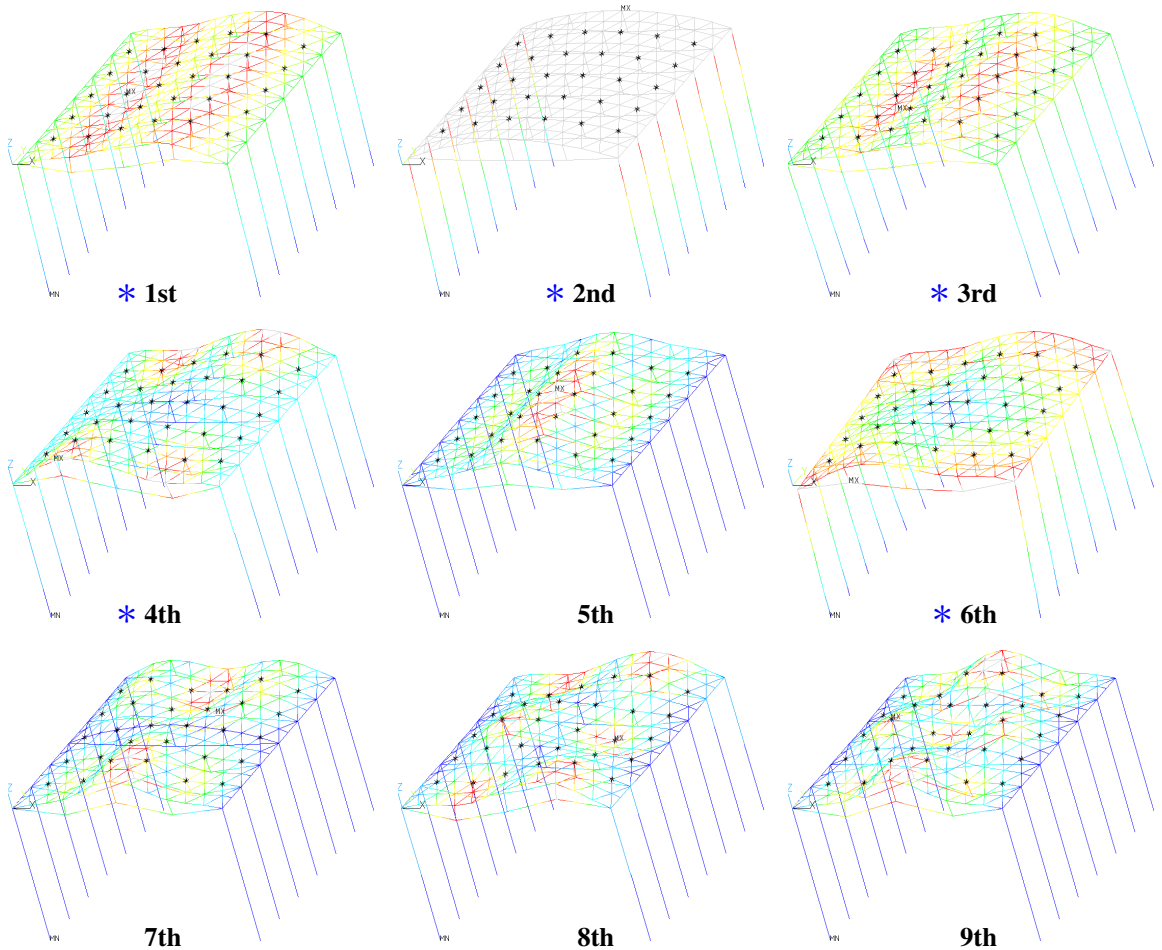


Figure 10. Mode shapes of the first nine mode frequencies for the third phase. (See page 7 for the asterisks.)

at different locations can differ greatly, impulses were applied at one corner of the structure, and the responses at multiple locations were recorded. The force applied by the force hammer was recorded using the piezoelectric force sensor in the hammer. The piezoelectric acceleration sensors gave three-axis acceleration information at each measurement point. The piezoelectric force and acceleration signals were amplified and passed through an antialiasing low-pass filter, and were stored in a data acquisition and signal processing (DASP) system. Figure 12 shows the signal-collection process.

To ensure that the test data were accurate and reliable, pretests were conducted as follows:

- (1) The linearity of the test object was evaluated by applying different impacts.
- (2) Appropriate sample rates were chosen for the impact force signal and for the accelerometer sensor signals in order to obtain good-fidelity information.

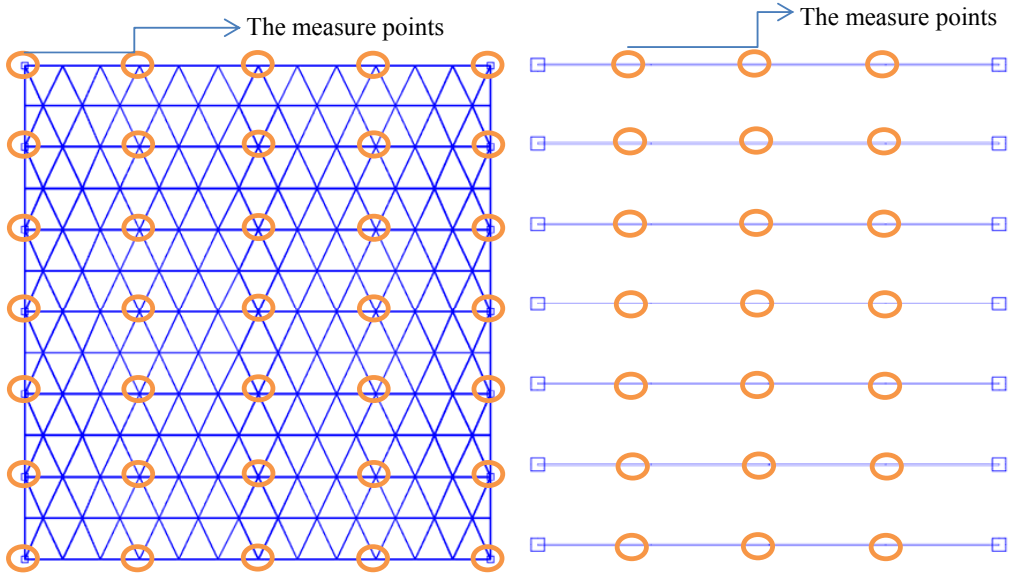


Figure 11. Accelerometer sensor locations (measurement points) on the barrel vault (left) and along the cables (right).

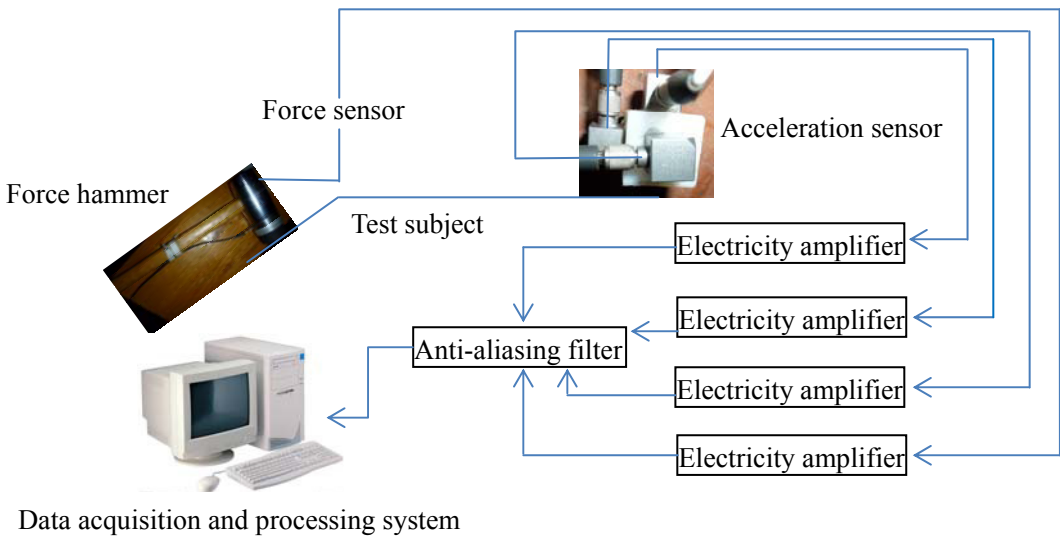


Figure 12. Data-collection hardware configuration.

- (3) The symmetry of the matrix of frequency response functions was tested by interchanging the points of the input impact and the resulting response.
- (4) Tests were conducted to determine the best location for applying the impulse input. It was determined that a top corner of the structure gave the best excitation of modes, amplitude responses, and signal-to-noise ratio, as shown in [Figure 13](#).

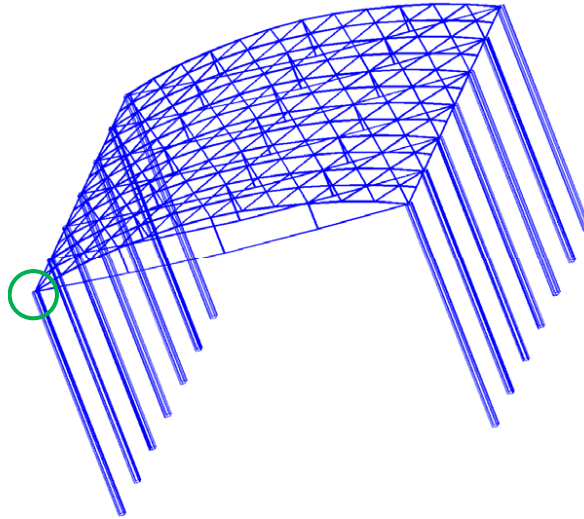


Figure 13. Location of impact using the force hammer (circled).

The bandwidth of the formal test is 100 Hz. Fast Fourier transforms were used on the impact force signal and acceleration response signals to obtain the frequency response functions. The “set total average” and “point spread function” in the DASP modal analysis software were used to identify the mode frequencies and shapes. By comparing the modal fits, the mode of vibration was obtained by the mass-normalized method.

Test results. The test research contents can be divided into three phases: first, the barrel vault (without struts and cables); second, the CSBV structure; and third, the CSBV structure with added masses of 15 kg to simulate the roof. Experimental and numerical values of the natural frequencies for each phase can be compared in [Table 2](#).

The vibration mode shapes of the CSBV are close to each other and their vibration directions are mainly in the vertical direction. The mode shapes are mostly symmetric or antisymmetric. The vibration mode shows a trend of the symmetry number increasing as the modal order increases. The frequency spectrum is very concentrated, making the dynamic characteristics of the CSBV extremely complex. Furthermore, the rigidity of the CSBV is greater than that of the traditional shell structure. Due to the existence of the cable and strut, the vibration modes of the CSBV are changed and the seismic behavior is improved. The dynamic analysis models, used during the process of seismic analysis of the three stages of construction and forming, have greater differences. The changes in the dynamic response of the structure in the construction process cannot be neglected.

5. Parameters research

The finite element model of the CSBV from before is used in the following subsections to study the influence of rise-span ratio and sag-span ratio.

Influence of rise-span ratio. The rise-span ratio used above was 1/100. The influence of the rise-span ratio on the mode frequencies of the structure was analyzed by considering two additional ratios, 1/50

First phase			Second phase			Third phase		
Mode number	Test result	Numerical result	Mode number	Test result	Numerical result	Mode number	Test result	Numerical result
1	6.78	6.33	1	8.87	8.72	1	3.12	2.44
2	7.42	7.24	2	12.12	11.27	2	3.68	3.03
3	8.97	8.88	3	14.02	13.62	3	4.24	3.41
4	10.68	10.1	4	14.29	14.35	4	4.67	3.81
5	11.26	10.98	5	15.62	15.83	5	5.28	4.76
6	13.36	13.01	6	23.43	24.82	6	5.93	4.94
7	14.53	14.21	7	25.42	26.05	7	6.79	5.68
8	25.49	25.25	8	27.43	28.43	8	8.11	7.04
9	27.28	26.81	9	32.14	33.26	9	8.45	7.38

Table 2. Comparison between the experimental and numerical values, in Hz, for natural frequencies. “First phase” refers to the barrel vault without struts and cables; “second phase” to the CSBV structure; and “third phase” to, the CSBV structure with added masses of 15 kg to simulate the roof.

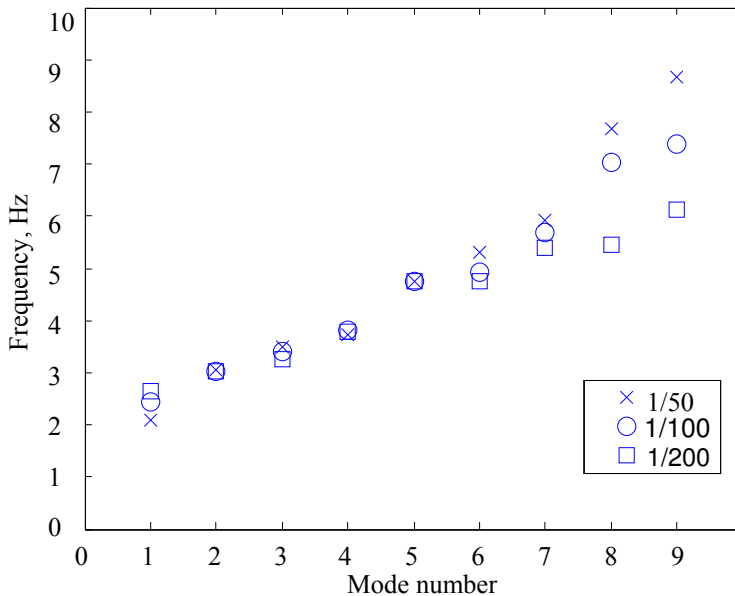


Figure 14. Influence of rise-span ratio on the natural frequency of the CSBV.

and 1/200. The modified models were subjected to an added mass to simulate the third phase. The natural frequency results are shown in Figure 14.

The natural frequency of the CSBV decreases as the rise-span ratio decreases, while the period increases as the rise-span ratio decreases. The variation in the natural frequency is small for small order numbers and becomes larger as the order number increases.

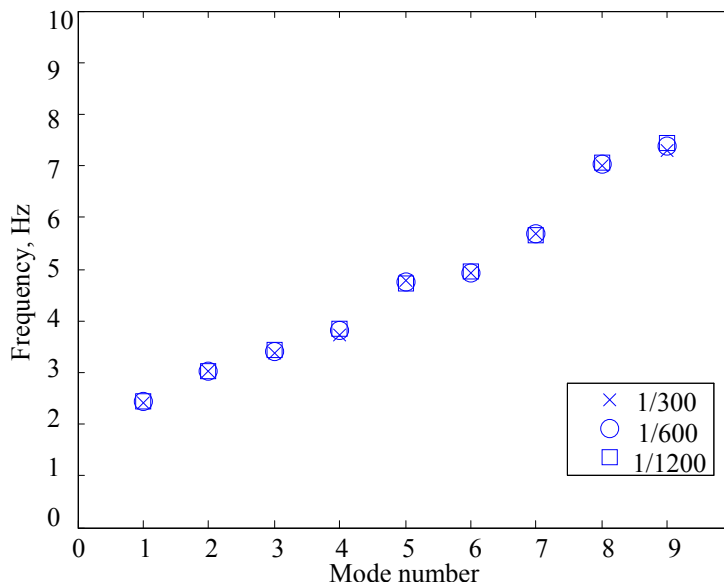


Figure 15. Influence of sag-span ratio on the natural frequencies of the CSBV.

Influence of sag-span ratio. The sag-span ratio used above was 1/600. The influence of the sag-span ratio on the mode frequencies of the structure was analyzed by considering two additional ratios, 1/300 and 1/1200. The modified models were subjected to an added mass to simulate the third phase. The natural frequency results are shown in [Figure 15](#).

The natural frequency of the CSBV increases as the sag-span ratio decreases, while the period decreases as the sag-span ratio decreases. However, the natural frequency does not change significantly as the sag-span ratio changes.

6. Conclusions

The cable-supported barrel vault (CSBV) structure, based on beam string structures (or truss string structures) and cylindrical latticed shell structures, is a new-style hybrid spatial steel structure. The design of the cable-supported structure is different from other steel structures. The process of designing the cable-supported structure is complicated and includes section design and cable-force determination. In this paper, a finite element model of the CSBV with the cable force determined by an iterative calculation was created. In order to simulate the construction process of a CSBV structure, the research was divided into three phases: the first phase considered the barrel vault without struts and cables, the second the CSBV structure, and the third the CSBV structure with added mass to simulate the influence of a roof, considered here to consist of 30 added masses of 15 kg each. Research was conducted using numerical investigation by generating a finite element model, and a CSBV structure was created for experimental verification of the finite element results.

The mode shapes of the CSBV structure are similar, mostly symmetric and antisymmetric, and their vibrations are mostly in the vertical direction. The frequency spectrum is concentrated, creating dynamic characteristics that are very complex. The vibration modes show a trend of the symmetry number

increasing as the modal order increasing. The rigidity of the CSBV is greater than that of the traditional shell structure, and the cables and struts change the vibration modes and improve the seismic behavior. The changes in the dynamic response of the structure in the construction process cannot be neglected. The vibration modes of the CSBV are influenced by the roof, as well as by the stiffness of the bottom structure, indicating that global analysis is necessary.

From investigation of the influence of rise-span and sag-span ratios we make the following conclusions: the natural frequencies of the CSBV decrease with the increase of the rise-span ratio, while the period increases with the increase of the rise-span ratio. The variation in the natural frequency is small for small order numbers and becomes larger as the order number increases. The natural frequency of the CSBV increases as the sag-span ratio decreases, while the period decreases as the sag-span ratio decreases. However, the natural frequency is not significantly changed as the sag-span ratio changes.

References

- [ANSYS 2010] *ANSYS 12.0 users' manual*, Swanson Analysis Systems, 2010.
- [Cao et al. 2009] Z.-G. Cao, F. Fan, Y. Sun, and H.-H. Ma, “Elasto-plastic stability of single-layer cylindrical reticulated shells”, pp. 1832–1840 in *Evolution and trends in design, analysis and construction of shell and spatial structures: 50th Anniversary Symposium of the IASS* (Valencia, 2009), edited by A. Domingo and C. Lazaro, Editorial de la Universitat Politècnica de Valencia, Valencia, 2009.
- [Chen and Li 2005] Z.-H. Chen and Y. Li, “Parameter analysis on stability of a suspendedome”, *Int. J. Space Struct.* **20**:2 (2005), 115–124.
- [Chen et al. 2004] Z.-H. Chen, Y. Guo, and Y. Li, “Experimental research and analysis of the prestress and dynamic behavior for suspendedome structure system”, *Build. Struct.* **34**:5 (2004), 42–45. In Chinese.
- [Chen et al. 2008] Z.-H. Chen, X.-Y. Yan, W.-T. Qiao, X.-L. Liu, Z.-X. Sun, Q. Li, J. Meng, and X.-Y. Tang, “Structure system of cable supported barrel vault structure”, patent ZL200810053722.8, China, 2008, <http://www.soopat.com/Patent/200810053722>. In Chinese.
- [Chen et al. 2010] Z.-H. Chen, W.-T. Qiao, and X.-Y. Yan, “Cable supported barrel vault structure system and research on mechanics feature”, *Adv. Steel Constr.* (IJASC, ISSN 1816-112X) **6**:3 (2010), 867–878.
- [Dong and Yao 1994] S.-L. Dong and J. Yao, “The future and prospect of latticed shell structures”, *Spat. Struct.* **1**:1 (1994), 3–10. In Chinese.
- [He et al. 2004] Y.-J. He, X.-H. Zhou, and S.-L. Dong, “Research on static and stability properties of single layer latticed intersected cylindrical shell”, *J. Hunan Univ. (Nat. Sci.)* **31**:4 (2004), 45–50. In Chinese.
- [Jung et al. 1999] H.-J. Jung, M.-C. Kim, and I.-W. Lee, “An improved subspace iteration method with shifting”, *Comput. Struct.* **70**:6 (1999), 625–633.
- [Kang et al. 2003] W.-J. Kang, Z.-H. Chen, H.-F. Lam, and C.-R. Zuo, “Analysis and design of the general and outmost-ring stiffed suspen-dome structures”, *Eng. Struct.* **25**:13 (2003), 1685–1695.
- [Kawaguchi et al. 1999] M. Kawaguchi, M. Abe, and I. Tatemichi, “Design, tests and realization of ‘susten-dome’ system”, *J. IASS* **40**:3/131 (1999), 179–192.
- [Kumagai et al. 2009] T. Kumagai, T. Takeuchi, and I. Suzuki, “Dynamic responses of cylindrical lattice shell roofs under horizontal earthquake motions with arbitrary direction by shaking table tests”, pp. 409–419 in *Evolution and trends in design, analysis and construction of shell and spatial structures: 50th Anniversary Symposium of the IASS* (Valencia, 2009), edited by A. Domingo and C. Lazaro, Editorial de la Universitat Politècnica de Valencia, Valencia, 2009.
- [Langbecker and Albermani 2001] T. Langbecker and F. Albermani, “Kinematic and non-linear analysis of foldable barrel vaults”, *Eng. Struct.* **23**:2 (2001), 158–171.
- [Tatemichi et al. 1997] I. Tatemichi, T. Hatato, and Y. Anma, “Vibration tests on a full-size suspen-dome structure”, *Int. J. Space Struct.* **12**:31 (1997), 143–161.

- [Wang and Li 1999] B.-B. Wang and Y.-Y. Li, “A theoretical study of super-span latticed shells”, *J. Constr. Steel Res.* **51**:3 (1999), 287–296.
- [Xue and Liu 2009] W.-C. Xue and S. Liu, “Design optimization and experimental study on beam string structures”, *J. Constr. Steel Res.* **65**:1 (2009), 70–80.
- [Zhang et al. 2007] A.-L. Zhang, D.-M. Wang, and X.-C. Liu, “Dynamic performance experiment and theoretical analysis on the suspend-dome structure model of the badminton gymnasium for 2008 Olympic Games”, *J. Build. Struct.* **28**:6 (2007), 68–75. In Chinese.

Received 10 Mar 2012. Revised 25 Oct 2012. Accepted 30 Oct 2012.

SUN GUO-JUN: sungj.tju@hotmail.com

School of Civil Engineering, Tianjin University, 92 Weijin Road, Tianjin, 300072, China

CHEN ZHI-HUA: zhchen@tju.edu.cn

School of Civil Engineering, Tianjin University, 92 Weijin Road, Tianjin, 300072, China

RICHARD W. LONGMAN: rw14@columbia.edu

Department of Mechanical Engineering, Columbia University, 500 W 120th St., Mudd 220, New York, NY 10027, United States

WHEN BEAM THEORIES FAIL

PAUL R. HEYLIGER

The free vibration of completely unrestrained prismatic rectangular parallelepipeds and the static response of planar elastic rectangles under transverse loads are examined to determine the relative accuracy of several widely used beam theories. The Euler–Bernoulli, Rayleigh, and Timoshenko theories are applied to both isotropic and orthotropic beams and compared with elasticity-based solutions. The resulting frequencies, energies, displacements, and stresses are compared with solutions to the linear theory of elasticity for solids with the same geometries and material constitutions. Sources of the resulting differences in response are identified, and guidelines are suggested.

Introduction

The vibrating beam is one of the most studied problems in mechanics, having an extremely large number of practical applications [Timoshenko 1921; 1922; 1953; Love 1927; Anderson 1953; Traill-Nash and Collar 1953; Dolph 1954; Herrmann 1955; Huang 1961; Cooper 1966; Thomas and Abbas 1975; Abbas and Thomas 1977; Stephen 1978; 2001; Levinson 1981; King 1985; Schramm et al. 1994; Han et al. 1999; Gruttmann and Wagner 2001; Hutchinson 2001; Puchegger et al. 2003; 2005]. One of the key issues encountered when considering this problem is the loss in relative accuracy when moving from a fully three-dimensional elasticity theory to the simpler one-dimensional beam theories commonly used by most engineers. In general, the complexity of the displacement field in the beam increases as the slenderness ratio (s) of the beam decreases, where $s = L\sqrt{A/I}$, and L , A , and I represent the beam length, area of the cross-section, and second moment of the cross-sectional area, respectively. Similar behavior is found in static response for beams under a variety of loading and boundary conditions.

The most widely used beam theories in modern applications were all developed by 1921. These are the Euler–Bernoulli, Rayleigh, and Timoshenko beam theories. The excellent review of these theories (along with a rarely used shear beam model) in [Han et al. 1999] completely describes these basic theories and their behaviors under a variety of boundary conditions. There is fairly broad consensus that if the slenderness ratio is large, with the value of $s \geq 100$ used by Han and coworkers being typical, that Euler–Bernoulli theory can be used but when the slenderness ratio is “small”, shear deformation models may give more accuracy.

One issue that has seen little exploration during these investigations is at what point the beam ceases to behave as such and the estimates provided by one-dimensional beam theories begin to fail. To take an extreme case, a rectangular parallelepiped with a square cross-section of sides a and length L has a slenderness ratio of $\sqrt{12}(L/a)$. For larger L/a ratios, the parallelepiped deforms according to the kinematic hypothesis consistent with Euler–Bernoulli theory, then transitions into deformation patterns

Funding from the Mountains Plains Consortium is gratefully acknowledged.

Keywords: beam, vibration, elasticity, frequency, Timoshenko, Euler–Bernoulli.

consistent with shear deformation models well represented by Timoshenko theory. But at some point, even the Timoshenko model has limitations, as L approaches and eventually takes a value less than a . What was once a beam becomes a thin square plate with thickness L and side edge lengths of a , with completely different behavior.

In this study, elasticity theory is used to determine the limits of beam-theory accuracy as the slenderness ratio decreases for both dynamic and static responses. This is accomplished first by comparing the frequency and modal displacement results from three commonly used beam theories (Euler–Bernoulli, Rayleigh, and Timoshenko) with those of approximate solutions to the equations of motion for linear elasticity for the same solid. Specific attention is paid to the simplest possible set of boundary conditions (from an elasticity perspective): the free-free beam. This translates to the problem of zero end shear and moment for the beam theories and traction-free vibration for a three-dimensional solid, and allows a direct comparison for determining, at least in part, when beam theories fail to capture the mechanics of deformation in these solids. Second, the static response of a beam under transverse sinusoidal loading is considered using beam theories and an exact linear elasticity solution. In both cases, the objective is to provide estimates of the errors induced by various beam theory approximations as the slenderness ratio decreases.

Theoretical foundation

Governing equations. For a three-dimensional solid, there are three displacement components: $u_1(x_1, x_2, x_3)$, $u_2(x_1, x_2, x_3)$, and $u_3(x_1, x_2, x_3)$. They are linked to components of infinitesimal strain via the relations

$$\epsilon_{ij} = \frac{1}{2} \left(\frac{\partial u_i}{\partial x_j} + \frac{\partial u_j}{\partial x_i} \right). \quad (1)$$

Here ϵ_{ij} are the components of the infinitesimal strain tensor and u_i represent the displacement components in indicial form. These strains are related to the components of Cauchy stress via the generalized Hooke's law, given by

$$\sigma_{ij} = C_{ijkl} \epsilon_{kl}, \quad (2)$$

where C_{ijkl} represent the components of the elastic stiffness tensor. Substituting these stresses into the equations of motion

$$\sigma_{ij,j} = \rho \frac{\partial^2 u_i}{\partial t^2} \quad (3)$$

allows for a direct representation of these equations in terms of the three displacement variables.

An alternative to a direct solution of the equations of equilibrium uses Hamilton's principle as a starting point for approximate solutions to the equations of motion. For the case of zero body force, this can be written

$$0 = - \int_0^t \int_V \{ \sigma_{11} \delta \epsilon_{11} + \sigma_{22} \delta \epsilon_{22} + \sigma_{33} \delta \epsilon_{33} + 2\sigma_{23} \delta \epsilon_{23} + 2\sigma_{13} \delta \epsilon_{13} + 2\sigma_{12} \delta \epsilon_{12} \} dV dt \\ + \delta \int_0^t \int_S t_i \delta u_i dS + \frac{1}{2} \delta \int_0^t \int_V \rho (\dot{u}_1^2 + \dot{u}_2^2 + \dot{u}_3^2) dV dt. \quad (4)$$

Here V is the volume of the solid, $\dot{u} = \partial u / \partial t$, t represents time, ρ is the density of the material, t_i are the specified surface tractions, and δ is the variational operator.

Beam theory displacement fields. The general procedure for simplifying computational models in the field of solid mechanics is to restrict the way that a general particle within the solid can deform by imposing kinematic constraints through an assumed displacement field. This can take a variety of forms, but the general intent in beam, plate, and shell theories is to reduce the dimensions of the problem and thereby simplify the subsequent analysis. In this study, each of the models used (the three beam theories and the three-dimensional elasticity solution) imposes a sequence of constraints represented in the resulting displacement fields. In the discussion that follows, the standard notations of $u_1 = u$, $u_2 = v$, and $u_3 = w$ and $x_1 = x$, $x_2 = y$, and $x_3 = z$ are both used because of clarity and common usage. The long axis of the beam is given by x and the cross-section coordinates are y in the out-of-plane direction and z in the transverse direction of the beam. Additionally, only displacement fields corresponding to bending action are considered in this study. There are of course types of beams in which the axial, torsional, and bending action are coupled [Hodges 2006; Marigo and Meunier 2006], but those cases are not considered here.

Euler–Bernoulli and Rayleigh beam theories. The Euler–Bernoulli beam is represented by a single unknown variable: the transverse displacement of the beam centroid $u_3 = w$. By further assuming that the Poisson’s ratio is zero, the displacement field can be given by

$$u_1(x_1, x_2, x_3) = u(x, y, z) = -z dw/dx, \quad (5)$$

$$u_2(x_1, x_2, x_3) = v(x, y, z) = 0, \quad (6)$$

$$u_3(x_1, x_2, x_3) = w(x, y, z) = w(x). \quad (7)$$

The only difference between the Euler–Bernoulli and Rayleigh beam theories is that in Euler–Bernoulli theory the kinetic energy associated with the u displacement component is neglected since \dot{u}^2 along the axis of the beam is generally much smaller in magnitude than \dot{w}^2 transverse to the beam axis. The equation of motion for the Euler–Bernoulli model with density ρ , elastic modulus E , moment of inertia I , and transverse loading $q(x, t)$ can be expressed in terms of w as

$$\frac{\partial^2}{\partial x^2} \left(EI \frac{\partial^2 w}{\partial x^2} \right) + \rho \frac{\partial^2 w}{\partial t^2} = q(x, t). \quad (8)$$

Timoshenko beam theory. Timoshenko beam theory [Timoshenko 1921; 1922], also sometimes referred to as a first-order shear deformation theory because it allows for nonzero transverse shear strain, is represented by two unknown functions that represent the transverse displacement (w) and the total section rotation (Ψ) of the beam cross-section:

$$u_1(x_1, x_2, x_3) = u(x, y, z) = z\Psi(x), \quad (9)$$

$$u_2(x_1, x_2, x_3) = v(x, y, z) = 0, \quad (10)$$

$$u_3(x_1, x_2, x_3) = w(x, y, z) = w(x). \quad (11)$$

Here again the Poisson’s ratio is assumed to be zero. There is a fourth beam theory, rarely used, termed

the shear theory, in which the kinetic energy associated with the displacement u is neglected. This theory is not considered in this study.

The respective displacement fields can be substituted into the strain-displacement relations and appropriate constitutive law, then the resulting displacement variables can be used in the equation(s) of motion

$$\rho A \frac{\partial^2 w}{\partial t^2} - q(x, t) = \frac{\partial}{\partial x} \left[\kappa A G \left(\frac{\partial w}{\partial x} - \Psi \right) \right], \quad (12)$$

$$\rho I \frac{\partial^2 \Psi}{\partial t^2} = \frac{\partial}{\partial x} \left(E I \frac{\partial \Psi}{\partial x} \right) + \kappa A G \left(\frac{\partial w}{\partial x} - \Psi \right), \quad (13)$$

where A is the cross-sectional area, κ is the shear correction coefficient, and G is the shear modulus. For the isotropic beam, the shear and elastic modulus are related. For the orthotropic beam, these constants are independent. In either case, these governing equations can then be solved using usual methods [Han et al. 1999].

Application and results

In this section, the displacement fields associated with beam theories and elasticity theory are applied to two fundamental problems: the free vibration of the completely unrestrained rectangular parallelepiped, and the static response of a simply supported rectangular strip under transverse load. The results obtained by various beam theories can be compared with three-dimensional elasticity theory in the first case and an exact plane elasticity solution in the second case.

Traction-free vibration of the free-free beam. Most of the analyses that use beam theory require use of dimensionless variables. For a beam of length L^* , area A^* , moment of inertia I^* , we can compute the dimensionless area $A = A^*/L^{*2}$, moment of inertia $I = I^*/L^{*4}$, density $\rho = \rho^* L^{*6} \omega_1^{*2}/(EI^*)$, and frequency $\omega_i = \omega_i^*/\omega_1^*$, where ω_i represents the i -th natural frequency of the beam in radians/second.

In terms of the three beam theories, the solution reduces to satisfaction of the equation(s) of motion along with the boundary conditions associated with zero resultant transverse shear and bending moment at the two ends. For the elasticity model, the weak form of the three equations of motion embedded within (4) must be solved for the case where the boundary conditions over the entire surface must be traction-free.

Euler–Bernoulli theory. The Euler–Bernoulli beam includes strain energy terms from axial strain and kinetic energy terms only from the transverse displacement component $w(x)$. The solution for the beam transverse displacement is given as [Han et al. 1999]

$$w(x) = C_1 \sin ax + C_2 \cos ax + C_3 \sinh ax + C_4 \cosh ax. \quad (14)$$

Here a is the dimensionless wave number that is related to the dimensionless density, area, and frequencies by

$$a^4 = \rho A \omega^2. \quad (15)$$

The end conditions consistent with the free-free beam for this theory are

$$\frac{d^3 w}{dx^3} = 0, \quad \frac{d^2 w}{dx^2} = 0. \quad (16)$$

Substitution of the displacement field into these four conditions yields the 4×4 linear system whose zero determinant provides the resulting frequencies, while the values of C_i define the mode shape of the deformed beam.

Rayleigh theory. Rayleigh theory is identical to the Euler–Bernoulli model with the exception of the addition of the kinetic energy along the beam axis. This term is often referred to as the rotary inertia, and generally results in a lowering of the frequencies compared with the Euler–Bernoulli model. The solution for the transverse displacement is now

$$w(x) = C_1 \sin a_1 x + C_2 \cos a_1 x + C_3 \sinh a_2 x + C_4 \cosh b_2 x, \quad (17)$$

where the dispersion relations identify a and b as

$$a_1 = \sqrt{\rho I \omega^2 / 2 + \sqrt{(\rho I \omega^2 / 2)^2 + \rho A \omega^2}}, \quad (18)$$

$$a_2 = \sqrt{-\rho I \omega^2 / 2 + \sqrt{(\rho I \omega^2 / 2)^2 + \rho A \omega^2}}. \quad (19)$$

The boundary conditions at each free end are given as

$$\frac{d^3 w}{dx^3} + \rho I \omega^2 \frac{dw}{dx} = 0, \quad \frac{d^2 w}{dx^2} = 0. \quad (20)$$

As before, this yields a 4×4 linear system that can be solved for the respective ω and corresponding mode shapes.

Timoshenko theory. In the Timoshenko model, the strain energy and kinetic energy consistent with the full displacement fields are considered where the spatial forms of the transverse displacement $w(x)$ and the section rotation $\Psi(x)$ are given as

$$\begin{Bmatrix} w(x) \\ \Psi(x) \end{Bmatrix} = \begin{Bmatrix} C_1 \\ D_1 \end{Bmatrix} \sin ax + \begin{Bmatrix} C_2 \\ D_2 \end{Bmatrix} \cos ax + \begin{Bmatrix} C_3 \\ D_3 \end{Bmatrix} \sinh ax + \begin{Bmatrix} C_4 \\ D_4 \end{Bmatrix} \cosh ax, \quad (21)$$

where the parameters a and the relations between the C_i and D_i are given in [Han et al. 1999]. The end conditions consistent with the free-free beam are

$$\frac{d^3 \Psi}{dx^3} = 0, \quad \frac{dw}{dx} - \Psi = 0. \quad (22)$$

Substitution of the displacement field into these four conditions yields the 4×4 linear system whose zero determinant provides the resulting frequencies and whose values for C_i and D_i define the mode shape of the deformed beam.

Linear elasticity theory. The problem of traction-free vibration of solids of general shape cannot usually be solved using exact methods. Instead, solutions to Hamilton's principle are sought using Ritz-based approximations for the three displacement components. The displacement fields using this form of approximation were first used in [Demarest 1971], expanded in [Ohno 1976], and refined in perhaps their most efficient form in [Visscher et al. 1991; Migliori and Sarrao 1997]. Their general form can be

expressed as

$$u_1(x_1, x_2, x_3, t) = u(x, y, z, t) = \sum_{j=1}^n c_j(t) \phi_j^u(x, y, z), \quad (23)$$

$$u_2(x_1, x_2, x_3, t) = v(x, y, z, t) = \sum_{j=1}^n d_j(t) \phi_j^v(x, y, z),$$

$$u_3(x_1, x_2, x_3, t) = w(x, y, z, t) = \sum_{j=1}^n e_j(t) \phi_j^w(x, y, z). \quad (24)$$

Here c , d , and e are unknown constants that depend on time, and the functions ϕ are known functions of position. This form of approximation is general, and in fact can be used for a variety of models including those functions that have only local nonzero behavior (such as finite element approximation functions) along with those that exist over the entire domain of the solid. It is the latter class that is of interest in this work. In either case, substitution of these approximations into Hamilton's principle and invocation of the assumption of harmonic motion allows the problem to be reduced into the generalized eigenvalue problem given as

$$\begin{bmatrix} K_{11} & K_{12} & K_{13} \\ K_{21} & K_{22} & K_{23} \\ K_{31} & K_{23} & K_{33} \end{bmatrix} \begin{Bmatrix} c \\ d \\ e \end{Bmatrix} = \omega^2 \begin{bmatrix} M_{11} & 0 & 0 \\ 0 & M_{22} & 0 \\ 0 & 0 & M_{33} \end{bmatrix} \begin{Bmatrix} c \\ d \\ e \end{Bmatrix}. \quad (25)$$

The elements of these matrices are given in the [Appendix](#).

The form of the approximation functions as used in this work is taken as

$$\phi_i = x^j y^k z^l. \quad (26)$$

These functions have the appealing property of being very simple to evaluate over the domain of the parallelepiped while providing a very accurate basis to represent the various displacement components of the beam. It is also possible to use group theory to split the resulting eigenvalue problem into eight smaller problems that separate the vibrational modes according to spatial dependence of the three displacements. This topic has been extensively discussed in [\[Ohno 1976\]](#). The eight groups are defined in [Table 1](#). Similar to the displacement fields of the beam theories, this class of model confines the solution to a

Grp	Disp	x	y	z	Grp	Disp	x	y	z	Grp	Disp	x	y	z	Grp	Disp	x	y	z
OD	u	O	E	E	OX	u	O	O	O	EY	u	O	O	E	EZ	u	O	E	O
	v	E	O	E		v	E	E	O		v	E	E	E		v	E	O	O
	w	E	E	O		w	E	O	E		w	E	O	O		w	E	E	E
EX	u	E	E	E	EV	u	E	O	O	OY	u	E	E	O	OZ	u	E	O	E
	v	O	O	E		v	O	E	O		v	O	O	O		v	O	E	E
	w	O	E	O		w	O	O	E		w	O	E	E		w	O	O	O

Table 1. Groupings of approximation functions. (Grp: group; Disp: displacement.)

specific combination of polynomial forms, but in general the accuracy of this model increases rapidly as the number of terms in the series increases.

The generalized eigenvalue problem for the three-dimensional solid defined earlier gives the general form of solution for the elasticity solution of the free-free beam. Of the eight groups that represent the total beam vibration of an elastic parallelepiped with either isotropic or orthorhombic symmetry, there are four that contain what can be categorized as flexural modes, as the resulting displacement patterns reflect this class of deformation. As one of the beam dimensions grows (for example, the length in the x or axial direction, defined as L in the usual beam theories), the flexural modes become easier to excite and are among the lowest of the frequencies described by the eight symmetry groups. But in all cases used in this study, only those symmetry groupings that are associated with flexure are used to compare with the results from beam theory. Modes having to do with longitudinal shear or torsion about the beam axis, for example, are eliminated from consideration when comparing with results from one-dimensional beam theories.

As the number of terms in the series used to describe the three displacement components is increased, the accuracy in the frequencies improves. To demonstrate this behavior, we consider a beam of length 0.2 m with a square cross-section of 0.01×0.01 m. The elastic constants are taken to be those of steel, with $C_{11} = 269.231$ GPa and $C_{44} = 76.923$ GPa along with a density of 7830 kg/m³. In [Table 2](#), the lowest five flexural frequencies are shown as a function of the parameter $j + k + l$, which is the summed total of all powers in (26). The results indicate an accuracy, at least for these first five modes, that is adequate to at least five figures. Similar results were found for beams with other aspect ratios.

From a full analysis of this rectangular parallelepiped, there are six zero eigenvalues corresponding to the rigid body modes of the solid, then a sequence of seven repeated frequencies that represent what are usually classified as the bending modes of the beam. The first, third, fifth, and seventh frequencies are from the groups (EY, EZ), and the second, fourth, and sixth are from the groups (OY, OZ). These frequencies are repeated since they represent bending about the y and z -axes, and are identical since the beam cross-section is square. It is not until the eighth frequency where a single mode from the group EV makes an appearance. But in general, the focus here is on the bending modes so they can be directly compared with the class of frequency derived from the beam theories.

Frequencies. The mechanics of deformation for beams changes as the slenderness ratio begins to decrease. To demonstrate the limits of beam theory, the lowest five flexural modes are computed for the three main beam theories (Euler–Bernoulli (EB), Rayleigh, and Timoshenko) and compared with the

Mode	Sum of terms in series					
	8	10	12	14	16	18
1	8088.47	8088.47	8088.47	8088.47	8088.47	8088.47
2	21949.9	21943.9	21943.8	21943.8	21943.8	21943.8
3	42147.0	42073.6	42072.7	42072.7	42072.6	42072.6
4	75581.3	68056.1	67652.5	67642.7	67642.5	67642.5
5	115478.	99316.0	97915.6	97855.6	97854.2	97854.1

Table 2. Convergence of frequencies (in radians per second) of isotropic bar with $L = 0.20$ m.

same frequencies as computed using elasticity theory for zero and nonzero Poisson's ratios. This is completed for the isotropic beam using the elastic constants of steel as listed earlier, and for the orthotropic elastic constants of graphite-magnesium given as $C_{11} = C_{22} = 28.18$ (all in GPa), $C_{33} = 174.3$, $C_{12} = 10.67$, $C_{13} = C_{23} = 12.20$, and $C_{66} = 8.76$, with a density of 1738 kg/m^3 [Ledbetter et al. 1989]. The results are given in radians/second and are all computed using a fixed cross-sectional dimension (0.01×0.01) with the length varying to give the specified slenderness ratio. The results are shown in Table 3 for the isotropic beam and Table 4 for the orthotropic beam.

	EB	Rayleigh	Timoshenko	$\nu = 0$	Full
$L = 0.02 \text{ m}$ ($s = 6.928$)	816033.	570862.	515972.	514674.	516233.
	2249460.	1243978.	865076.	858577.	862774.
	4409820.	2024066.	1220600.	1245000.	1227690.
	7289660.	2839420.	1226500.	1266740.	1238280.
	10889500.	3666503.	1623750.	1297740.	1383700.
$L = 0.05 \text{ m}$ ($s = 17.32$)	130565.	120943.	115643.	115547.	115773.
	359914.	308040.	270703.	270111.	271519.
	705571.	553822.	450802.	449397.	452726.
	1166350.	836851.	635424.	633014.	638419.
	1742330.	1143697.	816534.	813070.	819523.
$L = 0.10 \text{ m}$ ($s = 34.64$)	32641.3	31988.3	31534.8	31526.1	31546.3
	89978.5	86145.8	82081.1	82008.3	82180.9
	176393.	164062.	149833.	149599.	150167.
	291586.	262124.	228803.	228303.	229548.
	435581.	376983.	314906.	314056.	316225.
$L = 0.20 \text{ m}$ ($s = 69.28$)	8160.33	8188.69	8087.68	8087.07	8088.47
	22494.6	22243.4	21396.1	21930.1	21943.8
	44098.2	43263.8	42042.2	42019.3	42072.6
	72896.6	70825.6	67562.6	67504.0	67642.5
	108895.	104599.	97688.3	97569.4	97854.1
$L = 0.40 \text{ m}$ ($s = 138.56$)	2040.08	2037.48	2035.50	2035.46	2035.55
	5623.65	5607.75	5587.49	5587.09	5588.01
	11024.5	10971.3	10887.3	10885.7	10889.5
	18224.1	18090.5	17854.5	17849.9	17860.4
	27223.8	26943.0	26413.3	26403.2	26426.6
$L = 1.0 \text{ m}$ ($s = 346.4$)	326.413	326.350	326.299	326.298	326.300
	899.785	899.373	898.847	898.837	898.861
	1763.93	1762.56	1760.35	1760.31	1760.41
	2915.86	2912.42	2906.10	2905.97	2906.26
	4355.81	4348.52	4334.06	4333.77	4334.42

Table 3. Frequencies for isotropic bar with rectangular cross-section.

Several broad observations can be made. The widely used assumption of zero Poisson's ratio as used within an isotropic elasticity model results in frequencies that are nearly always below the exact values with the full elastic constants. This difference is less than one percent for the lowest five modes for slenderness ratios at or above 17 for both the isotropic and orthotropic beams. For slenderness ratios less than about 10, this behavior transitions to less consistent behavior with the differences in frequency rapidly increasing to over 10 percent for some values. However, for most cases, the assumption of no Poisson's effect has a very small influence on the resulting frequency spectra.

	EB	Rayleigh	Timoshenko	$\nu = 0$	Full
$L = 0.02$ m ($s = 6.928$)	1581020.	1106017.	674806.	769102.	769967.
	4358220.	2410141.	801592.	944903.	957027.
	8543800.	3921528.	1155010.	961637.	959906.
	14123400.	5501235.	1416310.	1039640.	1051190.
	21097900.	7103668.	1750170.	1283550.	1281090.
$L = 0.05$ m ($s = 17.32$)	252964.	234321.	189850.	201500.	201793.
	697315.	596813.	359106.	405631.	406741.
	1367010.	1073002.	532576.	617063.	618665.
	2259740.	1621357.	677543.	804311.	805812.
	3375670.	2215856.	857382.	944903.	953822.
$L = 0.1$ m ($s = 34.64$)	63240.9	61975.8	57667.4	58930.7	58963.2
	174329.	166903.	133924.	142312.	142532.
	341752.	317862.	219221.	240694.	241250.
	564934.	507852.	304759.	343250.	344205.
	843917.	730385.	389128.	446464.	447792.
$L = 0.2$ m ($s = 69.28$)	15810.2	15729.6	15417.8	15513.5	15516.0
	43582.2	43095.6	40177.8	41031.6	41053.8
	85438.0	83821.4	73087.0	76023.5	76100.9
	141234.	137221.	110850.	117535.	117713.
	210979.	202655.	151253.	163291.	163610.
$L = 0.4$ m ($s = 138.56$)	3952.56	3947.52	3927.23	3933.52	3933.71
	10895.6	10864.7	10660.9	10723.5	10725.1
	21359.5	21256.4	20431.9	20680.0	20686.4
	35308.4	35049.5	32803.4	33461.6	33478.8
	52744.8	52200.7	47342.1	48721.7	48758.0
$L = 1.0$ m ($s = 346.4$)	632.409	632.287	631.761	631.926	631.930
	1743.29	1742.49	1737.09	1738.78	1738.82
	3417.52	3414.87	3392.30	3399.31	3399.45
	5649.34	5642.66	5578.50	5598.35	5598.86
	8439.17	8425.05	8279.24	8324.08	8325.23

Table 4. Frequencies for anisotropic bar with rectangular cross-section.

The decision to use an Euler–Bernoulli beam theory versus Rayleigh theory is, at least for modern practical applications, rarely an issue. Most analysts will use finite element models in which the rotary inertia is incorporated into the mass matrix of the finite element equations. In general the Rayleigh results are lower than those of Euler–Bernoulli theory since the additional kinetic energy terms from the rotary inertia effectively appear on the same side as the frequency in the eigenvalue equation. For the beams considered in this study, the differences in frequency obtained from these two theories is quite small when the beam is very slender (s over 100), with changes that increase with mode number that also dramatically differ when the beam becomes thick (with s under 50). There is not a significant difference between the isotropic and anisotropic beam behavior in this regard. However, the higher-mode Rayleigh frequencies are larger than the elasticity values by up to several percent even when the beam is very slender (s over 100). For a beam of dimensions $1 \times 1 \times 20$ ($s = 69.28$), the errors in the lowest five frequencies range from 0.7 to 8 percent for the isotropic beam and 1.6 to 25 percent for the orthotropic beam, with the higher modes having the larger errors. When the beam is $1 \times 1 \times 10$ ($s = 34.64$), the errors range from 2.55 to 23 percent for the isotropic case and 6.3 to 69 percent for the orthotropic beam. Hence although the fundamental frequency of the Rayleigh beam yields good agreement with elasticity results, the decision to use either of these two theories to predict higher modes is of questionable merit. This would of course be even more true if these elements are used to consider assemblies of beams into a planar or spatial frame.

The Timoshenko beam model provides excellent agreement with elasticity results for the case of the isotropic beam. For this study, the shear correction coefficient was taken to be 0.85 [Han et al. 1999], which is a well-established value for isotropic and rectangular cross-sections. The fundamental bending mode is well within a single percent of the full elasticity results for virtually all cases, even when the beam becomes very thick. For more realistic slenderness ratios, the first five modes match very well even for relatively stocky beams. For larger slenderness ratios, the frequencies provided by the Timoshenko model are in between the elasticity solutions for zero and nonzero Poisson’s ratio results, and this appears to hold for all of the five lowest bending frequencies. It is only when the slenderness ratio is less than about 10 that the higher modes become less accurate.

For the orthotropic beam, the Timoshenko model appears to be significantly less robust. The shear correction coefficient value was taken to be 0.8406 in the case of these material properties, and was computed according to the method of [Puchegger et al. 2003; 2005]. There have been far fewer studies of shear correction coefficients for orthotropic beams than for the isotropic case, in part because of the wide variability that can exist between the longitudinal and shear moduli for some materials. Once again, the assumption of zero Poisson’s ratio has negligible influence on the results. Most of the frequencies computed using the full stiffness tensor are only slightly (far less than one percent) higher than the frequencies computed using the assumption of zero Poisson’s ratio. The anisotropic Timoshenko theory also does a reasonable job predicting the fundamental bending frequency for moderately stocky beams. However, unlike the isotropic theory, the errors become significant when the slenderness ratio reaches lower double digits (roughly $s = 20$). Additionally, Timoshenko theory does not do as well with higher modes even when the beam is quite thin. Errors between the elasticity and Timoshenko theory for the first five modes are 0.17, 0.60, 1.2, 2.1, and 3.0 percent when the beam dimensions are $1 \times 1 \times 40$, with the Timoshenko model underpredicting the frequencies. When the beam is $1 \times 1 \times 20$, these errors jump to 0.64, 2.2, 4.1, 6.2, and 8.2 percent. For a $1 \times 1 \times 10$ beam, they are 2.2, 6.4, 10.0, 12.9, and

15.1 percent. These differences are far more significant than for the isotropic case, suggesting that a single shear coefficient has difficulty capturing the total energy contribution from higher modes when the material is anisotropic.

Mode shapes. The mode shapes for the beam theories and the elasticity theory are easily computed using the solution of the respective eigenvalue problems. The distorted shapes of the lowest five modes are shown in [Figure 1](#) for slenderness ratios of 69.28 (a $1 \times 1 \times 20$ beam) and 6.928 (a $1 \times 1 \times 2$ beam) for

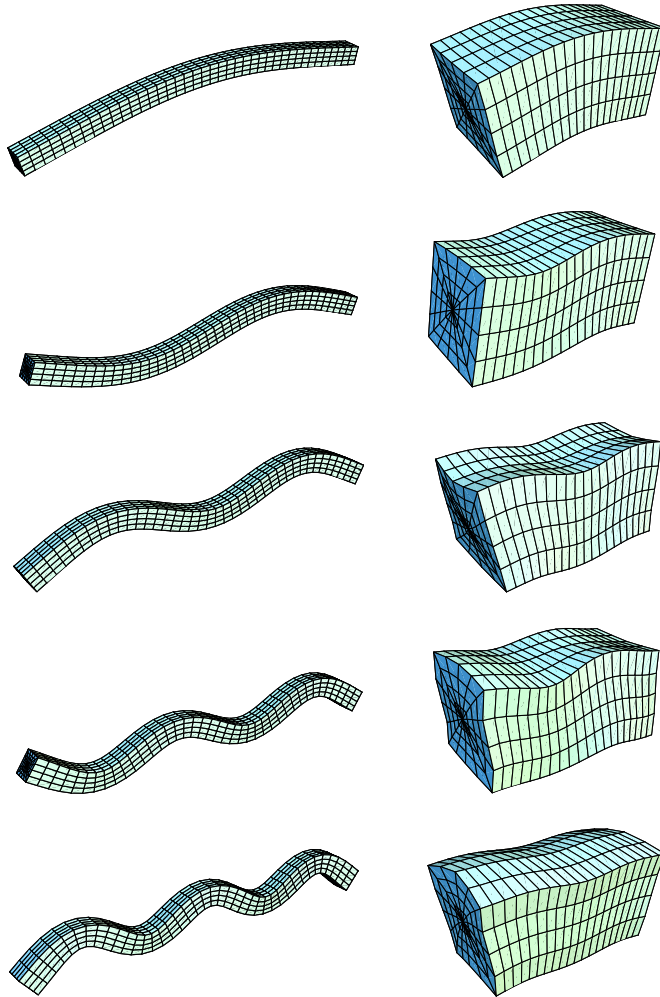


Figure 1. The first five mode shapes for the isotropic beam change in character as the slenderness ratio decreases, shown here as computed by elasticity theory. On the left, the modes for relative dimensions of $1 \times 1 \times 20$ ($s = 69.28$) are well represented by the beam theories, and plots of the transverse displacement are virtually identical to those for all three beam theories and elasticity theory. On the right, with a geometry of $1 \times 1 \times 2$ ($s = 6.928$), significant changes are apparent, with curved lines through the thickness and surfaces that possess significant warping.

isotropic material properties. Usually these modes are plotted using only the transverse displacement w for the beam theories (along with the section rotation for Timoshenko theory) but in this case we have plotted the entire solid. For the slender beam, there is no visible difference between the transverse displacement pattern between the elasticity and beam theory results, and the deformation field is significant in that the entire surfaces of the beam remain relatively smooth. In fact, one can see that the plane sections of the beam are remaining flat and are deforming very close to the assumptions of the Euler–Bernoulli and Rayleigh theories.

For the thicker beam, there are significant changes in behavior for these modes. The lowest mode shape is very similar to that of the thin beam, but as the modes progress in order there is an increasingly large deviation from the smooth-faced behavior of the slender beam. There is not only distortion of the vertical lines representing the plane deformation, but there are indications of warping across the top surfaces along with a total deformation field that is difficult to capture using only one or two variables. The case of $s = 6.928$ is somewhat extreme, but the transition from slender beam behavior to vibrating solid behavior is the crucial aspect of this work.

These plots give an indication of the visual difference between behaviors, but other metrics can be used to reinforce the sources of the changes in frequency. Because so much of the deformation is comprised of the axial stretch along the length of the beam, it is useful to consider the changes in the deformation pattern as the modes increase and the slenderness ratio decreases. Figure 2 shows the contours of the axial displacement for the upper right quadrant of the beam for the lowest five modes of the isotropic beam with stocky geometry ($1 \times 1 \times 5$ and $1 \times 1 \times 2$). The contours associated with all three beam theories are not shown but they are easy to visualize: they would be perfectly straight horizontal lines spaced an equal distance in the vertical direction (see the form of the axial displacement component u for the beam theories, which all linearly depend on z but have no spatial dependence on the other cross-sectional component).

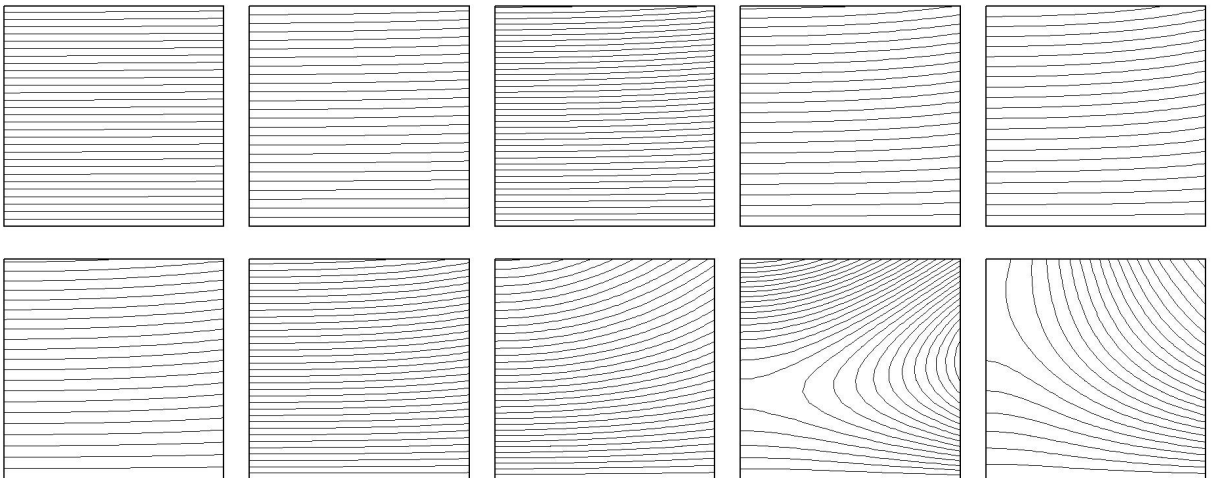


Figure 2. These contour plots show the upper right quadrant of the axial displacement for the isotropic beam computed using elasticity theory for lengths of 0.05 (top) and 0.02 (bottom). The lowest modes are on the left. They demonstrate the breakdown of beam theory approximations which assume that these components are linear in z .

These figures clearly show how the assumption of single-power displacement fields can be adequate for low-mode, high- s vibrations. In fact, even the fundamental mode for $s = 17.32$ is well captured by such an assumption. But as the mode number increases, the displacement field becomes nonlinear in the horizontal coordinate direction of the beam cross-section, and the displacement fields for the low- s beams diverge even more strongly. They indicate that a slightly more inclusive displacement field, perhaps with a small number of additional terms dependent on the $x_2 = y$ coordinate, could better capture this basic behavior.

Kinetic and strain energy. The goal of most beam theories is to be able to mimic the actual behavior of a solid using as few variables as possible. Since the natural frequencies of a vibrating solid are dependent on the ability of these theories to capture both the kinetic and strain energies corresponding to each mode shape, the sources of error when compared with elasticity solutions can be determined and potentially eliminated using more sophisticated kinematic assumptions.

The strain energy density U_o at any point in the solid can be expressed as

$$U_o = U_o^{11} + U_o^{22} + U_o^{33} + U_o^{23} + U_o^{13} + U_o^{12} = \frac{1}{2}\sigma_{11}\epsilon_{11} + \frac{1}{2}\sigma_{22}\epsilon_{22} + \frac{1}{2}\sigma_{33}\epsilon_{33} + \sigma_{23}\epsilon_{23} + \sigma_{13}\epsilon_{13} + \sigma_{12}\epsilon_{12}, \quad (27)$$

and the kinetic energy density can be expressed as

$$K = K_o^{11} + K_o^{22} + K_o^{33} = \frac{1}{2}\rho\dot{u}_1^2 + \frac{1}{2}\rho\dot{u}_2^2 + \frac{1}{2}\rho\dot{u}_3^2. \quad (28)$$

These scalar functions of position can be integrated over the domain of the beam to give the strain energy and kinetic energy associated with any displaced shape of the beam. For example, we can define

$$K^{11} = \int_V K_o^{11} dV. \quad (29)$$

Hence K^{11} is simply the size of the kinetic energy term along the axis of the beam for a specific modal deformation pattern. Using this separation and the modal displacement patterns that result from the solution of the eigenvalue problem, it is a simple matter to separate the relative contribution of each displacement component and stress-strain contribution to the total kinetic and strain energies for each mode. This allows an assessment of the sources of error between elasticity theory and the beam theories.

The influence of each term is shown by computing the relative size of the contribution of each of the terms from the kinetic and strain energy terms for the first five modes considered in the earlier examples. Since the amplitude of each mode is arbitrary, the values are normalized with respect to the dominant terms in the kinetic (K^{33}) and strain (U_{11}) energies. These terms are selected as the reference values since for flexural modes most of the energy associated with the motion is transverse for the kinetic term and axial for the strain term. Hence for each mode the amplitudes of motion are scaled so that the other terms are relative to the dominant values.

Results are shown in [Figure 3](#) for the case of strain energy and [Figure 4](#) for the case of kinetic energy. In [Figure 3](#), the results are given in terms of the transverse shear strain energy scaled by the axial strain energy as a function of beam length for the isotropic and orthotropic cases. In [Figure 4](#), the results are given in terms of the axial kinetic energy scaled by the transverse kinetic energy as a function of beam length. The contributions of all other terms are consistently several orders of magnitude lower than those of these two dominant terms and it would make little sense to modify existing beam theories to better capture these terms. They were not plotted here. The transverse kinetic energy (K^{33}) and axial strain

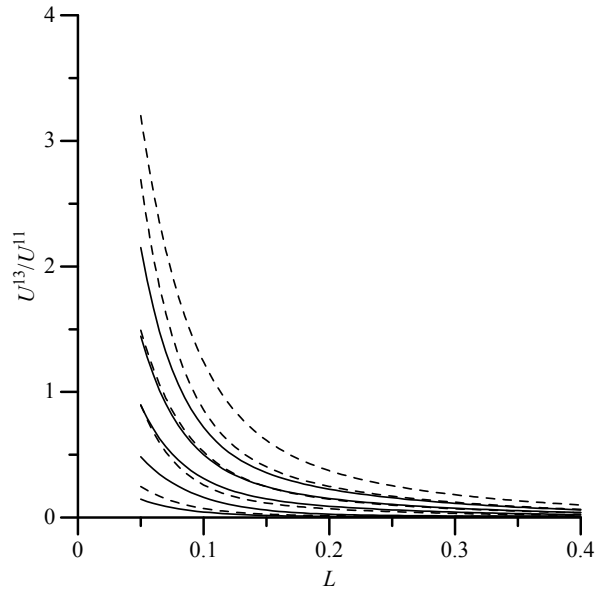


Figure 3. The ratio of the transverse shear energy to the axial energy is shown for the 0.01×0.01 beam as a function of beam length for the first five modes of the isotropic (solid lines) and orthotropic (dashed) beams. This ratio increases with mode number and is significantly more pronounced for the orthotropic beam.

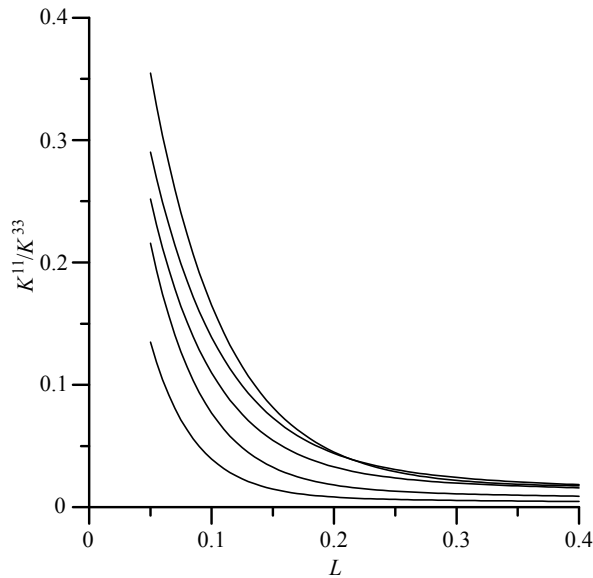


Figure 4. The ratio of the axial kinetic energy to the transverse kinetic energy is shown for the 0.01×0.01 beam as a function of beam length for the first five modes of the isotropic beam. This ratio generally increases with mode number but for most reasonably sized beams is less than five percent of the total contribution.

energy (U^{11}) dominate the total kinetic and strain energies for all thin beams. The shear strain energy contribution is larger than the rotary kinetic contribution by a factor of roughly 2–5 for the isotropic case and roughly 5–10 times higher for the orthotropic beam.

In addition to the tabulated results, the ratios of the energies as computed using elasticity theories to those of Timoshenko theory were also computed. The ratios of the transverse kinetic energy of the isotropic beam computed by elasticity theory to that of Timoshenko theory when the maximum displacements are the same are given by 0.9996, 0.9996, 0.9997, 1.00001, and 1.0013 for beams of length 1, 0.4, 0.2, 0.1, and 0.05, respectively. For the orthotropic beam, these ratios are 0.99914, 1.0013, 1.0061, 1.0234, and 1.079. The ratios of the axial strain energies for the lowest modes of the isotropic beam (again with $L = 1.0, 0.4, 0.2, 0.1,$ and 0.05) are 1.000004, 1.000024, 1.000099, 1.0004, and 1.0018, respectively. The axial kinetic energy ratios (elasticity over Timoshenko) are 0.99983, 0.99986, 0.999993, 1.0005, and 1.0025. However, for the orthotropic beam the axial strain energy ratios are 1.00079, 1.0049, 1.0194, 1.0737, and 1.256. For the axial kinetic energy, the ratios are 1.00115, 1.0081, 1.0322, 1.122, and 1.417.

Static response. The static response of a simply supported beam of length L under sinusoidal transverse loading $q(x) = q_o \sin(\pi x/L)$ is an extremely well-known problem that can also be used to compare beam theories with elasticity solutions. A beam under plane stress has the elastic constants E_1, E_3, G_{13} , and ν_{13} and has a base width of b and a height of h , with the area and second moment of area being given by $A = bh$ and $I = bh^3/12$.

Euler–Bernoulli theory. The governing equation (8) can be readily solved under the boundary conditions of $w = 0$ and $d^2w/dx^2 = 0$ at $x = 0$ and $x = L$ to give

$$w(x) = \frac{q_o L^4}{\pi^4 EI} \sin \frac{\pi x}{L}. \quad (30)$$

Here $E = E_1$, which is simply the elastic modulus along the beam axis. The other elastic constants play no role in the one-dimensional response for this theory.

Timoshenko theory. An exact Timoshenko solution can be obtained by substituting the assumed solution

$$w(x) = C_1 \sin \frac{\pi x}{L}, \quad \Psi(x) = C_2 \cos \frac{\pi x}{L}, \quad (31)$$

into the governing equations (12) and (13). This results in the solution of the linear system

$$\begin{bmatrix} kGA \frac{\pi^2}{L^2} & kGA \frac{\pi}{L} \\ kGA \frac{\pi}{L} & kGA + EI \frac{\pi^2}{L^2} \end{bmatrix} \begin{Bmatrix} C_1 \\ C_2 \end{Bmatrix} = \begin{Bmatrix} q_o \\ 0 \end{Bmatrix}. \quad (32)$$

Here $G = G_{13}$, where now the beam response is a function of the two elastic constants E and G . This is true for both the isotropic and anisotropic cases.

Plane elasticity solution. A solution that is exact within the constraints of plane stress can also be obtained for this problem. This is in fact a special case of the exact solution obtained in [Pagano 1969]. The equilibrium equations in the x and z directions for a beam/strip along the x -axis of length L and

height in z of h can be expressed as

$$C_{11} \frac{\partial^2 u}{\partial x^2} + C_{13} \frac{\partial^2 w}{\partial x \partial z} + C_{55} \frac{\partial^2 u}{\partial z^2} + C_{55} \frac{\partial^2 w}{\partial x \partial z} = 0, \quad (33)$$

$$C_{55} \frac{\partial^2 w}{\partial x^2} + C_{55} \frac{\partial^2 w}{\partial x \partial z} + C_{33} \frac{\partial^2 u}{\partial z^2} + C_{13} \frac{\partial^2 w}{\partial x \partial z} = 0. \quad (34)$$

Here the elastic constants are obtained by inverting the compliance matrix under plane stress conditions (which contains E_1 , E_3 , G_{13} , and ν_{13}) to obtain the reduced stiffnesses C_{11} , C_{33} , C_{13} , and C_{55} .

The displacement field can be assumed as

$$u(x, z) = A \cos \frac{\pi x}{L} \exp \lambda z, \quad w(x, z) = B \sin \frac{\pi x}{L} \exp \lambda z. \quad (35)$$

Substituting these into equilibrium yields the matrix expression

$$\begin{bmatrix} C_{55} \lambda^2 - C_{11} \left(\frac{\pi}{L}\right)^2 & \lambda \frac{\pi}{L} (C_{13} + C_{55}) \\ -\lambda \frac{\pi}{L} (C_{13} + C_{55}) & C_{33} \lambda^2 - C_{55} \left(\frac{\pi}{L}\right)^2 \end{bmatrix} \begin{Bmatrix} A \\ B \end{Bmatrix} = \begin{Bmatrix} 0 \\ 0 \end{Bmatrix}. \quad (36)$$

The values for λ can be obtained by taking the determinant of the 2×2 matrix for given elastic constants and beam length and setting the result to zero.

For isotropic beams, the four C_{ij} are reduced to two independent constants, and there are two repeated roots for λ . The solutions are given by

$$u(x, z) = \cos \frac{\pi x}{L} [(A_1 + A_2 z) \exp \pi z/L + (A_3 + A_4 z) \exp -\pi z/L], \quad (37)$$

$$w(x, z) = \sin \frac{\pi x}{L} [(B_1 + B_2 z) \exp \pi z/L + (B_3 + B_4 z) \exp -\pi z/L]. \quad (38)$$

Here the constants B_i are related to the constants A_i via

$$B_1 = A_1 - \frac{3C_{11} - C_{13}}{C_{11} + C_{13}} \frac{L}{\pi} A_2, \quad B_2 = A_2, \quad (39)$$

$$B_3 = -A_3 - \frac{3C_{11} - C_{13}}{C_{11} + C_{13}} \frac{L}{\pi} A_4, \quad B_4 = -A_4. \quad (40)$$

For the orthotropic beam, the four roots for λ_i are generally distinct and depend on the specific set of elastic constants. The displacements can be expressed as

$$u(x, z) = \cos \frac{\pi x}{L} [A_1 \exp \lambda_1 z + A_2 \exp \lambda_2 z + A_3 \exp \lambda_3 z + A_4 \exp \lambda_4 z], \quad (41)$$

$$w(x, z) = \sin \frac{\pi x}{L} [B_1 \exp \lambda_1 z + B_2 \exp \lambda_2 z + B_3 \exp \lambda_3 z + B_4 \exp \lambda_4 z], \quad (42)$$

where now the constants are related via

$$B_i = \frac{C_{11} (\pi/L)^2 - C_{55} \lambda_i^2}{\lambda_i (\pi/L) (C_{13} + C_{55})} A_i. \quad (43)$$

In either case, the four constants are evaluated using the four boundary conditions on the tractions at the lower and upper surfaces of the beam. The bottom surface is traction free, and the condition at the upper surface is $\sigma_{zz} = q(x)$. The stresses can be readily computed using the appropriate constitutive law.

Displacements. In the discussion that follows, both isotropic and orthotropic constitutive laws are used. In the case of isotropic beams, the Poisson's ratio is assumed to be equal to 0.3 and the resulting displacements and stresses are compared relative to the results determined by Euler–Bernoulli theory that depend only on the elastic modulus. For the orthotropic case, the material properties used are taken as $E_1 = 155$, $E_3 = 12.1$, $G_{13} = 4.40$ (all in GPa), and $\nu_{13} = 0.248$. These values are typical of a graphite-polymer composite [Hyer 1998].

The maximum displacement at the center of the beam can be used as a single point of comparison to determine relative levels of error in beam theory assumptions. This is shown in Figure 5 for the isotropic and orthotropic beams. Only the Timoshenko and elasticity solutions are plotted since the dimensionless displacement from the Euler–Bernoulli model does not depend on length. The results are shown over the key region from $L/h = 4$ to $L/h = 12$, which corresponds to a range of slenderness ratio of roughly 14–40.

As was the case for free vibration, there is again excellent agreement between the elasticity and Timoshenko models for this fundamental behavior. The isotropic Timoshenko beam has displacements that are slightly above those of the elasticity results, while the orthotropic Timoshenko beam varies from being slightly below elasticity for larger lengths to slightly above for shorter beams. The more dramatic leap is the distinction between Euler–Bernoulli theory for isotropic versus orthotropic beams. For slenderness ratios in the low double-digits, Euler–Bernoulli theory underpredicts the displacement by a factor of between 1.5 and 3. For the isotropic beam, there is not nearly this level of discrepancy, with a maximum difference of less than 20 percent.

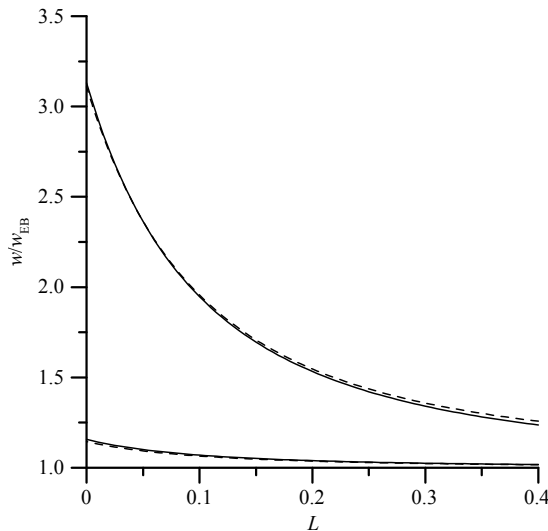


Figure 5. The ratio of the maximum transverse displacement at the beam center as computed by Timoshenko (solid) and elasticity (dashed) theories over the Euler–Bernoulli prediction is shown for the isotropic (lower curves) and orthotropic (upper curves) beams under static loading for a 1×1 beam as a function of beam length.

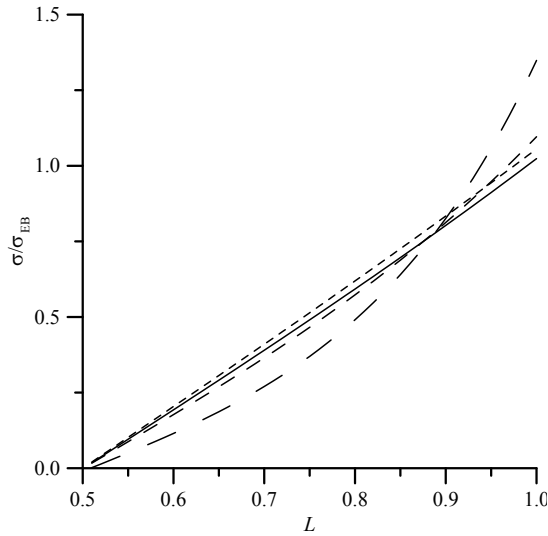


Figure 6. The ratio of the through-thickness distribution of axial stress σ_{xx} is shown over the upper half of the isotropic beam using the elasticity solution for $L = 4$ (solid) and the orthotropic beam for $L = 4$ (long dash), $L = 8$ (medium dash), and $L = 20$ (long dash). The response of the Timoshenko beam is essentially identical to the isotropic case even when the beam is short.

The longitudinal modulus is larger than the shear modulus by a factor of 2.6 for the isotropic beam but by a factor of over 35 for the orthotropic beam. As the beam becomes shorter and shear deformations accumulate, a softer shear modulus will yield much larger levels of shear deformation that cannot be captured by purely axial stiffness.

Stress. The distribution of the bending stress σ_{xx} for several cases is shown in Figure 6 for the upper half of the beam (here a beam of unit depth $h = 1$ was used). Both Euler–Bernoulli and Timoshenko theories give a distribution that is linear in z , and the question becomes how much the exact elasticity solution varies from this behavior. This figure shows that the assumption of linear variation is quite sound except for in the case of thick beams (s less than about 30), where the distribution begins to go nonlinear. For lengths of 20, 8, and 4 the elementary theory underpredicts this stress by 6, 10, and 35 percent in the orthotropic case. The isotropic beam has much smaller error, with a length of 4 giving only 2 percent error at the extreme locations of the beam cross-section. The Timoshenko beam does a very good job of capturing the maximum values of transverse shear stress regardless of aspect ratio or material constitution.

Conclusions

For the small number of cases considered here, we conclude the following:

- (1) For both the isotropic and orthotropic beams, the assumption of zero Poisson’s ratio has an extremely small influence. This is true for all modes and nearly all slenderness ratios explored using elasticity theory.

- (2) When s is less than 100, Euler–Bernoulli theory is not competitive. For orthotropic beams, significant errors (over a single percent) appear, especially for higher modes, even when this ratio is over 100.
- (3) The inclusion of the rotary inertia terms in the kinetic energy within Rayleigh theory offers only marginal improvement over the Euler–Bernoulli model. These differences are consistent with errors that are small (several percent at $s = 100$ for the isotropic case) but rapidly increase to over ten percent when s drops to low double digits and the mode number increases. For the orthotropic case, the errors are significant even at $s = 50$.
- (4) For an isotropic beam with a relatively small ratio (under 3 in this case) between the axial modulus and the shear modulus, Timoshenko theory is extremely robust even as the slenderness ratio approaches single digits. For $s = 7$ (which represents a beam that is $1 \times 1 \times 2$), the lowest four frequencies are within a single percent error.
- (5) For the orthotropic beam with a relatively large ratio (approximately 13 in this case) between the axial modulus and the shear modulus, Timoshenko theory generates significant errors even for beams that are relatively slender ($s = 50$), with even the fundamental frequency having an error well over a percent and even larger errors (up to 8 percent) for the higher modes. For stocky beams ($s = 10$ or so), errors are well into double digits for most of the frequencies.
- (6) Rayleigh theory overpredicts the contribution of axial kinetic energy, but the lack of shear deformation restricts the relative motion and the resulting frequencies are above those of elasticity theory even for relatively high values (mid double-digit) of s .
- (7) The isotropic Timoshenko beam is extremely accurate in capturing the relative axial kinetic energy contribution but underpredicts the contribution to transverse shear strain energy, leading to frequencies that are slightly below those of elasticity theory. For orthotropic Timoshenko beams, the axial kinetic energy is underpredicted and the strain energy contributions are overpredicted, with frequencies below those of elasticity theory.
- (8) Under static response, isotropic beams modeled using Euler–Bernoulli theory underpredict maximum displacements by up to 20 percent for relatively thick beams but by a factor of about 3 for the orthotropic case.
- (9) Static axial stress fields for isotropic beams are captured well by both Euler–Bernoulli and Timoshenko theories, even when the beam is relatively thick. Orthotropic beams generate an axial stress that goes nonlinear over the cross-section at a much higher aspect ratio, with errors of over 25 percent for $L/h = 4$.

Returning to the title, when, in fact, do beam theories fail? For isotropic materials, one potential answer is this: earlier (that is, at larger values of s) than one might expect for Euler–Bernoulli and Raleigh theories, and later (that is, at smaller values of s) than one might expect for Timoshenko theory. Given that many studies use these beam theories to predict the resonant modes for assemblies of beam/frame elements for beam geometries that possess moderately low values of s , these errors could accumulate to cast doubt on the overall accuracy of such approaches.

For orthotropic beams with high ratios of elastic to shear moduli, the answer is even more dire: one-dimensional theories generate significant errors in vibrational response even at high values (over 100)

of s . This is true even to the point that there appears to be room for adjustments or wholesale revisions of these basic theories when the material is anisotropic. Given the discrepancy between the axial kinetic and strain energy values between elasticity and Timoshenko theories, it would not be unreasonable to modify the axial displacement component as a next step in applying beam theory to the class of orthotropic beams. But one result is clear: caution should be applied in interpreting results obtained by applying beam theories to problems where higher modes, energy, or stresses are of significant interest.

Appendix

Elasticity theory. The elements of the coefficient matrices are a function of the elastic constants C_{ij} and the Ritz approximation functions ϕ , for which the superscripts indicate the variable to which that function is linked. These entries are given as

$$\begin{aligned}
 K_{ij}^{11} &= \int_V \left(C_{11} \frac{\partial \phi_i^u}{\partial x} \frac{\partial \phi_j^u}{\partial x} + C_{55} \frac{\partial \phi_i^u}{\partial z} \frac{\partial \phi_j^u}{\partial z} + C_{66} \frac{\partial \phi_i^u}{\partial y} \frac{\partial \phi_j^u}{\partial y} \right) dV, \\
 K_{ij}^{12} &= \int_V \left(C_{12} \frac{\partial \phi_i^u}{\partial x} \frac{\partial \phi_j^v}{\partial y} + C_{66} \frac{\partial \phi_i^u}{\partial y} \frac{\partial \phi_j^v}{\partial x} \right) dV = K_{ji}^{21}, \\
 K_{ij}^{13} &= \int_V \left(C_{13} \frac{\partial \phi_i^u}{\partial x} \frac{\partial \phi_j^w}{\partial z} + C_{55} \frac{\partial \phi_i^u}{\partial z} \frac{\partial \phi_j^w}{\partial x} \right) dV = K_{ji}^{31}, \\
 K_{ij}^{22} &= \int_V \left(C_{22} \frac{\partial \phi_i^v}{\partial y} \frac{\partial \phi_j^v}{\partial y} + C_{44} \frac{\partial \phi_i^v}{\partial z} \frac{\partial \phi_j^v}{\partial z} + C_{66} \frac{\partial \phi_i^v}{\partial x} \frac{\partial \phi_j^v}{\partial x} \right) dV, \\
 K_{ij}^{23} &= \int_V \left(C_{23} \frac{\partial \phi_i^v}{\partial y} \frac{\partial \phi_j^w}{\partial z} + C_{44} \frac{\partial \phi_i^v}{\partial z} \frac{\partial \phi_j^w}{\partial y} \right) dV = K_{ji}^{32}, \\
 K_{ij}^{33} &= \int_V \left(C_{33} \frac{\partial \phi_i^w}{\partial z} \frac{\partial \phi_j^w}{\partial z} + C_{44} \frac{\partial \phi_i^w}{\partial y} \frac{\partial \phi_j^w}{\partial y} + C_{55} \frac{\partial \phi_i^w}{\partial x} \frac{\partial \phi_j^w}{\partial x} \right) dV, \\
 M_{ij}^{11} &= M_{ij}^{22} = M_{ij}^{33} = \int_V \psi_i \psi_j dV.
 \end{aligned}$$

References

- [Abbas and Thomas 1977] B. A. H. Abbas and J. Thomas, “The second frequency spectrum of Timoshenko beams”, *J. Sound Vib.* **51** (1977), 123–137.
- [Anderson 1953] R. A. Anderson, “Flexural vibration of uniform beams according to the Timoshenko theory”, *J. Appl. Mech. (ASME)* **75** (1953), 504–510.
- [Cooper 1966] G. R. Cooper, “The shear coefficient in Timoshenko’s beam theory”, *J. Appl. Mech. (ASME)* **33** (1966), 335–340.
- [Demarest 1971] H. H. Demarest, Jr., “Cube resonance method to determine the elastic constants of solids”, *J. Acoust. Soc. Am.* **49** (1971), 768–775.
- [Dolph 1954] C. L. Dolph, “On the Timoshenko theory of transverse beam vibrations”, *Quart. Appl. Math.* **12** (1954), 175–187.
- [Gruttmann and Wagner 2001] F. Gruttmann and W. Wagner, “Shear correction factors in Timoshenko’s beam theory for arbitrary shaped cross-sections”, *Comput. Mech.* **27** (2001), 199–207.
- [Han et al. 1999] S. M. Han, H. Benaroya, and T. Wei, “Dynamics of transversely vibrating beams using four engineering beam theories”, *J. Sound Vib.* **225** (1999), 935–988.

- [Herrmann 1955] G. Herrmann, “Forced motions of Timoshenko beam theory”, *J. Appl. Mech. (ASME)* **77** (1955), 53–56.
- [Hodges 2006] D. H. Hodges, *Nonlinear composite beam theory for engineers*, American Institute of Aeronautics and Astronautics, Reston, VA, 2006.
- [Huang 1961] T. C. Huang, “The effect of rotatory inertia and of shear deformation on the frequency and normal mode equations of uniform beams with simple end conditions”, *J. Appl. Mech. (ASME)* **28** (1961), 579–584.
- [Hutchinson 2001] J. R. Hutchinson, “Shear coefficients for Timoshenko beam theory”, *J. Appl. Mech. (ASME)* **68** (2001), 87–92.
- [Hyer 1998] M. W. Hyer, *Stress analysis of fiber-reinforced composite materials*, McGraw-Hill, Boston, 1998.
- [King 1985] J. L. King, “The free transverse vibrations of anisotropic beams”, *J. Sound Vib.* **98** (1985), 575–585.
- [Ledbetter et al. 1989] H. M. Ledbetter, S. K. Datta, and T. Kyono, “Elastic constants of a graphite-magnesium composite”, *J. Appl. Phys.* **65** (1989), 3411–3416.
- [Levinson 1981] M. Levinson, “A new rectangular beam theory”, *J. Sound Vib.* **74** (1981), 81–87.
- [Love 1927] A. E. H. Love, *A treatise on the mathematical theory of elasticity*, 4th ed., Dover, New York, 1927.
- [Marigo and Meunier 2006] J.-J. Marigo and N. Meunier, “Hierarchy of one-dimensional models in nonlinear elasticity”, *J. Elasticity* **83**:1 (2006), 1–28.
- [Migliori and Sarrao 1997] A. Migliori and J. L. Sarrao, *Resonant ultrasound spectroscopy: applications to physics, materials measurements and non-destructive evaluation*, Wiley, New York, 1997.
- [Ohno 1976] I. Ohno, “Free vibration of a rectangular parallelepiped crystal and its application to determination of elastic constants of orthorhombic crystals”, *J. Phys. Earth* **24** (1976), 355–379.
- [Pagano 1969] N. Pagano, “Exact solutions for composite laminates in cylindrical bending”, *J. Compos. Mater.* **3** (1969), 398–411.
- [Puchegger et al. 2003] S. Puchegger, D. Loidl, K. Kromp, and H. Peterlik, “Hutchinson’s shear coefficient for anisotropic beams”, *J. Sound Vib.* **266** (2003), 207–216.
- [Puchegger et al. 2005] S. Puchegger, D. Loidl, K. Kromp, H. Peterlik, and R. Weiss, “Extension of the resonant beam technique to highly anisotropic materials”, *J. Sound Vib.* **279** (2005), 1121–1129.
- [Schramm et al. 1994] U. Schramm, L. Kitis, W. Kang, and W. D. Pilkey, “On the shear deformation coefficient in beam theory”, *Finite Elem. Anal. Des.* **16** (1994), 141–162.
- [Stephen 1978] N. G. Stephen, “On the variation of Timoshenko’s shear coefficient with frequency”, *J. Appl. Mech. (ASME)* **45** (1978), 695–697.
- [Stephen 2001] N. G. Stephen, “Discussion of Hutchinson’s paper shear coefficients for Timoshenko beam theory”, *J. Appl. Mech. (ASME)* **68** (2001), 959–960.
- [Thomas and Abbas 1975] J. Thomas and B. A. H. Abbas, “Finite element model for dynamic analysis of Timoshenko beam”, *J. Sound Vib.* **41** (1975), 291–299.
- [Timoshenko 1921] S. P. Timoshenko, “On the correction for shear of the differential equation for transverse vibrations of bars of uniform cross-section”, *Philos. Mag.* **41** (1921), 744–746.
- [Timoshenko 1922] S. P. Timoshenko, “On the transverse vibrations of bars of uniform cross-section”, *Philos. Mag.* **43** (1922), 125–131.
- [Timoshenko 1953] S. P. Timoshenko, *History of strength of materials*, Dover, New York, 1953.
- [Traill-Nash and Collar 1953] R. W. Traill-Nash and A. R. Collar, “The effects of shear flexibility and rotatory inertia on the bending vibrations of beams”, *Quart. J. Mech. Appl. Math.* **6** (1953), 186–222.
- [Visscher et al. 1991] W. M. Visscher, A. Migliori, T. M. Bell, and R. A. Reinert, “On the normal modes of free vibration of inhomogeneous and anisotropic elastic objects”, *J. Acoust. Soc. Am.* **90** (1991), 2154–2162.

Received 2 Jul 2012. Revised 15 Nov 2012. Accepted 13 Jan 2013.

PAUL R. HEYLIGER: prh@engr.colostate.edu

Department of Civil and Environmental Engineering, Colorado State University, Fort Collins, CO 80523-1372, United States

TRANSIENT 3D SINGULAR SOLUTIONS FOR USE IN PROBLEMS OF PRESTRESSED HIGHLY ELASTIC SOLIDS

LOUIS MILTON BROCK

The dynamic perturbation of a neo-Hookean solid in an initial equilibrium state of finite deformation can be viewed as the superposition of infinitesimal strains upon large ones. Three transient 3D singular problems whose solutions are useful in generating the former are studied. The first and second concern, respectively, a concentrated force and a point displacement discontinuity in an unbounded solid; the third problem involves a concentrated force applied at a point on the surface of a half-space. The governing equations resemble those for a linear anisotropic solid. Analytic solutions are obtained, as well as formulas and calculations for anisotropic wave speeds. Formulation of the problems is in terms of Cartesian coordinates, but expressions for the solutions and wave speeds make use of a quasipolar coordinate system.

1. Introduction

Loading of a prestressed highly elastic solid may produce incremental deformations that are infinitesimal in nature. Equations for infinitesimal deformation superimposed upon large can be developed [Green and Zerna 1968; Beatty and Usmani 1975] to describe this perturbation response. These equations are generally similar in form to those for anisotropic, linear elastic solids [Ting 1996], with elastic constants that depend on constitutive equations for the highly elastic solid and the prestress. As in isotropic elasticity, whether classical [Love 1944] or transient [Achenbach 1973], quasistatic [Willis 1965; Ting 1996] and transient [Wang and Achenbach 1992] singular solutions can serve as the basis for treating general dynamic loading. Moreover, the singular solutions themselves give insight into anisotropic behavior.

To illustrate the construction of such solutions this article considers a simple, neo-Hookean isotropic solid. The principal stress and principal material axes coincide, and the former is uniform. The anisotropic 3D equations of small deformation in an unbounded solid are solved for the cases of a concentrated force and a displacement discontinuity at a point. The 3D equations for the half-space subject to a concentrated surface force are then considered. Analytic solutions and formulas for body-wave and Rayleigh-wave speeds are provided. Sample calculations for the latter are also presented. The solution process involves integral transforms in Cartesian coordinates, coupled with inversions based on quasipolar and quasispherical coordinates [Brock 2012; 2013] and a standard method of de Hoop [1960]. The solution expressions are, therefore, in a hybrid but uncomplicated form.

Keywords: neo-Hookean, dynamic perturbation, 3D singular solution, transient.

2. Field equations

An elastic body \mathfrak{R} is homogeneous and isotropic relative to an undisturbed reference configuration \mathfrak{R}_0 . Smooth motion $\mathbf{x} = \mathbf{x}(\mathbf{X})$ takes \mathfrak{R} to deformed equilibrium configuration \mathfrak{R} . Cauchy stress \mathbf{T} in \mathfrak{R} is [Green and Zerna 1968; Beatty and Usmani 1975]

$$\mathbf{T} = \alpha_0 \mathbf{1} + \alpha_1 \mathbf{B} + \alpha_2 \mathbf{B}^2, \quad \mathbf{B} = \mathbf{F} \mathbf{F}^T, \quad \mathbf{F} = \frac{\partial \mathbf{x}}{\partial \mathbf{X}}. \quad (1)$$

Here $\mathbf{1}$ is the identity tensor, $(\alpha_0, \alpha_1, \alpha_2)$ are scalar functions of the principal invariant (I, II, J) of \mathbf{B} , and body forces are neglected. Inequalities based on the experiment [Truesdell and Noll 1965] support restrictions

$$\alpha_0 - II\alpha_2 \leq 0, \quad \alpha_1 + I\alpha_2 > 0, \quad \alpha_2 \leq 0. \quad (2)$$

An adjacent nonequilibrium deformed configuration \mathfrak{R}^* arises upon superposition of an infinitesimal displacement \mathbf{u} that depends on \mathbf{X} and time. This requires perturbation Cauchy stress $\mathbf{T}' = \mathbf{T}^* - \mathbf{T}$, where \mathbf{T}^* is the Cauchy stress in \mathfrak{R}^* . To the first order in $\nabla \mathbf{u}$ its components in the principal reference system, that is, $\mathbf{B} = \text{diag}\{\lambda_1^2, \lambda_2^2, \lambda_3^2\}$ where $(\lambda_1, \lambda_2, \lambda_3)$ is the principal stretch, are

$$\begin{bmatrix} T'_{11} \\ T'_{22} \\ T'_{33} \end{bmatrix} = \begin{bmatrix} \lambda'_{11} + 2\mu'_{11} & \lambda'_{12} & \lambda'_{13} \\ \lambda'_{21} & \lambda'_{22} + 2\mu'_{22} & \lambda'_{23} \\ \lambda'_{31} & \lambda'_{32} & \lambda'_{33} + 2\mu'_{33} \end{bmatrix} \begin{bmatrix} \partial_1 u_1 \\ \partial_2 u_2 \\ \partial_3 u_3 \end{bmatrix}, \quad (3a)$$

$$T'_{ik} = \mu'_{ik} \partial_i u_k + \mu'_{ki} \partial_k u_i \quad (i \neq k). \quad (3b)$$

Here (i, k) take on values $(1, 2, 3)$ and (T'_{ik}, u_i, x_i) are scalar components of $(\mathbf{T}', \mathbf{u}, \mathbf{x})$. Operator ∂_i is the component of the gradient ∇ associated with coordinate x_i , and $(\lambda'_{ik}, \mu'_{ik})$ are generalized Lamé constants defined by

$$(\lambda'_{ik}, \mu'_{ik}) = (\lambda_{ik}, \mu_{ik}) \lambda_k^2, \quad (4a)$$

$$\frac{1}{2} \lambda_{ik} = \frac{\partial \alpha_0}{\partial \lambda_k^2} + \lambda_i^2 \frac{\partial \alpha_1}{\partial \lambda_k^2} + \lambda_i^4 \frac{\partial \alpha_2}{\partial \lambda_k^2}, \quad (4b)$$

$$\mu_{ik} = \mu_{ki} = \alpha_1 + \alpha_2 (\lambda_i^2 + \lambda_k^2). \quad (4c)$$

Because configuration \mathfrak{R}_0 is homogeneous, the perturbation balance of linear momentum in a Cartesian basis reduces to

$$\nabla \cdot \mathbf{T}' = \rho \ddot{\mathbf{u}} + \mathbf{Q}. \quad (5)$$

Here ρ is mass density, \mathbf{Q} is a body force associated with \mathbf{u} , and a superposed dot signifies time differentiation. Perturbation traction on a surface in \mathfrak{R}^* with outwardly directed normal \mathbf{n} is given by vector

$$\mathbf{t}'^{(n)} = \mathbf{T}' \mathbf{n} + \mathbf{T} \mathbf{n} [\mathbf{n} \cdot (\nabla \mathbf{u}) \mathbf{n}] - \mathbf{T} (\nabla \mathbf{u})^T \mathbf{n}. \quad (6)$$

In a principal basis, a Hadamard material can, in view of (1), be characterized by

$$\alpha_0 = 2J \frac{dG(J)}{dJ}, \quad \alpha_1 = \frac{1}{\sqrt{J}} (a_0 - b_0 I), \quad \alpha_2 = \frac{b_0}{\sqrt{J}}, \quad (7a)$$

$$I = \lambda_1^2 + \lambda_2^2 + \lambda_3^2, \quad II = \lambda_1^2 \lambda_2^2 + \lambda_2^2 \lambda_3^2 + \lambda_3^2 \lambda_1^2, \quad J = \lambda_1^2 \lambda_2^2 \lambda_3^2. \quad (7b)$$

Here $G(1) = 0$ and (a_0, b_0) are material constants, where $a_0 - b_0 = \mu$ and μ is the shear modulus for infinitesimal deformation. A simple model for the subclass of compressible isotropic neo-Hookean materials arises when [Brock 2001; Brock and Georgiadis 2001]

$$b_0 = 0, \quad G(J) = \mu \left(\frac{1}{\sqrt{J}} - 1 \right). \quad (8)$$

Such a material for infinitesimal deformations exhibits a Poisson's ratio of 0.25. Use of (7) and (8) in (3) and (4) gives the constitutive forms

$$\frac{1}{\mu} T'_{11} = B_1 \partial_1 u_1 + \left(\frac{2}{J} - b_1 \right) (\partial_2 u_2 + \partial_3 u_3), \quad (9a)$$

$$\frac{1}{\mu} T'_{22} = B_2 \partial_2 u_2 + \left(\frac{2}{J} - b_2 \right) (\partial_3 u_3 + \partial_1 u_1), \quad (9b)$$

$$\frac{1}{\mu} T'_{33} = B_3 \partial_3 u_3 + \left(\frac{2}{J} - b_3 \right) (\partial_1 u_1 + \partial_2 u_2), \quad (9c)$$

$$T'_{ik} = T'_{ki} = \mu [(b\partial)_i u_k + (b\partial)_k u_i] \quad (i \neq k). \quad (9d)$$

In (9) dimensionless parameters

$$b_k = \frac{\lambda_k^2}{\sqrt{J}}, \quad B_k = \frac{2}{J} + b_k. \quad (10)$$

In (9d) and (10), (i, k) take on values $(1, 2, 3)$. Equations (6) and (9) for a surface in \mathfrak{N}^* with an outwardly directed normal in the negative x_3 -direction give $t_3^{(-3)} = -T'_{33}$ and, for $k = (1, 2)$,

$$t_k^{(-3)} = -\mu \left(\frac{1}{J} \partial_k u_3 + b_3 \partial_3 u_k \right). \quad (11)$$

In view of (1) and (7b) the principal stretches λ_k are obtained as functions of the homogeneous principal Cauchy stress T_k from the coupled nonlinear equations

$$\frac{T_k}{\mu} + \frac{1}{J} - b_k = 0 \quad \left(\frac{T_k}{\mu} < \frac{1}{J} \right). \quad (12)$$

The parenthetical restriction on tensile Cauchy stress guarantees that coefficients in (9) are nonnegative. Tensile stress of the same order of magnitude as μ is not precluded, for example, $(T_k)_{\max} < \mu/\sqrt{2}$ in plane strain [Brock 2001; Brock and Georgiadis 2001]. For convenience the temporal variable $\tau = v_0 \times$ time is introduced, where $v_0 = \sqrt{\mu/\rho}$ is the rotational wave speed for isotropic infinitesimal deformation. Thus $(\mathbf{u}, \mathbf{T}')$ are functions of (\mathbf{x}, τ) , and (5) and (9) combine to give

$$\frac{2}{J} \nabla(\nabla \cdot \mathbf{u}) + (\nabla_S^2 - \partial^2) \mathbf{u} = \frac{\mathbf{Q}}{\mu} \quad (\tau > 0), \quad (13a)$$

$$(\mathbf{u}, \mathbf{T}', \mathbf{Q}) \equiv 0 \quad (\tau \leq 0). \quad (13b)$$

Here ∂ signifies differentiation with respect to τ . We now introduce operators

$$\nabla_S^2 = b_k \partial_k^2, \quad \nabla_D^2 = B_k \partial_k^2 = \nabla_S^2 + \frac{2}{J} \nabla^2. \quad (14)$$

The summation convention applies and ∇^2 is the Laplacian. For the homogeneous case (13a) lends itself to a decomposition of Helmholtz type [Achenbach 1973]:

$$\mathbf{u} = \mathbf{u}_D + \mathbf{u}_S, \quad (15a)$$

$$(\nabla_S^2 - \partial^2)\mathbf{u}_S = 0, \quad \nabla \cdot \mathbf{u}_S = 0, \quad (15b)$$

$$(\nabla_D^2 - \partial^2)\mathbf{u}_D = 0, \quad \mathbf{u}_D = \nabla \mathbf{u}_D. \quad (15c)$$

3. Concentrated force

Convolution of the concentrated force solution can be used to study the effect of dynamically induced body forces on equilibrium configuration \mathfrak{N} . In this case \mathfrak{N} is unbounded, and nonequilibrium configuration \mathfrak{N}^* arises due to imposition for $\tau > 0$ of a concentrated force at $\mathbf{x} = 0$, that is,

$$\mathbf{Q} = \mathbf{P}(\tau)\delta(x_1)\delta(x_2)\delta(x_3). \quad (16)$$

Here δ is the Dirac function and $\mathbf{P} \equiv 0$ ($\tau < 0$). After [Stakgold 1967] we treat \mathfrak{N} as half-spaces $x_3 > 0$ and $x_3 < 0$. The homogeneous form of (13a) is the field equation in each half-space, and (16) and the welding of the half-spaces are manifested as conditions for $\tau > 0$ on interface $x_3 = 0$:

$$[\mathbf{u}]_{\pm}^{\pm} = 0, \quad (17a)$$

$$b_3[\partial_3 u_k]_{\pm}^{\pm} + \frac{2}{J}[\partial_k u_3]_{\pm}^{\pm} = \frac{1}{\mu} P_k(\tau)\delta(x_1)\delta(x_2), \quad k = (1, 2), \quad (17b)$$

$$\frac{2}{J}[\partial_1 u_1]_{\pm}^{\pm} + \frac{2}{J}[\partial_2 u_2]_{\pm}^{\pm} + B_3[\partial_3 u_3]_{\pm}^{\pm} = \frac{1}{\mu} P_3(\tau)\delta(x_1)\delta(x_2). \quad (17c)$$

Here $[f]_{\pm}^{\pm}$ signifies a jump in quantity f as the interface is crossed from half-space $x_3 < 0$ to half-space $x_3 > 0$. Solutions to (13)–(15) and (17) must be bounded above as $|\mathbf{x}| \rightarrow \infty$ for finite $\tau > 0$.

To obtain these solutions, unilateral and multiple bilateral Laplace transforms are introduced [van der Pol and Bremmer 1950; Sneddon 1972]:

$$\hat{f} = \int f(\tau) \exp(-p\tau) d\tau, \quad (18a)$$

$$f^* = \iint \hat{f}(x_1, x_2) \exp p(-q_1 x_1 - q_2 x_2) dx_1 dx_2. \quad (18b)$$

For $\text{Re}(p) > 0$ and $\text{Re}(q_1, q_2) = 0$ integration can be taken over the positive τ -axis for (18a), and over the entire x_1 - and x_2 -axes for (18b). Application of (18) to the homogeneous form of (13a) in view of (13b) and (15) gives for $x_3 > 0(+)$ and $x_3 < 0(-)$

$$\mathbf{u}_S^* = (U_1^{\pm}, U_2^{\pm}, U_3^{\pm}) \exp(-p\omega_S|x_3|), \quad (19a)$$

$$q_1 U_1^{\pm} + q_2 U_2^{\pm} \mp \omega_S U_3^{\pm} = 0, \quad (19b)$$

$$\mathbf{u}_D^* = p(q_1, q_2, \mp \omega_D) U_D^{\pm} \exp(-p\omega_D|x_3|). \quad (19c)$$

In (19) (ω_S, ω_D) are radicals:

$$\omega_S = \frac{1}{\sqrt{b_3}} \sqrt{1 - b_1 q_1^2 - b_2 q_2^2}, \quad \text{Re}(\omega_S) \geq 0, \quad (20a)$$

$$\omega_D = \frac{1}{\sqrt{B_3}} \sqrt{1 - B_1 q_1^2 - B_2 q_2^2}, \quad \text{Re}(\omega_D) \geq 0. \quad (20b)$$

Application of (18) to (17) and substitution of (19) gives the results

$$p^2 U_D^\pm = \frac{1}{2\mu\Delta} \left[\pm \hat{P}_3 - \frac{1}{\omega_S} (q_1 \hat{P}_1 + q_2 \hat{P}_2) \right], \quad (21a)$$

$$p U_k^\pm = \frac{-\hat{P}_k}{2\mu b_3 \omega_S} - p^2 q_k U_D^\pm, \quad k = (1, 2). \quad (21b)$$

Here $k = (1, 2)$ and

$$\Delta = 1 + (b_1 - b_3)q_1^2 + (b_2 - b_3)q_2^2. \quad (22)$$

4. Transform inversion

The inversion operation for (18b) is [van der Pol and Bremmer 1950; Sneddon 1972]

$$\hat{f}(x_1, x_2) = \left(\frac{p}{2\pi i} \right)^2 \iint f^* \exp p(q_1 x_1 + q_2 x_2) dq_1 dq_2. \quad (23)$$

If there are no branch points or poles there, integration can be taken along the entire $\text{Im}(q_1)$ and $\text{Im}(q_2)$ -axes. In view of (19) and (21), f^* for any contribution to (\hat{u}_S, \hat{u}_D) exhibits one of the following forms:

$$f^* = \frac{1}{\Delta} \left(q_k, \frac{q_k^2}{\omega}, \omega \right) \exp(-p\omega|x_3|), \quad (24a)$$

$$f^* = \frac{1}{\omega} \exp(-p\omega|x_3|). \quad (24b)$$

Here $k = (1, 2)$ and $\omega = (\omega_S, \omega_D)$. Thus for $x_3 > 0(+)$ and $x_3 < 0(-)$ the right-hand side of (23) reduces to the operations

$$(\mp \partial_3 \partial_k, \partial_k^2, \partial_3^2) \left(\frac{1}{2\pi i} \right)^2 \iint \exp(p(q_1 x_1 + q_2 x_2 - \omega|x_3|)) \frac{dq_1 dq_2}{\Delta \omega}, \quad (25a)$$

$$\left(\frac{1}{2\pi i} \right)^2 \iint \exp(p(q_1 x_1 + q_2 x_2 - \omega|x_3|)) \frac{dq_1 dq_2}{\omega}. \quad (25b)$$

For the integration procedure, results in [Brock 2012; 2013] suggest transformations

$$q_1 = q \cos \psi, \quad q_2 = q \sin \psi, \quad (26a)$$

$$\begin{bmatrix} x_1 \\ x_2 \end{bmatrix} = \begin{bmatrix} \cos \psi & -\sin \psi \\ \sin \psi & \cos \psi \end{bmatrix} \begin{bmatrix} x \\ y \end{bmatrix}. \quad (26b)$$

Here $|\psi| < \pi/2$ and $|x, y, \text{Im}(q)| < \infty$, and (q, ψ) and $(y=0, x, \psi)$ form quasipolar coordinate systems.

Thus the integration procedures in (25a) and (25b) respectively become

$$\frac{1}{i\pi} \int_{\Psi} d\psi \frac{1}{2\pi i} \int \frac{|q|}{\Delta\omega} \exp p(qx - \omega|x_3|) dq, \quad (27a)$$

$$\frac{1}{i\pi} \int_{\Psi} \frac{|q|}{\omega} \exp(qx - \omega|x_3|) dq. \quad (27b)$$

Here Ψ signifies integration over the range $|\psi| < \pi/2$, and integration with respect to q is over the entire $\text{Im}(q)$ -axis. In (27)

$$\Delta = 1 + (b_3 - b)q^2, \quad (28a)$$

$$\omega_S = \frac{1}{\sqrt{b_3}} \sqrt{1 - bq^2}, \quad b = b_1 \cos^2 \psi + b_2 \sin^2 \psi, \quad (28b)$$

$$\omega_D = \frac{1}{\sqrt{B_3}} \sqrt{1 - Bq^2}, \quad B = \frac{2}{J} + b. \quad (28c)$$

Equation (28) shows that conditions $\text{Re}(\omega_S) \geq 0$ and $\text{Re}(\omega_D) \geq 0$ hold in the q -plane with cuts $\text{Im}(q) = 0$, $|\text{Re}(q)| > 1/\sqrt{b}$ and $\text{Im}(q) = 0$, $|\text{Re}(q)| > 1/\sqrt{B}$, respectively. When $b_3 > b$, Δ in (27a) exhibits roots $q = \pm 1/\sqrt{b - b_3}$. Because $\sqrt{B} > \sqrt{b} > \sqrt{b - b_3}$ these lie on the branch cuts of (ω_S, ω_D) . For $b > b_3$ roots $q = \pm i/\sqrt{b_3 - b}$ lie on the $\text{Im}(q)$ -axis, so that deformations in the integration contour in (27a) are required. Instead the de Hoop method [de Hoop 1960] is employed to change the integration contour to a path in the q -plane parametrized by the positive real variable t . Thus (27a) gives

$$\frac{1}{i\pi} \int_{\Psi} d\psi \frac{1}{i\pi} \text{Re} \int \exp(-pt) \frac{q_+ q'_+ dt}{\Delta(q_+) \omega(q_+)}. \quad (29)$$

For the case ω_S , t -integration is over the range (S, ∞) and

$$\sqrt{b} S^2 q_+ = -\frac{tx}{\sqrt{b}} + i \frac{|x_3|}{\sqrt{b_3}} \sqrt{t^2 - S^2}, \quad q'_+ = i \sqrt{\frac{b_3}{b}} \frac{\omega_S(q_+)}{\sqrt{t^2 - S^2}}. \quad (30a)$$

For the case ω_D , t -integration is over the range (D, ∞) and

$$\sqrt{B} D^2 q_+ = -\frac{tx}{\sqrt{B}} + i \frac{|x_3|}{\sqrt{B_3}} \sqrt{t^2 - D^2}, \quad q'_+ = i \sqrt{\frac{B_3}{B}} \frac{\omega_D(q_+)}{\sqrt{t^2 - D^2}}. \quad (30b)$$

Parameters (S, D) are given by

$$S = \sqrt{\frac{x^2}{b} + \frac{x_3^2}{b_3}}, \quad D = \sqrt{\frac{x^2}{B} + \frac{x_3^2}{B_3}}. \quad (31)$$

Taking the real part of the integrand in (29) gives for (ω_S, ω_D) , respectively,

$$-\frac{|x_3|}{\pi^2} \int_{\Psi} \frac{d\psi}{S^2} \int_S^{\infty} \frac{N_S}{M} \exp(-pt) dt, \quad -\frac{|x_3|}{\pi^2} \int_{\Psi} \frac{d\psi}{D^2} \int_D^{\infty} \frac{N_D}{M} \exp(-pt) dt. \quad (32a)$$

The analogous result for (27b) is

$$-\frac{|x_3|}{\pi^2 p} \int_{\Psi} \frac{d\psi}{b S^2} \exp(-pS), \quad -\frac{|x_3|}{\pi^2 p} \int_{\Psi} \frac{d\psi}{B D^2} \exp(-pD). \quad (32b)$$

In (32a) (M, N_S, N_D) are given by

$$M = [(b - b_3)t^2 - r^2]^2 + 2t^2(b - b_3)x_3^2, \quad (33a)$$

$$N_S = (b_3 - b) \left[\frac{2x^2}{b} + (b - b_3) \left(\frac{x^2}{b} - \frac{x_3^2}{b_3} \right) \right] t^2 - r^2 S^2, \quad (33b)$$

$$N_D = (b_3 - b) \left[\frac{2x^2}{B} + (b - b_3) \left(\frac{x^2}{B} - \frac{x_3^2}{B_3} \right) \right] t^2 - r^2 D^2. \quad (33c)$$

In (30)–(33) $r = \sqrt{x^2 + x_3^2}$, where $x = x_1 \cos \psi + x_2 \sin \psi$. Equations (21), (25), and (32) show that explicit dependence of $(\hat{\mathbf{u}}_S, \hat{\mathbf{u}}_D)$ on transform parameter p is confined to products $\hat{P}_k \exp(-pt)$. Inversion of $(\hat{\mathbf{u}}_S, \hat{\mathbf{u}}_D)$ can then be, in view of (18a) and (24), performed by inspection. For the case of common temporal load behavior $\mathbf{P}(\tau) = \mathbf{P}\delta(\tau)$ (15a) gives

$$\mathbf{u} = \frac{1}{2\pi^2} (\mathbf{P} \cdot \nabla) \nabla |x_3| \int_{\Psi} d\psi \left[\int_D^{\tau} \frac{N_D}{MD^2} dt - \int_S^{\tau} \frac{N_S}{MS^2} dt \right] + \frac{1}{2\pi^2} \mathbf{P} \nabla^2 |x_3| \int_{\Psi} \frac{d\psi}{bS^2} (\tau - S). \quad (34)$$

Wave speeds (v_S, v_D) associated with the integration terms in (34) can be obtained by introducing the quasispherical coordinate system

$$x_1 = X \cos \theta \sin \phi, \quad x_2 = X \sin \theta \sin \phi, \quad x_3 = X \cos \phi. \quad (35)$$

Here $|X| < \infty$, $|\theta| < \pi/2$, $0 < \phi < \pi/2$, and in view of (31),

$$v_S = c_S v_0, \quad v_D = c_D v_0, \quad (36a)$$

$$c_S = \frac{\sqrt{b_3 b}}{\sqrt{b_3 \sin^2 \phi + b \cos^2 \phi}}, \quad b = b_1 \cos^2 \theta + b_2 \sin^2 \theta, \quad (36b)$$

$$c_D = \frac{\sqrt{B_3 B}}{\sqrt{B_3 \sin^2 \phi + B \cos^2 \phi}}, \quad B = \frac{2}{J} + b. \quad (36c)$$

5. Displacement discontinuity

In this instance configuration \aleph^* arises in unbounded \aleph due to the existence for $\tau > 0$ of a finite discontinuity in displacement at $\mathbf{x} = 0$. Convolution of the solution for this problem can be used to study dynamic perturbation of \aleph by formation of a crack on the plane $x_3 = 0$. We again treat two half-spaces $x_3 > 0(+)$ and $x_3 < 0(-)$. Equations (13)–(15) are valid for $x_3 \neq 0$, with $\mathbf{Q} \equiv 0$, but Equation (17) for $x_3 = 0$, $\tau > 0$ is replaced with

$$[\mathbf{u}]_{\pm}^+ = \mathbf{U}^C(\tau) \delta(x_1) \delta(x_2), \quad \mathbf{t}'^{(3)} + \mathbf{t}'^{(-3)} = 0. \quad (37)$$

Here \mathbf{U}^C vanishes for $\tau \leq 0$, but for $\tau > 0$ it is continuous and bounded above. The transform operation (18) produces (19), (20), and (22), with (U_D^{\pm}, U_k^{\pm}) now given by

$$pU_D^\pm = -\frac{\beta_3}{2}\hat{U}_3^C - \frac{1}{2\Delta}\left[\left(\frac{1}{J} + b_3\right)\frac{\omega_D}{b_3}\hat{U}_3^C \mp 2(q_1\hat{U}_1^C + q_2\hat{U}_2^C)\right], \quad (38a)$$

$$U_k^\pm = \pm\frac{1}{2}\hat{U}_k^C + \frac{q_k}{2\Delta}\left[\left(\frac{1}{J} + b_3\right)\frac{\omega_S}{b_3}\hat{U}_3^C \mp 2(q_1\hat{U}_1^C + q_2\hat{U}_2^C)\right], \quad (38b)$$

$$\beta_3 = \frac{1}{(Jb_3)^2}\left(\frac{2}{2+Jb_3} - b_3\right). \quad (38c)$$

In (38) $k = (1, 2)$, and comparison of (21) and (38) indicates that (25) is replaced by

$$(\mp\partial_3\partial_k^2, \partial_k\partial_3^2)\left(\frac{1}{2\pi i}\right)^2 \iint \exp p(q_1x_1 + q_2x_2 - \omega|x_3|) \frac{dq_1 dq_2}{p\Delta\omega}, \quad (39a)$$

$$(\mp\partial_3, \partial_k)\left(\frac{1}{2\pi i}\right)^2 \iint \exp p(q_1x_1 + q_2x_2 - \omega|x_3|) p \frac{dq_1 dq_2}{\omega}. \quad (39b)$$

The transform inversion process involving (19), (20), (22), and (39) is similar to that for the concentrated force problem. For the case $U^C(\tau) = U^C$ the results are

$$\begin{aligned} \mathbf{u} = \mathbf{u}^D + \mathbf{u}^S + \frac{U_k^C}{2\pi^2} \nabla\partial_3\partial_k|x_3| \int_{\Psi} d\psi \left[\int_D^{\tau} \frac{N_D}{MD^2}(\tau-t) dt - \int_S^{\tau} \frac{N_S}{MS^2}(\tau-t) dt \right] \\ + \frac{U_3^C}{2\pi^2} \left(1 + \frac{1}{Jb_3}\right) \nabla\partial_3^2|x_3| \int_{\Psi} d\psi \left[\int_D^{\tau} \frac{N_D}{MD^2}(\tau-t) dt - \int_S^{\tau} \frac{N_S}{MS^2}(\tau-t) dt \right], \end{aligned} \quad (40a)$$

$$\mathbf{u}^D = \frac{U_3^C}{2\pi^2} \nabla|x_3| \int_{\Psi} \frac{\beta_3}{BD^2} d\psi H(\tau - D), \quad (40b)$$

$$\mathbf{u}_k^S = \frac{U_k^C}{2\pi^2} \partial_3|x_3| \int_{\Psi} \frac{d\psi}{bS^2} H(\tau - S), \quad (40c)$$

$$\mathbf{u}_3^S = \frac{1}{2\pi^2} \left[U_k^C \partial_k + U_3^C \left(1 + \frac{1}{Jb_3}\right) \partial_3 \right] |x_3| \int_{\Psi} \frac{d\psi}{bS^2} H(\tau - S). \quad (40d)$$

Here $\mathbf{u}^D \neq \mathbf{u}_D$ and $\mathbf{u}^S \neq \mathbf{u}_S$, $k = (1, 2)$, the summation convention holds, and H is the unit step function.

6. Behavior on a principal plane: concentrated surface force

Convolution of the solution for this problem can serve as the basis for study of dynamic perturbation by dynamic contact. Thus \mathfrak{R} is the half-space $x_3 > 0$ with traction-free surface $x_3 = 0$. Configuration \mathfrak{N}^* arises due to imposing for $\tau > 0$ the surface load

$$t_k^{(-3)} = -P_{3k}(\tau)\delta(x_1)\delta(x_2). \quad (41)$$

Here $k = (1, 2, 3)$ and $P_{3k} \equiv 0$ ($\tau < 0$) and is bounded above for $\tau > 0$. Because \mathfrak{R} in \mathfrak{N}^* has no surface traction, $T_3 \equiv 0$ and (9c) and (11) give

$$b_3 = \frac{1}{J}, \quad B_3 = \frac{3}{J}, \quad \frac{1}{b_1b_2} = \sqrt{J} \sqrt{\frac{b_1}{b_2}} - \frac{T_1}{\mu} = \sqrt{J} \sqrt{\frac{b_2}{b_1}} - \frac{T_2}{\mu}. \quad (42)$$

Equations (13)–(15), with $\mathbf{Q} \equiv 0$, govern for $(x_3, \tau) > 0$. Application of (18) in view of boundary condition (41) leads to expressions for (U_D^+, U_k^+) . Of interest here is displacement \mathbf{u}^0 on the half-space

surface $x_3 = 0$, and use of these expressions and variables defined by (26) in (23) give the transform

$$\hat{u}^0 = \frac{1}{i\pi} \int_{\Psi} J d\psi \frac{1}{2\pi i} \int \frac{|q| dq}{\mu p R} N \cdot \hat{t}^{(-3)} \exp(pqx), \quad (43a)$$

$$\begin{bmatrix} N_{11} & N_{12} \\ N_{21} & N_{22} \end{bmatrix} = \frac{1}{\omega_S} \begin{bmatrix} N_1 & N_{12} \\ N_{12} & N_2 \end{bmatrix}, \quad \begin{bmatrix} N_{31} \\ N_{32} \end{bmatrix} = - \begin{bmatrix} N_{13} \\ N_{23} \end{bmatrix} = qN \begin{bmatrix} \cos \psi \\ \sin \psi \end{bmatrix}, \quad N_{33} = -\omega_D \Delta. \quad (43b)$$

Again $x = x_1 \cos \psi + x_2 \sin \psi$, but the definition of terms in (43) is influenced by (42):

$$\omega_S = \sqrt{q^2 - T}, \quad \omega_D = \frac{1}{\sqrt{3}} \sqrt{-q^2 - T}, \quad T = (1 + Jb)q^2 - J, \quad (44a)$$

$$N = 2\omega_S \omega_D - T, \quad R = 4q^2 \omega_S \omega_D + T^2, \quad (44b)$$

$$(N_1, N_2) = Mq^2(\cos^2 \psi, \sin^2 \psi) - R, \quad N_{12} = Mq^2 \sin \psi \cos \psi, \quad (44c)$$

$$M = q^2 + \omega_S(2\omega_D - 3\omega_S), \quad \Delta = J + q^2(1 - Jb). \quad (44d)$$

Integration in (43a) is along the entire $\text{Im}(q)$ -axis but, as a special case of (30), the contour can be changed to a path around branch cuts on the $\text{Re}(q)$ -axis. In view of (44a) the branch points are defined by $q = \pm(1/\sqrt{b}, 1/\sqrt{B})$. In addition, the Rayleigh function R exhibits real roots $q = \pm q_R$, where $q_R > 1/\sqrt{b}$ and is defined by

$$q_R = \frac{\sqrt{J}}{\sqrt{Jb + 1 - 2/\sqrt{3}}}. \quad (45)$$

These values of q define the body wave speeds (v_S, v_D)—see (36)—and the Rayleigh speed v_R in the principal plane $x_3 = 0$:

$$v_S = c_S v_0, \quad v_D = c_D v_0, \quad v_R = c_R v_0, \quad (46a)$$

$$c_S = \sqrt{b}, \quad c_D = \sqrt{B}, \quad c_R = \sqrt{b + \frac{1}{J} \left(1 - \frac{2}{\sqrt{3}}\right)}, \quad (46b)$$

$$b = b_1 \cos^2 \theta + b_2 \sin^2 \theta, \quad B = \frac{2}{J} + b. \quad (46c)$$

In (46c) quasipolar coordinate $|\theta| < \pi/2$ is measured with respect to the x_1 -direction in the principal plane. Changing the integration path by means of the Cauchy theorem gives expressions that can be inverted by inspection. For the step function $P_{3k}(\tau) = P_{3k}H(\tau)$,

$$u_1^0 = J \int_{\Psi} U_0 \cos \psi d\psi + \frac{JP_{31}}{\mu\pi^2} \int_{\Psi} \frac{q d\psi}{\Omega_S x} H\left(\tau - \frac{|x|}{c_S}\right), \quad (47a)$$

$$u_2^0 = J \int_{\Psi} U_0 \sin \psi d\psi + \frac{JP_{32}}{\mu\pi^2} \int_{\Psi} \frac{q d\psi}{\Omega_S x} H\left(\tau - \frac{|x|}{c_S}\right), \quad (47b)$$

$$u_3^0 = J \int_{\Psi} U_3 d\psi. \quad (47c)$$

Equation (47) involves the definitions $P_{12} = P_{31} \cos \psi + P_{32} \sin \psi$ and

$$U_0 = \frac{P_{33}}{\mu\pi^2x} \frac{6q^2T\Omega_D\omega_S}{(3T^2 - 4q^4)(T + 2q^2)} H\left(\tau - \frac{|x|}{c_D}\right) H\left(\frac{|x|}{c_S} - \tau\right) - \frac{JP_{33}}{\mu\pi c_R} \frac{(\sqrt{3} - 1) \operatorname{sgn}(x)}{8 - 3\sqrt{3}(1 + Jb)} \delta\left(\tau - \frac{|x|}{c_R}\right) - \frac{P_{12}}{\mu\pi^2x} \frac{3q^3}{(3T^2 - 4q^4)(T + 2q^2)} \times 4\Omega_D\Omega_S H\left(\tau - \frac{|x|}{c_D}\right) + \frac{16q^2\Omega_D\Omega_S^2 - 3T^3}{\Omega_S(T - 2q^2)} H\left(\tau - \frac{|x|}{c_S}\right), \quad (48a)$$

$$U_3 = -\frac{P_{12}}{\mu\pi^2x} \frac{6q^2T\Omega_D\omega_S}{(3T^2 - 4q^4)(T + 2q^2)} H\left(\tau - \frac{|x|}{c_D}\right) H\left(\frac{|x|}{c_S} - \tau\right) + \frac{JP_{12}}{\mu\pi c_R} \frac{(\sqrt{3} - 1) \operatorname{sgn}(x)}{8 - 3\sqrt{3}(1 + Jb)} \delta\left(\tau - \frac{|x|}{c_R}\right) + \frac{P_{33}}{\mu\pi^2x} \frac{3qT\Omega_D}{(3T^2 - 4q^4)(T^2 - 4q^4)} \times T^2 H\left(\tau - \frac{|x|}{c_D}\right) + 4q^2\Omega_S\Omega_D H\left(\tau - \frac{|x|}{c_S}\right), \quad (48b)$$

$$\Omega_S = \sqrt{T - q^2}, \quad \Omega_D = \frac{1}{\sqrt{3}} \sqrt{T + q^2}, \quad q = \frac{\tau}{x}. \quad (48c)$$

7. Dimensionless speed values

The \mathfrak{R} considered here is an idealized isotropic neo-Hookean solid with an effective Poisson's ratio of 0.25 for infinitesimal strain. It is chosen for purposes of illustration and, therefore, sample values of dimensionless speeds (c_S , c_D) in (36) are given for the spherical octant $0 \leq (\theta, \phi) \leq 90^\circ (\pi/2)$ in Tables 1 and 2. Configuration \mathfrak{R} results from the plane strain defined by $\lambda_3 = 1$ and $T_1 + T_2 = 0$, so that (9c) and (11) give

$$b_1 = \sqrt{\frac{\chi}{\sqrt{J}}}, \quad b_2 = \frac{1}{\sqrt{\chi\sqrt{J}}}, \quad b_3 = \frac{1}{\sqrt{J}}, \quad B_k = \frac{2}{J} + b_k, \quad (49a)$$

$$J = \frac{2\chi}{1 + \chi^2}, \quad \chi = \frac{T_1}{\mu} + \sqrt{1 + \left(\frac{T_1}{\mu}\right)^2}, \quad \frac{T_3}{\mu} = \frac{1}{\sqrt{J}} - \frac{1}{J}. \quad (49b)$$

	$\phi = 0^\circ$	15°	30°	45°	60°	75°	90°
$\theta = 0^\circ$	1.04811	1.04847	1.04945	1.05080	1.05215	1.05314	1.05351
15°	1.04811	1.04813	1.04817	1.04824	1.04830	1.04835	1.04837
30°	1.04811	1.04070	1.04459	1.04110	1.03765	1.03515	1.03423
45°	1.04811	1.04578	1.03942	1.03095	1.02268	1.01675	1.01460
60°	1.04811	1.04425	1.03392	1.02030	1.00720	0.99779	0.99459
75°	1.04811	1.04307	1.29664	1.01216	0.99552	0.98385	0.97917
90°	1.04811	1.04262	1.02805	1.00911	0.99117	0.97863	0.97416

Table 1. Dimensionless speed c_S in spherical octant $0 \leq (\theta, \phi) \leq 90^\circ$ for $T_1/\mu = 0.2$.

	$\phi = 0^\circ$	15°	30°	45°	60°	75°	90°
$\theta = 0^\circ$	1.77148	1.77169	1.77228	1.77308	1.77388	1.77446	1.77467
15°	1.77148	1.77149	1.77152	1.77156	1.77160	1.77162	1.77163
30°	1.77148	1.77093	1.76943	1.76738	1.76534	1.76385	1.76331
45°	1.77148	1.77014	1.76651	1.76159	1.75671	1.75316	1.75186
60°	1.77148	1.76934	1.76354	1.75571	1.74798	1.74238	1.74035
75°	1.77148	1.76874	1.76132	1.75134	1.74152	1.73444	1.73187
90°	1.77148	1.76852	1.76050	1.74973	1.73915	1.73152	1.72876

Table 2. Dimensionless speed c_D in spherical octant $0 \leq (\theta, \phi) \leq 90^\circ$ for $T_1/\mu = 0.2$.

$T_1/\mu =$	-0.2	-0.1	0.1	0.2
$\theta = 0^\circ$	0.94068	0.97015	1.03015	1.01227
15°	0.92778	0.97360	1.02689	1.05418
30°	0.96691	0.98296	1.01794	1.03667
45°	0.99243	0.99560	1.00558	1.01226
60°	1.01731	1.00808	0.99307	0.98725
75°	1.03515	1.01712	0.98380	0.96855
90°	1.04160	1.02041	0.98039	0.96159

Table 3. Dimensionless speed c_S in circular quadrant $0 \leq \theta \leq 90^\circ$ for various T_1 .

$T_1/\mu =$	-0.2	-0.1	0.1	0.2
$\theta = 0^\circ$	1.74779	1.73887	1.72729	1.72453
15°	1.75162	1.74079	1.72535	1.72064
30°	1.76204	1.74604	1.72004	1.70997
45°	1.77618	1.75319	1.71275	1.69528
60°	1.79020	1.76031	1.70544	1.68047
75°	1.80039	1.76550	1.70006	1.66955
90°	1.80411	1.76740	1.69809	1.66552

Table 4. Dimensionless speed c_D in circular quadrant $0 \leq \theta \leq 90^\circ$ for various T_1 .

Because (49b) gives $J < 1$, any finite $|T_1|$ satisfies the parenthetical restriction in (11). In similar fashion dimensionless speeds (c_S, c_D, c_R) associated with principal plane $x_3 = 0$ in (45) are given for the circular quadrant $0 \leq \theta \leq 90^\circ(\pi/2)$ in Tables 3, 4, and 5. Here \aleph is induced by uniaxial loading $(T_2, T_3) = 0$. Equations (9), (11), and (42) give

$$b_1 = J^{3/2}, \quad (b_2, b_3) = \frac{1}{J}, \quad J^{5/2} - \frac{T_1}{\mu} J - 1 = 0 \quad \left(\frac{T_1}{\mu} < \frac{1}{2^{0.4}} \right). \quad (50)$$

In this case the restriction in (11) imposes a tension limit on T_1 . Equations (9)–(11) show that a nonhydrostatic principal stress in \aleph gives configuration \aleph , whose infinitesimal perturbation response is anisotropic. Even for the simple nonhydrostatic cases chosen, the data in Tables 1–5 clearly illustrate this behavior.

$T_1/\mu =$	-0.2	-0.1	0.1	0.2
$\theta = 0^\circ$	0.84679	0.88324	0.95526	0.99078
15°	0.85467	0.88703	0.95174	0.98400
30°	0.87582	0.89729	0.94207	0.96521
45°	0.90392	0.91112	0.92871	0.93895
60°	0.93118	0.92474	0.91514	0.91193
75°	0.95063	0.93458	0.90508	0.89165
90°	0.95765	0.93816	0.90138	0.88409

Table 5. Dimensionless speed c_R in circular quadrant $0 \leq \theta \leq 90^\circ$ for various T_1 .

8. Comments

Equations (34), (40), and (47) express exact transient solutions as integrals with respect to quasipolar angle measure $|\psi| < \pi/2$. Equations (34) and (47) also exhibit integration with respect to a temporal variable t . This integration can, in fact, be performed with use of standard tables [Pierce and Foster 1956; Gradshteyn and Ryzhik 1980], but the results are cumbersome; for example, in (34), for $b > b_3$:

$$|x_3| \int_S^\tau \frac{N_S}{M} dt = \frac{1}{2\sqrt{r^2+x^2}} \operatorname{Im} \frac{r^2 S^2 + A_S T}{\sqrt{(b-b_3)T}} \times \ln \frac{\sqrt{T} - \tau\sqrt{b-b_3}}{\sqrt{T} - S\sqrt{b-b_3}} \frac{\sqrt{T} + S\sqrt{b-b_3}}{\sqrt{T} + \tau\sqrt{b-b_3}}, \quad (51a)$$

$$A_S = 2\frac{x^2}{b} + (b-b_3) \left(\frac{x^2}{b} - \frac{x_3^2}{b_3} \right), \quad T = x^2 + i|x_3|\sqrt{r^2+x^2}. \quad (51b)$$

Here $\sqrt{b-b_3} \rightarrow i\sqrt{b_3-b}$ when $b_3 > b$. Use of a quasipolar measure, therefore, renders (34), (40), and (47) as a “hybrid” of quasipolar and principal Cartesian coordinates, as well as general operators $(\nabla, \nabla^2, \mathbf{f} \cdot \mathbf{q})$. Moreover, dimensionless speeds (c_S, c_D) associated with (34) and (40) involve quasi-spherical measure (θ, ϕ) , and (c_S, c_D, c_R) involve quasipolar measure θ . Nevertheless, the form of (34), (40), and (47) is not complicated and is similar to corresponding results for the linear isotropic case, compare (34) and [Achenbach 1973, Equation (3.92)].

This type of similarity is well known for linear quasistatic anisotropic results [Ting 1996]. Indeed, in light of results such as [Ting 1996; Jones 1999] it is often useful to categorize superimposed infinitesimal deformation equations in accordance with classes of anisotropic materials, for example, [Green and Zerna 1968; Beatty and Usmani 1975]. Due to the idealized neo-Hookean \mathfrak{H} treated, this article took an ad hoc solution approach. However, the approach itself may be useful in generation of singular transient solutions in linear anisotropic solids [Willis 1965; Wang and Achenbach 1992], and such efforts are underway.

References

- [Achenbach 1973] J. D. Achenbach, *Wave propagation in elastic solids*, North-Holland, Amsterdam, 1973.
- [Beatty and Usmani 1975] M. F. Beatty and S. A. Usmani, “On the indentation of a highly elastic half-space”, *Quart. J. Mech. Appl. Math.* **28** (1975), 47–62.
- [Brock 2001] L. M. Brock, “Rapid sliding contact on a highly elastic pre-stressed material”, *Int. J. Non-Linear Mech.* **36** (2001), 433–442.

- [Brock 2012] L. M. Brock, “Two cases of rapid contact on an elastic half-space: sliding ellipsoidal die, rolling sphere”, *J. Mech. Mater. Struct.* **7**:5 (2012), 469–483.
- [Brock 2013] L. M. Brock, “Rapid contact on a pre-stressed highly elastic half-space: the sliding ellipsoid and rolling sphere”, *J. Appl. Mech. (ASME)* **80**:2 (2013), Art. ID # 021023.
- [Brock and Georgiadis 2001] L. M. Brock and H. G. Georgiadis, “An illustration of sliding contact at any constant speed on highly elastic half-spaces”, *IMA J. Appl. Math.* **66**:6 (2001), 551–566.
- [Gradshteyn and Ryzhik 1980] I. S. Gradshteyn and I. M. Ryzhik, *Table of integrals, series and products*, Academic, New York, 1980.
- [Green and Zerna 1968] A. E. Green and W. Zerna, *Theoretical elasticity*, 2nd ed., Clarendon, Oxford, 1968.
- [de Hoop 1960] A. T. de Hoop, “A modification of Cagniard’s method for solving seismic pulse problems”, *Appl. Sci. Res. B* **8**:1 (1960), 349–356.
- [Jones 1999] R. M. Jones, *Mechanics of composite materials*, 2nd ed., Taylor and Francis, New York, 1999.
- [Love 1944] A. E. H. Love, *A treatise on the mathematical theory of elasticity*, 4th ed., Dover, New York, 1944.
- [Pierce and Foster 1956] B. O. Pierce and R. M. Foster, *A short table of integrals*, 4th ed., Ginn, Waltham, MA, 1956.
- [van der Pol and Bremmer 1950] B. van der Pol and H. Bremmer, *Operational calculus: based on the two-sided Laplace integral*, Cambridge University Press, Cambridge, 1950.
- [Sneddon 1972] I. N. Sneddon, *The use of integral transforms*, McGraw-Hill, New York, 1972.
- [Stakgold 1967] I. Stakgold, *Boundary value problems of mathematical physics*, vol. 1, MacMillan, New York, 1967.
- [Ting 1996] T. C. T. Ting, *Anisotropic elasticity: theory and applications*, Oxford Engineering Science Series **45**, Oxford University Press, New York, 1996.
- [Truesdell and Noll 1965] C. T. Truesdell and W. Noll, *The non-linear field theories of mechanics*, edited by W. Flugge, *Handbuch der Physik* **III/3**, Springer, Berlin, 1965.
- [Wang and Achenbach 1992] C.-Y. Wang and J. D. Achenbach, “A new look at 2-D time-domain elastodynamic Green’s functions for general anisotropic solids”, *Wave Motion* **16**:4 (1992), 389–405.
- [Willis 1965] J. R. Willis, “The elastic interaction energy of dislocation loops in anisotropic media”, *Quart. J. Mech. Appl. Math.* **18** (1965), 419–433.

Received 7 Aug 2012. Revised 19 Nov 2012. Accepted 22 Nov 2012.

LOUIS MILTON BROCK: brock@engr.uky.edu

Department of Mechanical Engineering, University of Kentucky, 265 Ralph G. Anderson Building, Lexington KY 40506-0503, United States

WAVE VELOCITY FORMULAS TO EVALUATE ELASTIC CONSTANTS OF SOFT BIOLOGICAL TISSUES

PHAM CHI VINH AND JOSE MERODIO

We use the equations governing infinitesimal motions superimposed on a finite deformation in order to establish formulas for the velocity of (plane homogeneous) shear bulk waves and surface Rayleigh waves propagating in soft biological tissues subject to uniaxial tension or compression. Soft biological tissues are characterized as transversely isotropic incompressible nonlinearly elastic solids. The constitutive model is given as a strain-energy density expanded up to fourth order in terms of the Green strain tensor. The velocity formulas are written as $\rho v^2 = a_0 + a_1 e + a_2 e^2$ where ρ is the mass density, v is the wave velocity, a_k are functions in terms of the elastic constants and e is the elongation in the loading direction. These formulas can be used to evaluate the elastic constants since they determine the exact behavior of the elastic constants of second, third, and fourth orders in the incompressible limit.

1. Introduction

Soft biological tissues were generally considered incompressible and isotropic under the early days of their analysis. In more recent years they have been recognized as highly anisotropic due to the presence of collagen fibers [Holzapfel et al. 2000]. Determination of the acoustoelastic coefficients in incompressible solids and the limiting values of the coefficients of nonlinearity for elastic wave propagation, among other studies, has very recently attracted a lot of attention since these analyses give an opportunity to capture the mechanical properties of these materials (see, for instance, Destrade et al. [Destrade et al. 2010b] and references therein). For other applications dealing with linearized dynamics we refer to [Bigoni et al. 2007; 2008] and the references therein.

Hamilton et al. [2004] analyzed a strain-energy density suitable for incompressible isotropic elastic solids such as gels and phantoms, namely

$$W = \mu I_2 + (A/3)I_3 + DI_2^2, \quad (1)$$

where

$$I_2 = \text{tr}(\mathbf{E}^2), \quad I_3 = \text{tr}(\mathbf{E}^3), \quad (2)$$

\mathbf{E} is the Green strain tensor and μ , A , and D are second-, third-, and fourth-order elastic constants, respectively (the order given by the exponent of \mathbf{E}). A very similar expansion to the one given in (1) was originally derived in [Ogden 1974].

Indeed, several investigations have been carried out to determine the elastic constants μ , A and D using shear bulk nonlinear waves [Gennisson et al. 2007; Renier et al. 2007; 2008] and small-amplitude

Keywords: incompressible transversely isotropic elastic solids, soft biological tissues, shear bulk waves, Rayleigh waves, wave velocity, elastic constants.

waves propagating in incompressible solids subject to homogeneous deformations [Destrade et al. 2010b] (linearized waves). It should be noted that if the analysis of a material only includes the small deformation regime then it is enough to consider (1) up to fourth order in strains.

In contrast to gels and phantoms, soft biological tissues are anisotropic solids due to the presence of oriented collagen fiber bundles [Holzapfel et al. 2000; Destrade et al. 2010a]. It is thus required a model other than (1) to account for the anisotropic behavior of these solids. A transversely isotropic model has been proposed in [Destrade et al. 2010a], in which the strain-energy density of third order (actually, it is the most general third order expansion) is given by

$$W = \mu I_2 + \frac{1}{3}A I_3 + \alpha_1 I_4^2 + \alpha_2 I_5 + \alpha_3 I_2 I_4 + \alpha_4 I_4^3 + \alpha_5 I_4 I_5, \quad (3)$$

where I_2 and I_3 are given in (2) and

$$I_4 = \mathbf{M} \cdot (\mathbf{E}\mathbf{M}), \quad I_5 = \mathbf{M} \cdot (\mathbf{E}^2\mathbf{M}), \quad (4)$$

are anisotropic invariants where \mathbf{M} is the unit vector that gives the undeformed fiber direction. It follows that μ, α_1, α_2 and $A, \alpha_3, \alpha_4, \alpha_5$ are second- and third-order elastic constants, respectively. To evaluate the elastic constants μ, A, α_k ($k = \overline{1, 5}$, where the overline means $k = 1, \dots, 5$) the authors established a formula for the velocity of shear bulk waves. This formula is a first-order polynomial in the elongation e , defined by $\lambda = 1 + e$, where λ is the principal stretch in the direction of the fibers and the uniaxial tension. The speeds of infinitesimal waves expressed in terms of third- and fourth-order constants does provide a basis for the acousto-elastic evaluation of the material constants [Destrade and Ogden 2010].

To make the model more accurate and representative of soft biological tissue we consider a fourth-order strain-energy function (actually, the most general fourth order expansion), namely (see also [Destrade et al. 2010a])

$$W = \mu I_2 + \frac{1}{3}A I_3 + \alpha_1 I_4^2 + \alpha_2 I_5 + \alpha_3 I_2 I_4 + \alpha_4 I_4^3 + \alpha_5 I_4 I_5 + \alpha_6 I_2^2 + \alpha_7 I_2 I_4^2 + \alpha_8 I_2 I_5 + \alpha_9 I_4^4 + \alpha_{10} I_5^2 + \alpha_{11} I_3 I_4, \quad (5)$$

where $\alpha_6, \dots, \alpha_{11}$ are fourth-order elastic constants. In order to determine the elastic constants μ, A , and α_k ($k = \overline{1, 11}$), we develop formulas for the velocity of (homogeneous plane) shear bulk waves and surface Rayleigh waves which are second-order polynomials of the elongation e . When $\alpha_k = 0$, $k = \overline{1, 11}$, $k \neq 6$ and α_6 is denoted D , these formulas coincide with the corresponding approximate formulas obtained in [Destrade et al. 2010b]. The results show that linear corrections to the acoustoelastic wave speed formulas involve second- and third-order constants, and that quadratic corrections involve second-, third-, and fourth-order constants, in agreement with [Hoger 1999].

The layout of the paper is as follows. In Section 2, we introduce briefly the main governing equations while Sections 3 and 4 are devoted to the acousto-elastic analysis of (5). In Section 5 some conclusions are outlined.

2. Expressions of components of the fourth-order elasticity tensor

We consider an incompressible transversely isotropic elastic body \mathcal{B} , which possesses a natural unstrained state \mathcal{B}_0 and a finitely deformed (pre-stressed) equilibrium state \mathcal{B}_e . A small time-dependent motion is superimposed upon this pre-stressed equilibrium configuration to reach a final material state \mathcal{B}_t , called

current configuration. The position vectors of a representative particle are denoted by X_A , $x_i(\mathbf{X})$, $\tilde{x}_i(\mathbf{X}, t)$ in \mathcal{B}_0 , \mathcal{B}_e and \mathcal{B}_t , respectively. The deformation gradient tensor associated with the deformations $\mathcal{B}_0 \rightarrow \mathcal{B}_t$ and $\mathcal{B}_0 \rightarrow \mathcal{B}_e$ are denoted by \mathbf{F} and $\bar{\mathbf{F}}$ and given in component form by

$$F_{iA} = \frac{\partial \tilde{x}_i}{\partial X_A}, \quad \bar{F}_{iA} = \frac{\partial x_i}{\partial X_A}. \quad (6)$$

It is clear from (6) that

$$F_{iA} = (\delta_{ij} + u_{i,j}) \bar{F}_{jA}, \quad (7)$$

where δ_{ij} is the Kronecker operator, $u_i(\mathbf{X}, t)$ denotes the small time-dependent displacement associated with the deformation $\mathcal{B}_e \rightarrow \mathcal{B}_t$ and a comma indicates differentiation with respect to the indicated spatial coordinate in \mathcal{B}_e .

Suppose that the body is a soft tissue with one preferred direction associated with a family of parallel fibers of collagen. We denote by \mathbf{M} the unit vector in that direction when the solid is unloaded and at rest. Then, the strain-energy function W of the body, per unit volume at \mathcal{B}_0 , may be expressed by (5) (see [Destrade et al. 2010a]). It is well-known that $\mathbf{E} = (\mathbf{C} - \mathbf{I})/2$, where $\mathbf{C} = \mathbf{F}^T \mathbf{F}$ is the right Cauchy–Green strain tensor and \mathbf{I} is the identity tensor. In the absence of body forces, the equations of motion may be expressed in the following form (see [Prikazchikov and Rogerson 2003]):

$$\frac{\partial S_{Ai}}{\partial X_A} = \rho \ddot{u}_i \quad \text{or} \quad \frac{\partial}{\partial x_m} (\bar{F}_{mA} S_{Ai}) = \rho \ddot{u}_i, \quad S_{Ai} = \frac{\partial W^*}{\partial F_{iA}}, \quad W^* = W - p(J - 1), \quad J = \det \mathbf{F}, \quad (8)$$

where a superposed dot indicates differentiation with respect to the time t , $\bar{\mathbf{F}}$ is a constant tensor, S_{Ai} are the components of the nominal stress tensor and p plays the role of a Lagrange multiplier and may be understood as a pressure (in \mathcal{B}_t) associated with the incompressibility constraint. Since the quantities associated with the deformation $\mathcal{B}_e \rightarrow \mathcal{B}_t$ are small in comparison with the corresponding quantities associated with the deformations $\mathcal{B}_0 \rightarrow \mathcal{B}_e$ we have

$$S_{Ai} \approx S_{Ai}(\bar{\mathbf{F}}, \bar{p}) + \frac{\partial S_{Ai}}{\partial F_{kB}}(\bar{\mathbf{F}}, \bar{p}) u_{k,m} \bar{F}_{mB} + p^* \frac{\partial S_{Ai}}{\partial p}(\bar{\mathbf{F}}, \bar{p}), \quad (9)$$

where $\bar{p} = p(\bar{\mathbf{F}})$ and $p^* = p - \bar{p}$ is the time-dependent pressure increment. On use of the linear approximation (9) into (8)₂, the linearized equations of motion are obtained and can be written as

$$A_{jilk} u_{k,lj} - p_{,i}^* = \rho \ddot{u}_i, \quad (10)$$

where

$$A_{ijkl} = \bar{F}_{iA} \bar{F}_{kB} \left. \frac{\partial^2 W}{\partial F_{jA} \partial F_{lB}} \right|_{\mathbf{F}=\bar{\mathbf{F}}}, \quad (11)$$

are the components of the so-called fourth-order elasticity tensor. It is not difficult to verify that

$$A_{piqj} = \bar{F}_{p\alpha} \bar{F}_{q\beta} \left[\frac{1}{2} \delta_{ij} \left(\frac{\partial W}{\partial E_{\alpha\beta}} + \frac{\partial W}{\partial E_{\beta\alpha}} \right) + \frac{1}{4} \left(\bar{F}_{in} \bar{F}_{jy} \frac{\partial^2 W}{\partial E_{\alpha n} \partial E_{\beta y}} + \bar{F}_{in} \bar{F}_{jx} \frac{\partial^2 W}{\partial E_{\alpha n} \partial E_{x\beta}} + \bar{F}_{im} \bar{F}_{jy} \frac{\partial^2 W}{\partial E_{m\alpha} \partial E_{\beta y}} + \bar{F}_{im} \bar{F}_{jx} \frac{\partial^2 W}{\partial E_{m\alpha} \partial E_{x\beta}} \right) \right] \Big|_{\mathbf{F}=\bar{\mathbf{F}}}, \quad (12)$$

where

$$\frac{\partial W}{\partial E_{mn}} = \sum_{k=2}^5 \frac{\partial W}{\partial I_k} \frac{\partial I_k}{\partial E_{mn}}, \quad (13)$$

$$\frac{\partial^2 W}{\partial E_{mn} \partial E_{xy}} = \sum_{k=2}^5 \frac{\partial W}{\partial I_k} \frac{\partial^2 I_k}{\partial E_{mn} \partial E_{xy}} + \sum_{k=2}^5 \sum_{l=2}^5 \frac{\partial^2 W}{\partial I_k \partial I_l} \frac{\partial I_k}{\partial E_{mn}} \frac{\partial I_l}{\partial E_{xy}}, \quad (14)$$

and

$$\begin{aligned} \frac{\partial I_2}{\partial E_{mn}} &= 2E_{nm}, & \frac{\partial^2 I_2}{\partial E_{mn} \partial E_{xy}} &= 2\delta_{nx}\delta_{my}, \\ \frac{\partial I_3}{\partial E_{mn}} &= 3E_{nk}E_{km}, & \frac{\partial^2 I_3}{\partial E_{mn} \partial E_{xy}} &= 3(\delta_{nx}\delta_{ky}E_{km} + \delta_{kx}\delta_{my}E_{nk}), \\ \frac{\partial I_4}{\partial E_{mn}} &= M_m M_n, & \frac{\partial^2 I_4}{\partial E_{mn} \partial E_{xy}} &= 0, \\ \frac{\partial I_5}{\partial E_{mn}} &= M_m E_{nj} M_j + M_i E_{im} M_n, & \frac{\partial^2 I_5}{\partial E_{mn} \partial E_{xy}} &= M_m M_y \delta_{nx} + M_x M_n \delta_{my}. \end{aligned} \quad (15)$$

It is clear from (12) that $A_{ijkl} = A_{klij}$. The incremental condition of incompressibility follows and is of the form

$$u_{i,i} = 0. \quad (16)$$

3. Formulas for the velocity of shear bulk waves

We now describe the special loading and geometry case that will be used in the sections that follow. Consider a rectangular block of a soft transversely isotropic incompressible elastic solid whose faces in the unstressed state \mathcal{B}_0 are parallel to the (X_1, X_2) -, (X_2, X_3) -, (X_3, X_1) -planes and with the fiber direction \mathbf{M} parallel to the X_1 -direction (i. e. the fibers are parallel to OX_1). Suppose that the sample is under uniaxial tension or compression with the direction of tension parallel to the X_1 -axis. It is easy to see that the sample is subject to a equi-biaxial deformation, namely

$$x_1 = \lambda_1 X_1, \quad x_2 = \lambda_2 X_2, \quad x_3 = \lambda_3 X_3, \quad (17)$$

in which

$$\lambda_1 = \lambda, \quad \lambda_2 = \lambda_3 = \lambda^{-1/2}, \quad \lambda > 0, \quad (18)$$

where λ_k are the principal stretches of deformation. Note that the faces of the deformed block are parallel to the (x_1, x_2) -, (x_2, x_3) -, (x_3, x_1) -planes. In the case under consideration we have

$$\mathbf{F} = \begin{pmatrix} \lambda_1 & 0 & 0 \\ 0 & \lambda_2 & 0 \\ 0 & 0 & \lambda_3 \end{pmatrix}, \quad \mathbf{E} = \frac{1}{2} \begin{pmatrix} \lambda_1^2 - 1 & 0 & 0 \\ 0 & \lambda_2^2 - 1 & 0 \\ 0 & 0 & \lambda_3^2 - 1 \end{pmatrix}, \quad (19)$$

and

$$I_2 = E_{11}^2 + E_{22}^2 + E_{33}^2, \quad I_3 = E_{11}^3 + E_{22}^3 + E_{33}^3, \quad I_4 = E_{11}, \quad I_5 = E_{11}^2, \quad (20)$$

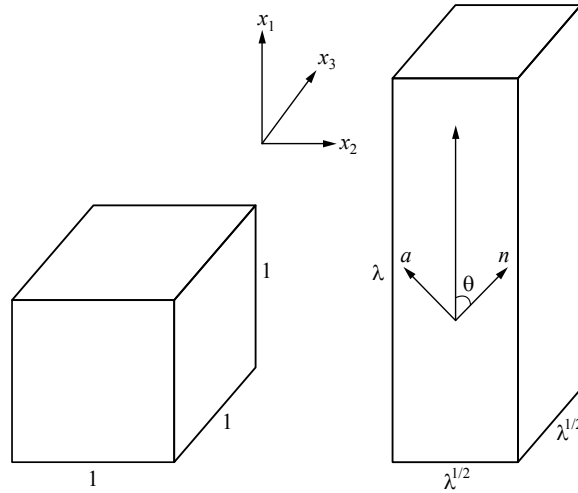


Figure 1. Geometry of cases addressed in Sections 3 and 4. The rectangular block on the left gives the undeformed configuration while the one on the right gives the deformed configuration under the conditions at hand indicating the principal stretches of deformation. Waves travel in the (x_1, x_2) -plane. In that plane, we denote \mathbf{n} as the unit vector in the direction of propagation and we denote \mathbf{a} as the unit vector orthogonal to \mathbf{n} .

where $E_{kk} = (\lambda_k^2 - 1)/2$. With the focus on (5) we apply the equation of motion and the incompressibility condition to the analysis of homogeneous plane waves.

Remark 1. Using (12)–(15) together with (19) and (20) it is easy to find that there are only 15 nonzero components of the fourth-order elasticity tensor, namely A_{ijij} , A_{ijji} ($i, j = 1, 2, 3, i \neq j$) and A_{ijji} ($i, j = 1, 2, 3, i \neq j$).

Consider waves traveling in the (x_1, x_2) -plane. In that plane denote \mathbf{n} as the unit vector in the direction of propagation and \mathbf{a} as the unit vector orthogonal to \mathbf{n} (see Figure 1). From [Ogden 2007], for example, it is known that there exist two shear bulk waves, one of which is polarized along \mathbf{a} and travels with velocity v_{1a} , and the other is polarized along $\mathbf{b} = \mathbf{a} \times \mathbf{n}$ and travels with velocity v_{1b} . These velocities are determined by (see also [Destrade et al. 2010b])

$$\rho v_{1a}^2 = (\gamma_{12} + \gamma_{21} - 2\beta_{12})c_\theta^4 + 2(\beta_{12} - \gamma_{21})c_\theta^2 + \gamma_{21}, \quad \rho v_{1b}^2 = \gamma_{13}c_\theta^2 + \gamma_{23}s_\theta^2, \quad (21)$$

where θ is the angle between \mathbf{n} , the direction of propagation, and the x_1 -direction, $c_\theta^n := \cos^n \theta$, $s_\theta^n := \sin^n \theta$, and γ_{ij} and β_{ij} ($i, j = 1, 2, 3, i \neq j$) are given by

$$\gamma_{ij} = A_{ijij}, \quad 2\beta_{ij} = A_{iiii} + A_{jjjj} - 2(A_{iijj} + A_{ijji}), \quad (22)$$

with no sum on repeated indices in formulas (22). Note that while $\beta_{ij} = \beta_{ji}$ (due to $A_{ijkl} = A_{klij}$), it is easy to see that $\gamma_{ij} \neq \gamma_{ji}$ in general. The velocities in (21) are written as polynomials in terms of c_θ^n and s_θ^n .

Now, consider a sufficiently small elongation e defined by $\lambda_1 = 1 + e$. Expanding γ_{ij} and β_{ij} into Maclaurin series up to second order in e by means of (22) and using (12)–(15), under the (uniaxial)

conditions at hand, we obtain for the coefficients of the polynomial in (21)₁, after a long computation,

$$2\beta_{12} - \gamma_{12} - \gamma_{21} = 2\alpha_1 + 2(4\alpha_1 + 3\alpha_2 + 3\alpha_3 + 3\alpha_4 + 2\alpha_5)e \\ + 3(6\mu + 3A + 4\alpha_1 + 4\alpha_2 + 6\alpha_3 + 9\alpha_4 + 8\alpha_5 + 6\alpha_6 + 5\alpha_7 + 4\alpha_8 + 4\alpha_9 + \frac{8}{3}\alpha_{10} + \frac{3}{2}\alpha_{11})e^2, \quad (23)$$

$$2(\beta_{12} - \gamma_{21}) = 2\alpha_1 + (3\mu + 10\alpha_1 + 8\alpha_2 + 6\alpha_3 + 6\alpha_4 + 4\alpha_5)e \\ + (21\mu + \frac{39}{4}A + 17\alpha_1 + 17\alpha_2 + \frac{45}{2}\alpha_3 + 30\alpha_4 + 27\alpha_5 + 18\alpha_6 + 15\alpha_7 + 12\alpha_8 + 12\alpha_9 + 8\alpha_{10} + \frac{9}{2}\alpha_{11})e^2, \quad (24)$$

$$4\gamma_{21} = 4\mu + 2\alpha_2 + (A + 2\alpha_2 + 4\alpha_3 + 2\alpha_5)e + (8\mu + 4A + 2\alpha_3 + 3\alpha_5 + 12\alpha_6 + 4\alpha_7 + 7\alpha_8 + 4\alpha_{10} + 3\alpha_{11})e^2. \quad (25)$$

Note that by taking $\alpha_k = 0$, $k = \overline{6, 11}$, in the expressions (23)–(25) we obtain the expansions given in [Destrade et al. 2010a, (19)].

Introducing (23)–(25) into (21)₁ yields

$$\rho v_{1a}^2 = \frac{1}{2}\alpha_1 s_{2\theta}^2 + \mu + \frac{1}{2}\alpha_2 + [3\mu c_\theta^2 + \frac{1}{4}A + (10c_\theta^2 - 8c_\theta^4)\alpha_1 + (8c_\theta^2 - 6c_\theta^4 + \frac{1}{2})\alpha_2 \\ + (\frac{3}{2}s_{2\theta}^2 + 1)\alpha_3 + \frac{3}{2}s_{2\theta}^2\alpha_4 + (s_{2\theta}^2 + \frac{1}{2})\alpha_5]e + [(21c_\theta^2 - 18c_\theta^4 + 2)\mu \\ + (\frac{39}{4}c_\theta^2 - 9c_\theta^4 + 1)A + (17c_\theta^2 - 12c_\theta^4)(\alpha_1 + \alpha_2) + (\frac{45}{2}c_\theta^2 - 18c_\theta^4 + \frac{1}{2})\alpha_3 \\ + (30c_\theta^2 - 27c_\theta^4)\alpha_4 + (27c_\theta^2 - 24c_\theta^4 + \frac{3}{4})\alpha_5 + (\frac{9}{2}s_{2\theta}^2 + 1)\alpha_6 + (\frac{15}{4}s_{2\theta}^2 + 1)\alpha_7 \\ + (3s_{2\theta}^2 + \frac{7}{4})\alpha_8 + 3s_{2\theta}^2\alpha_9 + (2s_{2\theta}^2 + 1)\alpha_{10} + (\frac{9}{8}s_{2\theta}^2 + \frac{3}{4})\alpha_{11}]e^2. \quad (26)$$

In a parallel way, we use (12)–(15) to calculate γ_{13} ($= \gamma_{12}$) and γ_{23} , which are the polynomial-term coefficients in (21)₂. Their approximations up second order in e are derived expanding them into Maclaurin series and disregarding all terms equal to and higher than e^3 in the expansions. The values are

$$\gamma_{13} = \mu + \frac{1}{2}\alpha_2 + (3\mu + \frac{1}{4}A + 2\alpha_1 + \frac{5}{2}\alpha_2 + \alpha_3 + \frac{1}{2}\alpha_5)e \\ + (5\mu + \frac{7}{4}A + 5\alpha_1 + 5\alpha_2 + 5\alpha_3 + 3\alpha_4 + \frac{15}{4}\alpha_5 + 3\alpha_6 + \alpha_7 + \frac{7}{4}\alpha_8 + \alpha_{10} + \frac{3}{4}\alpha_{11})e^2, \quad (27) \\ \gamma_{23} = \mu + (-3\mu - \frac{1}{2}A + \alpha_3)e + (5\mu + \frac{7}{4}A - \frac{5}{2}\alpha_3 + 3\alpha_6 + \alpha_7 + \alpha_8 - \frac{3}{2}\alpha_{11})e^2.$$

Introducing (27) into (21)₂ one gets the approximation of ρv_{1b}^2 in terms of e , which is

$$\rho v_{1b}^2 = \mu + \frac{1}{2}c_\theta^2\alpha_2 + [3(\mu + \frac{1}{8}A)c_{2\theta} - \frac{1}{8}A + 2c_\theta^2\alpha_1 + \frac{5}{2}c_\theta^2\alpha_2 + \alpha_3 + \frac{1}{2}\alpha_5]e \\ + [5\mu + \frac{7}{4}A + 5c_\theta^2\alpha_1 + 5c_\theta^2\alpha_2 + \frac{5}{2}(2c_\theta^2 - s_\theta^2)\alpha_3 + 3c_\theta^2\alpha_4 + \frac{15}{4}c_\theta^2\alpha_5 \\ + 3\alpha_6 + \alpha_7 + \frac{7}{4}(c_\theta^2 + 4s_\theta^2)\alpha_8 + c_\theta^2\alpha_{10} + \frac{3}{4}(c_\theta^2 - 2s_\theta^2)\alpha_{11}]e^2. \quad (28)$$

As noticed before, if $\alpha_k = 0$, $k = \overline{1, 11}$, $k \neq 6$ and α_6 is denoted D one gets the expressions in [Destrade et al. 2010b, (11)]. Note that when $\theta = 0$ the two shear velocities coincide and can be written as

$$\rho v_{1a}^2 = \rho v_{1b}^2 = \mu + \frac{1}{2}\alpha_2 + (3\mu + \frac{1}{4}A + 2\alpha_1 + \frac{5}{2}\alpha_2 + \alpha_3 + \frac{1}{2}\alpha_5)e \\ + (5\mu + \frac{7}{4}A + 5\alpha_1 + 5\alpha_2 + 5\alpha_3 + 3\alpha_4 + \frac{15}{4}\alpha_5 + 3\alpha_6 + \alpha_7 + \frac{7}{4}\alpha_8 + \alpha_{10} + \frac{3}{4}\alpha_{11})e^2. \quad (29)$$

The result in [Destrade et al. 2010b, (12)] is a special case of the approximation (29) when $\alpha_k = 0$, $k = \overline{1, 11}$, $k \neq 6$.

Let us turn our attention to consider shear waves that travel in the (x_2, x_3) -plane. Now, by θ we denote the angle between the direction of propagation of the plane wave and the x_2 -axis. Then, it is clear that

$\mathbf{n} = [0, \cos \theta, \sin \theta]^T$, $\mathbf{a} = [0, \sin \theta, -\cos \theta]^T$. The speed v_{2a} of the shear bulk wave polarized along \mathbf{a} is given by (21)₁ with the indices 12 and 21 replaced by 23 and 32, respectively. In this case, it follows easily using (12)–(15) that $\gamma_{23} = \gamma_{32} = \beta_{23}$. This makes the dependence of the shear wave on θ to vanish and one finally writes the speed v_{2a} in terms of e as

$$\rho v_{2a}^2 = \gamma_{32} = \mu + \left(-3\mu - \frac{1}{2}A + \alpha_3\right)e + \left(5\mu + \frac{7}{4}A - \frac{5}{2}\alpha_3 + 3\alpha_6 + \alpha_7 + \alpha_8 - \frac{3}{2}\alpha_{11}\right)e^2. \quad (30)$$

The approximation [Destrade et al. 2010b, (13)] is obtained from (30) by making $\alpha_k = 0$ for $k = \overline{1, 11}$, $k \neq 6$, and replacing α_6 by D .

Lastly, consider waves that travel in the (x_1, x_3) -plane. In this case, θ is the angle between the direction of propagation of the plane wave and the x_1 -axis. Using (12)–(15), it follows that $\gamma_{12} = \gamma_{13}$, $\gamma_{21} = \gamma_{31}$ and $\beta_{12} = \beta_{13}$. From these facts it is obvious that the secular equations in this case are exactly the ones obtained for waves propagating in the (x_1, x_2) -plane. This is consistent with the transversely isotropic character of the strain-induced anisotropy.

4. Formulas for the velocity of Rayleigh waves

We turn our attention to the analysis of Rayleigh surface waves. In what follows, by RW km ($k, m = 1, 2, 3, k \neq m$) we denote, for simplicity, a Rayleigh wave propagating along the x_k -direction, and attenuating in the x_m -direction, i.e., we consider a half space occupying the region $x_m < 0$ in the reference configuration with boundary $x_m = 0$ and surfaces waves propagating in the direction x_k .

4A. Secular equations.

Remark 2. According to Remark 1, the equations of motion (10) for the incremental displacements u_i , the incremental equation (16) of incompressibility, and the expressions of the incremental traction components are for Rayleigh surface waves the same as those for pre-stressed incompressible isotropic elastic materials (see [Vinh 2010] and references therein). Moreover, using (12)–(15), (19) and (20) one can see that the relations

$$A_{ijji} = A_{jii j} = A_{ijij} - \lambda_i \frac{\partial W}{\partial \lambda_i}, \quad (31)$$

still hold for the (uniaxial) cases under consideration. Therefore, the secular equations of Rayleigh waves for transversely isotropic materials under the conditions considered here are the same as the ones obtained for pre-stressed incompressible isotropic elastic materials.

Let us consider first the RW12 that travels with velocity v . Following Remark 2 and according to [Dowaikh and Ogden 1990], the secular equation of the Rayleigh wave RW12 is (see also [Vinh 2010; Prikazchikov and Rogerson 2004; Vinh and Giang 2010])

$$\gamma_{21}(\gamma_{12} - \rho v^2) + (2\beta_{12} + 2\gamma_{21}^* - \rho v^2)[\gamma_{21}(\gamma_{12} - \rho v^2)]^{1/2} = (\gamma_{21}^*)^2, \quad 0 < \rho v^2 < \gamma_{12}, \quad (32)$$

where γ_{12} , γ_{21} , and β_{12} are defined by (22), $\gamma_{mk}^* = \gamma_{mk} - \sigma_m$ ($m, k = 1, 2, 3, m \neq k$) and the σ_i are the principal stresses of the Cauchy stress tensor, which are given by [Ogden 1984]

$$\sigma_i = \lambda_i \frac{\partial W}{\partial \lambda_i} - \bar{p} \quad (i = 1, 2, 3). \quad (33)$$

Similarly, the secular equation of RW km can be written as

$$\gamma_{mk}(\gamma_{km} - \rho v^2) + (2\beta_{km} + 2\gamma_{mk}^* - \rho v^2)[\gamma_{mk}(\gamma_{km} - \rho v^2)]^{1/2} = (\gamma_{mk}^*)^2, \quad 0 < \rho v^2 < \gamma_{km}, \quad (34)$$

where γ_{mk} and β_{mk} are given by (22). Under the conditions at hand, it follows that $\sigma_2 = \sigma_3 = 0$, and, furthermore, $\gamma_{2k}^* = \gamma_{2k}$ ($k = 1, 3$), $\gamma_{3k}^* = \gamma_{3k}$ ($k = 1, 2$). The strong-ellipticity condition (see [Ogden and Singh 2011], for instance) requires that $\gamma_{km} > 0$ ($k, m = 1, 2, 3, k \neq m$). The following results show that it seems natural to consider expansions of strain energy functions in terms of the invariants of \mathbf{E} . Formulas for the Rayleigh surface waves obtained as polynomials of e depend only on some of the terms in which the strain-energy function W maybe expanded. More precisely, it is shown that linear polynomials of e depend on the coefficients included up to the third-order terms of the strain-energy function W . On the other hand, second-order polynomials in e depend also on the coefficients included up to the fourth-order terms of the strain-energy function W . We focus first on the first-order approximation for the velocity to clarify the analysis.

4B. First-order approximations for the velocity. In this section we obtain formulas for the velocity of the RW km given as first-order polynomials in e , i.e., we obtain

$$\rho v_{km}^2 = a_{km} + b_{km}e, \quad (35)$$

where v_{km} is the velocity of RW km . It follows that these equations include μ , A , a_k , $k = \overline{1, 5}$ and can be used to determine the elastic coefficients associated with the third-order strain-energy function (3).

Expression of v_{12} associated with RW12. It is readily verified that (32)₁ in terms of $\eta = \sqrt{(\gamma_{12} - \rho v^2)/\gamma_{21}}$ is of the form (see also [Destrade et al. 2010b; Dowaiikh and Ogden 1990])

$$\eta^3 + \eta^2 + g(e)\eta - 1 = 0, \quad (36)$$

where $g(e) := (2\beta_{12} + 2\gamma_{21} - \gamma_{12})/\gamma_{21}$. For our purposes it is sufficient to expand $g(e)$ up to first order in e . It is not difficult to obtain that $g(e) = g_0 + g_1e + O(e^2)$ where

$$\begin{aligned} g_0 &= \frac{6\mu + 4\alpha_1 + \alpha_2}{2\mu + \alpha_2}, \\ g_1 &= \frac{3A/2 + 16\alpha_1 + 15\alpha_2 + 18\alpha_3 + 12\alpha_4 + 11\alpha_5}{2\mu + \alpha_2} - \frac{(6\mu + 4\alpha_1 + 3\alpha_2)(A/2 + \alpha_2 + 2\alpha_3 + \alpha_5)}{(2\mu + \alpha_2)^2}. \end{aligned} \quad (37)$$

Equation (36) can be rewritten as

$$F[\eta, e] \equiv \eta^3 + \eta^2 + g(e)\eta - 1 = 0. \quad (38)$$

To obtain the the first-order approximation in e of ρv^2 it is sufficient to expand η as

$$\eta = \eta_0 + \eta_1 e, \quad \eta_0 := \eta(0), \quad \eta_1 = \eta'(0), \quad (39)$$

where η_0 is a solution of the equation

$$\eta^3 + \eta^2 + g_0\eta - 1 = 0. \quad (40)$$

The value η_0 corresponds to the Rayleigh wave propagating in the incompressible transversely isotropic elastic solids (without pre-stresses) and, according to [Ogden and Vinh 2004], η_0 is given by

$$\frac{1}{3} \left[-1 + \sqrt[3]{\frac{1}{2} [9\Delta + 16 + 3\sqrt{3}\sqrt{\Delta(4\Delta^2 - 13\Delta + 32)}]} - \sqrt[3]{\frac{1}{2} [9\Delta + 16 - 3\sqrt{3}\sqrt{\Delta(4\Delta^2 - 13\Delta + 32)}]} \right], \quad (41)$$

where $\Delta = g_0 + 1 = (8\mu + 4\alpha_1 + 2\alpha_2)/(2\mu + \alpha_2)$. Note that η_0 depends only on the second-order elastic constants μ, α_1, α_2 and $\eta_0 = 0.2956$ when $\alpha_1 = \alpha_2 = 0$ (for which $g_0 = 3, \Delta = 4$).

Since $\phi(e) = F[\eta(e), e] \equiv 0$, it is easy to get that $\phi'(e) = 0, \phi''(e) = 0$ as well as the remaining derivatives. Using (38) and $\phi'(e) = 0$ it follows that

$$\eta'(e) = -\frac{\partial F(\eta(e), e)/\partial e}{\partial F(\eta(e), e)/\partial \eta} = -\frac{g'(e)\eta}{3\eta^2 + 2\eta + g(e)}, \quad (42)$$

and therefore

$$\eta_1 = \eta'(0) = -\frac{\partial F(\eta_0, 0)/\partial e}{\partial F(\eta_0, 0)/\partial \eta} = -\frac{g_1\eta_0}{3\eta_0^2 + 2\eta_0 + g_0}. \quad (43)$$

Now, introducing γ_{12} and γ_{21} , which are given by (22), into the relation $\rho v^2 = \gamma_{12} - \gamma_{21}(\eta_0 + \eta_1 e)^2$ and expanding the resulting expression up to first order in e , we obtained

$$\rho v_{12}^2 = s_0 + s_1 e, \quad (44)$$

where

$$\begin{aligned} s_0 &= (1 - \eta_0^2)(\mu + \frac{1}{2}\alpha_2), \\ s_1 &= (3 - 2\eta_0\eta_1)\mu + \frac{1}{4}(1 - \eta_0^2)A + 2\alpha_1 + \frac{1}{2}(5 - 2\eta_0\eta_1 - \eta_0^2)\alpha_2 + (1 - \eta_0^2)(\alpha_3 + \alpha_5). \end{aligned} \quad (45)$$

The values η_0 and η_1 are obtained using (41) and (43), respectively, by means of (37). It is clear that ρv_{12}^2 is a function of μ, A, a_k ($k = \overline{1, 5}$) and e .

Expression of v_{23} associated with RW23. According to (34) and noting that $\sigma_3 = 0$, the secular equation of the RW23 ($k = 2, m = 3$) takes the form

$$\gamma_{32}(\gamma_{23} - \rho v^2) + (2\beta_{23} + 2\gamma_{32} - \rho v^2)[\gamma_{32}(\gamma_{23} - \rho v^2)]^{1/2} = (\gamma_{32})^2, \quad 0 < \rho v^2 < \gamma_{21}. \quad (46)$$

In terms of the variable $\eta = \sqrt{(\gamma_{23} - \rho v^2)/\gamma_{32}}$, (46) can be rewritten as

$$\eta^3 + \eta^2 + g^{(23)}(e)\eta - 1 = 0, \quad (47)$$

where $g^{(23)}(e) = (2\beta_{23} + 2\gamma_{32} - \gamma_{23})/\gamma_{32}$. Since $\gamma_{23} = \gamma_{32} = \beta_{23}$, as mentioned just before Equation (30), it follows that $g^{(23)}(e) = 3$ and, therefore, that $\eta = \eta_0$ where η_0 is given by (41). Taking into account (27)₂, the first-order approximation of $\rho v_{23}^2 = \gamma_{23}(1 - \eta_0^2)$ is finally

$$\rho v_{23}^2 = (1 - \eta_0^2)[\mu + (-3\mu - A/2)e + \alpha_3]. \quad (48)$$

Expression of v_{21} associated with RW21. According to (34) the secular equation of the RW21 is

$$\gamma_{12}(\gamma_{21} - \rho v^2) + (2\beta_{21} + 2\gamma_{12}^* - \rho v^2)[\gamma_{12}(\gamma_{21} - \rho v^2)]^{1/2} = (\gamma_{12}^*)^2, \quad 0 < \rho v^2 < \gamma_{21}. \quad (49)$$

Using (12)–(15) one can see that $\lambda_1 \partial W / \partial \lambda_1 - \lambda_2 \partial W / \partial \lambda_2 = \gamma_{12} - \gamma_{21}$. From this fact and the relation $\sigma_1 - \sigma_2 = \lambda_1 \partial W / \partial \lambda_1 - \lambda_2 \partial W / \partial \lambda_2$ (obtained from (33)) and $\sigma_2 = 0$ it follows that $\sigma_1 = \gamma_{12} - \gamma_{21}$. Thus $\gamma_{12}^* = \gamma_{21}$, and (49) now becomes

$$\gamma_{12}(\gamma_{21} - \rho v^2) + (2\beta_{21} + 2\gamma_{21} - \rho v^2)[\gamma_{12}(\gamma_{21} - \rho v^2)]^{1/2} = (\gamma_{21})^2, \quad 0 < \rho v^2 < \gamma_{21}. \quad (50)$$

In terms of the variable $\eta = \sqrt{(\gamma_{21} - \rho v^2) / \gamma_{12}}$, Equation (50) can be written as

$$\eta^3 + \eta^2 + g^{(21)}(e)\eta - h(e) = 0, \quad (51)$$

where $g^{(21)}(e) := (2\beta_{21} + \gamma_{21}) / \gamma_{12}$, $h(e) := \gamma_{21}^2 / \gamma_{12}^2$. Up to first order, the expansions of $g^{(21)}(e)$ and $h(e)$ are $g^{(21)}(e) = g_0^{(21)} + g_1^{(21)}e + O(e^2)$ and $h(e) = 1 - h_1e + O(e^2)$, where

$$\begin{aligned} g_0^{(21)} &= \frac{6\mu + 4\alpha_1 + 3\alpha_2}{2\mu + \alpha_2}, \\ g_1^{(21)} &= \frac{6\mu + \frac{3}{2}A + 20\alpha_1 + 19\alpha_2 + 18\alpha_3 + 12\alpha_4 + 11\alpha_5}{2\mu + \alpha_2} - \frac{6\mu + 4\alpha_1 + 3\alpha_2}{(2\mu + \alpha_2)^2} (6\mu + \frac{1}{2}A + 4\alpha_1 + 5\alpha_2 + 2\alpha_3 + \alpha_5), \\ h_1 &= \frac{4(3\mu + 2\alpha_1 + 2\alpha_2)}{2\mu + \alpha_2}. \end{aligned} \quad (52)$$

Following the same procedure used to get the first-order approximation of ρv_{12}^2 , now, we have

$$\rho v_{21}^2 = s_0^{(21)} + s_1^{(21)}e, \quad (53)$$

where

$$\begin{aligned} s_0^{(21)} &= (1 - \eta_0^2)(\mu + \frac{1}{2}\alpha_2), \\ s_1^{(21)} &= -(2\eta_0\eta_1 + 3\eta_0^2)\mu + \frac{1}{4}(1 - \eta_0^2)A - 2\eta_0^2\alpha_1 + \frac{1}{2}(1 - 2\eta_0\eta_1 - 5\eta_0^2)\alpha_2 + \frac{1}{2}(1 - \eta_0^2)(2\alpha_3 + \alpha_5), \end{aligned} \quad (54)$$

in which η_0 is calculated by (41) and

$$\eta_1 = -\frac{g_1^{(21)}\eta_0 + h_1}{3\eta_0^2 + 2\eta_0 + g_0^{(21)}}. \quad (55)$$

4C. Second-order approximations for the velocity. We now extend the above analysis to include fourth-order terms in the strain-energy function. For that reason, it is necessary to obtain formulas for the velocity of the RWkm given as second-order polynomials in e . We follow closely the notation used in the different cases analyzed in Section 4B.

Expression of v_{12} associated with RW12. In order to create second-order approximations for the velocity of RW12 we need to expand $g(e)$ into a Maclaurin series up to second order in e . One can write

$$g(e) = g_0 + g_1e + g_2e^2 + O(e^3),$$

where g_0, g_1 are given by (37) and

$$\begin{aligned}
 g_2 = & \frac{2}{2\mu + \alpha_2} (24\mu + 12A + 12\alpha_1 + 12\alpha_2 + \frac{39}{2}\alpha_3 + 27\alpha_4 + \frac{105}{4}\alpha_5 + 27\alpha_6 + 18\alpha_7 + \frac{69}{4}\alpha_8 + 12\alpha_9 + 11\alpha_{10} + \frac{27}{4}\alpha_{11}) \\
 & - \frac{2(6\mu + 4\alpha_1 + 3\alpha_2)}{(2\mu + \alpha_2)^2} (2\mu + A + \frac{1}{2}\alpha_3 + \frac{3}{4}\alpha_5 + 3\alpha_6 + \alpha_7 + \frac{7}{4}\alpha_8 + \alpha_{10} + \frac{3}{4}\alpha_{11}) \\
 & - \frac{A + 2\alpha_2 + 4\alpha_3 + 2\alpha_5}{(2\mu + \alpha_3)^3} (12\mu\alpha_3 + 6\alpha_2\alpha_3 + 8\mu\alpha_5 + 4\alpha_2\alpha_5 + 12\mu\alpha_2 + 6\alpha_2^2 \\
 & \quad + 12\mu\alpha_4 + 6\alpha_2\alpha_4 + 16\mu\alpha_1 + 6\alpha_1\alpha_2 - 4\alpha_1\alpha_3 - A\alpha_1 - 2\alpha_1\alpha_5). \quad (56)
 \end{aligned}$$

Up to second order in e the expansion of $\eta(e)$ is $\eta = \eta_0 + \eta_1 e + \eta_2 e^2$, where η_0 and η_1 are given by (41) and (43), respectively, and η_2 is to be determined. Using (38) and $\phi''(e) = 0$, it is obtained that

$$\eta''(e) = - \frac{\frac{\partial^2 F}{\partial \eta^2} \eta'^2 + 2 \frac{\partial^2 F}{\partial \eta \partial e} \eta' + \frac{\partial^2 F}{\partial e^2}}{\frac{\partial F}{\partial \eta}} \Big|_{(\eta(e), e)}, \quad (57)$$

and, therefore, that

$$\eta_2 = \frac{1}{2} \eta''(0) = - \frac{(3\eta_0 + 1)\eta_1^2 + g_1\eta_1 + g_2\eta_0}{3\eta_0^2 + 2\eta_0 + g_0}. \quad (58)$$

Expanding $\rho v^2 = \gamma_{12} - \gamma_{21}(\eta_0 + \eta_1 e + \eta_2 e^2)^2$ up to second order in e yields

$$\rho v_{12}^2 = s_0 + s_1 e + s_2 e^2, \quad (59)$$

where s_0 and s_1 are given by (45) and

$$\begin{aligned}
 s_2 = & (5 - 2\eta_0^2 - 2\eta_0\eta_2 - \eta_1^2)\mu + (7 - 2\eta_0\eta_1 - 4\eta_0^2)A/4 + 5\alpha_1 + [5 - \eta_0(\eta_1 + \eta_2) - \eta_1^2/2]\alpha_2 \\
 & + (5 - 2\eta_0\eta_1 - \eta_0^2/2)\alpha_3 + 3\alpha_4 + (15 - 4\eta_0\eta_1 - 3\eta_0^2)\alpha_5/4 \\
 & + 3(1 - \eta_0^2)\alpha_6 + (1 - \eta_0^2)\alpha_7 + 7(1 - \eta_0^2)\alpha_8/4 + (1 - \eta_0^2)\alpha_{10} + 3(1 - \eta_0^2)\alpha_{11}/4. \quad (60)
 \end{aligned}$$

Relation (59), where s_0 and s_1 are given by (45) and s_2 is given by (60), is the second-order approximation for the velocity. Now, consider that $\alpha_k = 0$, $k = \overline{1, 11}$, $k \neq 6$. Then, using (37) and (56) one obtains that $g_0 = 3$, $g_1 = 0$, $g_2 = 18 + 9(A/\mu) + 18(\alpha_6/\mu)$. Similarly, using (41), (43) and (58) one obtains that $\eta_0 = 0.2956$, $\eta_1 = 0$ and $\eta_2 = -(1.3806 + 0.6903(A/\mu) + 1.3806(\alpha_6/\mu))$. Introducing these results into (45) and (60) it is easy to obtain that

$$s_0 = 0.9126\mu, \quad s_1 = 3\mu + 0.9126A/4, \quad s_2 = 5.642\mu + 2.071A + 3.554\alpha_6, \quad (61)$$

which coincide with the coefficients of the approximation in [Destrade et al. 2010b, (19)], where the coefficient D is simply α_6 .

Expression of v_{23} associated with RW23. Introducing the expansion (27)₂ of γ_{23} into the relation $\rho v_{23}^2 = \gamma_{23}(1 - \eta_0^2)$ one obtains the second-order approximation as

$$\rho v_{23}^2 = (1 - \eta_0^2)[\mu + (-3\mu - A/2 + \alpha_3)e + (5\mu + \frac{7}{4}A - \frac{5}{2}\alpha_3 + 3\alpha_6 + \alpha_7 + \alpha_8 - \frac{3}{2}\alpha_{11})e^2]. \quad (62)$$

Expression of v_{21} associated with RW21. Following the same procedure used to obtain the second-order expansion for ρv_{12}^2 , one can write in this case that

$$\rho v_{21}^2 = s_0^{(21)} + s_1^{(21)} e + s_2^{(21)} e^2, \quad (63)$$

where $s_0^{(21)}$ and $s_1^{(21)}$ are determined using (54) and $s_2^{(21)}$ is given by

$$\begin{aligned} s_2^{(21)} = & (2 - 2\eta_0\eta_2 - \eta_1^2 - 6\eta_0\eta_1 - 5\eta_0^2)\mu + (1 - \frac{1}{2}\eta_0\eta_1 - \frac{7}{4}\eta_0^2)A - (4\eta_1 + 5\eta_0)\eta_0a_1 \\ & - (\eta_0\eta_2 + \frac{1}{2}\eta_1^2 + 5\eta_0\eta_1 + 5\eta_0^2)a_2 + (\frac{1}{2} - 2\eta_0\eta_1 - 5\eta_0^2)a_3 - 3\eta_0^2a_4 \\ & + (\frac{3}{4} - \eta_0\eta_1 - \frac{15}{4}\eta_0^2)a_5 + (1 - \eta_0^2)(3a_6 + a_7 + \frac{7}{4}a_8 + a_{10} + \frac{3}{4}a_{11}), \end{aligned} \quad (64)$$

where η_0 and η_1 are determined using (41) and (55), respectively, and η_2 is

$$\eta_2 = -\frac{(3\eta_0 + 1)\eta_1^2 + g_1^{(21)}\eta_1 + g_2^{(21)}\eta_0 - h_2}{3\eta_0^2 + 2\eta_0 + g_0^{(21)}}. \quad (65)$$

In (65), $g_0^{(21)}$ and $g_1^{(21)}$ are determined using (52) and the remaining symbols are given by

$$\begin{aligned} g_2^{(21)} = & \frac{2}{2\mu + a_2} (27\mu + \frac{51}{4}A + 17a_1 + 17a_2 + 24a_3 + 30a_4 + \frac{117}{4}a_5 + 27a_6 + 18a_7 + \frac{69}{4}a_8 + 12a_9 + 11a_{10} + \frac{27}{4}a_{11}) \\ & - 2 \frac{6\mu + 4a_1 + 3a_2}{(2\mu + a_2)^2} (5\mu + \frac{7}{4}A + 5a_1 + 5a_2 + 5a_3 + 3a_4 + \frac{15}{4}a_5 + 3a_6 + a_7 + \frac{7}{4}a_8 + a_{10} + \frac{3}{4}a_{11}) \\ & + 4 \frac{3\mu + \frac{A}{4} + 2a_1 + \frac{5}{2}a_2 + a_3 + \frac{1}{2}a_5}{(2\mu + a_2)^3} [(12\mu + 4a_1 + 2a_2 - 12a_3 - 12a_4 - 8a_5)\mu \\ & \quad + (A + 8a_1 + 6a_2 + 4a_3 + 2a_5)a_1 - (2a_2 + 6a_3 + 6a_4 + 4a_5)a_2] \end{aligned} \quad (66)$$

and

$$\begin{aligned} h_2 = & \frac{1}{(2\mu + a_2)^2} [(84\mu + 104a_1 + 104a_2 - 12a_3 - 24a_4 - 12a_5)\mu \\ & \quad + (4A + 48a_1 + 16a_3 + 8a_5)a_1 + (A + 8a_1 + 36a_2 - 2a_3 - 12a_4 - 4a_5)a_2]. \end{aligned} \quad (67)$$

5. Conclusions

The purpose of this analysis is to evaluate the mechanical properties of transversely isotropic incompressible nonlinear elastic materials such as certain soft biological tissues. We have considered an expanded strain energy function in terms of the Green strain tensor. More in particular we have focused on an energy function with elastic constants of second, third, and fourth orders in the Green strain tensor (see (5)). Homogeneous plane waves and Rayleigh surface waves have been examined in conjunction with the strain energy function (5). The speeds of shear waves and Rayleigh waves in the incompressible model (5) have been obtained. The formulas developed can be used to determine the elastic coefficients included in (5), although, it is not an easy task. The equations obtained in [Destrade et al. 2010b] are recovered from their corresponding formulas obtained in this paper. It has been noted that formulas for the speeds of Rayleigh waves that are linear in e depend on the coefficients included up to third-order terms in the strain-energy function (5). On the other hand, the speeds of Rayleigh waves given as second-order polynomials in e depend also on the coefficients included up to fourth-order terms in the strain-energy

function (5). This is particularly important since even though physical acousticians are interested in third order constants for anisotropic solids, workers in nonlinear elasticity, and furthermore, in soft biological tissues, work with finite extensions involving fourth order constants.

Acknowledgements

The work was supported by NAFOSTED (Vietnam National Foundation for Science and Technology Development) under grant 107.02-2012.12. Merodio acknowledges support from the Ministerio de Ciencia in Spain under the project reference DPI2011-26167.

References

- [Bigoni et al. 2007] D. Bigoni, D. Capuani, P. Bonetti, and S. Colli, “A novel boundary element approach to time-harmonic dynamics of incremental nonlinear elasticity: the role of pre-stress on structural vibrations and dynamic shear banding”, *Comput. Methods Appl. Mech. Eng.* **196**:41-44 (2007), 4222–4249.
- [Bigoni et al. 2008] D. Bigoni, M. Gei, and A. B. Movchan, “Dynamics of a prestressed stiff layer on an elastic half space: filtering and band gap characteristics of periodic structural models derived from long-wave asymptotics”, *J. Mech. Phys. Solids* **56**:7 (2008), 2494–2520.
- [Destrade and Ogden 2010] M. Destrade and R. W. Ogden, “On the third- and fourth-order constants of incompressible isotropic elasticity”, *J. Acoust. Soc. Am.* **128**:6 (2010), 3334–3343.
- [Destrade et al. 2010a] M. Destrade, M. D. Gilchrist, and R. W. Ogden, “Third- and fourth-order elasticities of biological soft tissues,”, *J. Acoust. Soc. Am.* **127**:4 (2010), 2103–2106.
- [Destrade et al. 2010b] M. Destrade, M. D. Gilchrist, and G. Saccomandi, “Third- and fourth-order constants of incompressible soft solids and the acousto-elastic effect”, *J. Acoust. Soc. Am.* **127**:5 (2010), 2759–2763.
- [Dowaikh and Ogden 1990] M. A. Dowaikh and R. W. Ogden, “On surface waves and deformations in a pre-stressed incompressible elastic solid”, *IMA J. Appl. Math.* **44**:3 (1990), 261–284.
- [Gennisson et al. 2007] J.-L. Gennisson, M. Renier, S. Catheline, C. Barriere, J. Bercoff, M. Tanter, and M. Fink, “Acoustoelasticity in soft solids: assessment of the nonlinear shear modulus with the acoustic radiation force”, *J. Acoust. Soc. Am.* **122**:6 (2007), 3211–3219.
- [Hamilton et al. 2004] M. F. Hamilton, Y. A. Ilinskii, and E. A. Zabolotskaya, “Separation of compressibility and shear deformation in the elastic energy density”, *J. Acoust. Soc. Am.* **116**:1 (2004), 41–44.
- [Hoger 1999] A. Hoger, “A second order constitutive theory for hyperelastic materials”, *Int. J. Solids Struct.* **36**:6 (1999), 847–868.
- [Holzapfel et al. 2000] G. A. Holzapfel, T. C. Gasser, and R. W. Ogden, “A new constitutive framework for arterial wall mechanics and a comparative study of material models”, *J. Elasticity* **61**:1-3 (2000), 1–48.
- [Ogden 1974] R. W. Ogden, “On isotropic tensors and elastic moduli”, *Math. Proc. Cambridge Philos. Soc.* **75**:3 (1974), 427–436.
- [Ogden 1984] R. W. Ogden, *Nonlinear elastic deformations*, Ellis Horwood, Chichester, 1984.
- [Ogden 2007] R. W. Ogden, “Incremental statics and dynamics of pre-stressed elastic materials”, pp. 1–26 in *Waves in nonlinear pre-stressed materials*, edited by M. Destrade and G. Saccomandi, CISM Courses and Lectures **495**, Springer, Vienna, 2007.
- [Ogden and Singh 2011] R. W. Ogden and B. Singh, “Propagation of waves in an incompressible transversely isotropic elastic solid with initial stress: Biot revisited”, *J. Mech. Mater. Struct.* **6**:1–4 (2011), 453–477.
- [Ogden and Vinh 2004] R. W. Ogden and P. C. Vinh, “On Rayleigh waves in incompressible orthotropic elastic solids”, *J. Acoust. Soc. Am.* **115**:2 (2004), 530–533.
- [Prikazchikov and Rogerson 2003] D. A. Prikazchikov and G. A. Rogerson, “Some comments on the dynamic properties of anisotropic and strongly anisotropic pre-stressed elastic solids”, *Int. J. Eng. Sci.* **41**:2 (2003), 149–171.

- [Prikazchikov and Rogerson 2004] D. A. Prikazchikov and G. A. Rogerson, “On surface wave propagation in incompressible, transversely isotropic, pre-stressed elastic half-spaces”, *Int. J. Eng. Sci.* **42**:10 (2004), 967–986.
- [Renier et al. 2007] M. Renier, J.-L. Gennisson, M. Tanter, S. Catheline, C. Barriere, D. Royer, and M. Fink, “Nonlinear shear elastic moduli in quasi-incompressible soft solids”, pp. 554–557 in *Proceedings of the IEEE Ultrasonics Symposium* (New York, 2007), IEEE, Piscataway, NJ, 2007.
- [Renier et al. 2008] M. Renier, J.-L. Gennisson, C. Barriere, D. Royer, and M. Fink, “Fourth-order shear elastic constant assessment in quasi-incompressible soft solids”, *Appl. Phys. Lett.* **93**:10 (2008), Art. ID #101912.
- [Vinh 2010] P. C. Vinh, “On formulas for the velocity of Rayleigh waves in prestrained incompressible elastic solids”, *J. Appl. Mech. (ASME)* **77**:2 (2010), Art. ID #021006.
- [Vinh and Giang 2010] P. C. Vinh and P. T. H. Giang, “On formulas for the Rayleigh wave velocity in pre-strained elastic materials subject to an isotropic internal constraint”, *Int. J. Eng. Sci.* **48**:3 (2010), 275–289.

Received 23 Aug 2012. Revised 15 Nov 2012. Accepted 17 Nov 2012.

PHAM CHI VINH: pcvinh@vnu.edu.vn

Faculty of Mathematics, Mechanics and Informatics, Hanoi University of Science, 334, Nguyen Trai Str., Thanh Xuan, Hanoi 1000, Vietnam

JOSE MERODIO: merodioj@gmail.com

Department of Continuum Mechanics and Structures, E.T.S. Ingeniería de Caminos, Canales e Puertos, Universidad Politecnica de Madrid, 28040 Madrid, Spain

TUBULAR ALUMINUM CELLULAR STRUCTURES: FABRICATION AND MECHANICAL RESPONSE

RYAN L. HOLLOMAN, VIKRAM DESHPANDE, ARVE G. HANSEN,
KATHERINE M. FLEMING, JOHN R. SCULLY AND HAYDN N. G. WADLEY

We explore a novel cellular topology structure based upon assemblies of square cross section tubes oriented in a cross-ply 2D and orthogonal 3D arrangements that can be tailored to support different combinations of through thickness and in-plane loads. A simple dip brazing approach is used to fabricate these structures from assemblies of extruded 6061-T6 aluminum alloy tubes and the through thickness compression of a variety of structures is investigated experimentally and with finite element modeling. We find that the 3D orthogonal structures have an approximately linear dependence of modulus upon relative density. However the strength has a power law dependence upon density with an exponent of approximately $5/3$. These cellular structures exhibit almost ideal plastic energy absorption at pressures that can be selected by adjustment of the vertical and in-plane tube wall thicknesses. A finite element model with a nonlinear hardening constitutive law is used to explore the buckling modes of the structure, and to investigate the relationship between cell topology, relative density, tube wall material properties and the cellular structures resistance to compression.

1. Introduction

Sandwich panel structures are widely used in stiffness dominated design where large bending stresses must be supported with minimum elastic deflection [Allen 1969]. In these scenarios, widely separated face sheets carry the primary loads and are constructed of light, stiff, strong materials such as light metals or fiber reinforced composites. When panel deflections are small, the mechanical performance is optimized by minimizing the core mass fraction [Zenkert 1995]. Since the flexural modulus of the sandwich panel increases with the square of the core thickness, the primary role of the core is to maintain separation of the faces and preserve the sandwich effect [Vinson 2001]. Cores for such applications can be made of low density materials such as Nomex with a hexagonal honeycomb cell topology [Bitzer 1997] or rigid polymer foams for less weight sensitive applications [Gibson and Ashby 1988; Mills 2007]. It is interesting to note that the development of these structures has been paced by advances in the adhesives used to strongly (and reliably) bond face sheets to the cores. More recently many other core options have emerged [Wadley 2006] including honeycombs with in-plane stretch resistant square [Wadley et al. 2007] or triangular [Wei et al. 2008] cell topologies, and flex honeycomb or lattice truss cores [Kooistra et al. 2008] for curved sandwich panels. Ways of making these cellular materials from engineering alloys such as high strength aluminum [Queheillalt et al. 2008; Kooistra et al. 2004] titanium [Queheillalt et al. 2000; Elzey and Wadley 2001; Moongkhamklang and Wadley 2010] and from composites have also been developed [Finnegan et al. 2007; Russell et al. 2008].

Keywords: cellular structures, 6061 aluminum, impact energy absorption.

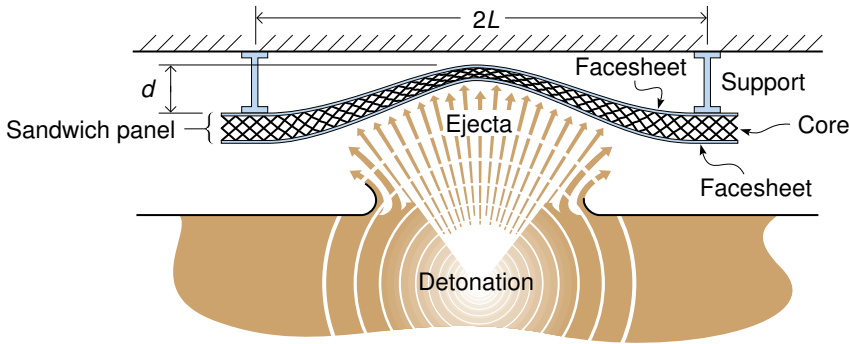


Figure 1. Example of a sandwich panel structure whose core undergoes localized compression, transverse shear, and membrane stretching during high intensity impulsive loading. The core in this example exhibits modest resistance to inplane stretching.

Sandwich panel structures have also attracted interest for impact energy absorption applications [Laurin and Vizzini 2005] and for reducing the dynamic deflections of structures that are subjected to high intensity dynamic loading [Vaziri et al. 2007]. Experimental studies have demonstrated significant reductions in panel deflections during shock loading under water [Wei et al. 2007], in air [Dharmasena et al. 2008] and when impacted by soil launched toward a panel by a buried explosion [Rimoli et al. 2011]. These studies reveal that the panel's out-of-plane deflection, d , scaled by the half span length, L , increases roughly linearly with the incident impulse I [Hutchinson and Xue 2005; Liang et al. 2007; McShane et al. 2007]. Under the most intense loadings, the deflections of edge clamped panels exceed the core thickness and the deformation of the panel changes to a combination of core crushing and in-plane stretching [Tilbrook et al. 2006]; see Figure 1. In this phase of the response, the resistance of the core to through thickness compression and in-plane stretching of the core and faces govern panel performance.

Sandwich structures intended for high intensity impulsive loading scenarios typically allocate about a third of the panels mass to the core to achieve the desired combination of core and face sheet responses [Wicks and Hutchinson 2001]. Foams [Reyes 2008], and tubes (both empty and foam filled) oriented axially to the crush direction [Hanssen et al. 2000a; Baumeister et al. 1997; Reid 1993] have been widely investigated for structural impact problems. These structures are highly compressible and can undergo compression at nearly constant stress to strains of 60% or more, making them efficient impact energy absorbers. However, they have little in-plane stretch or transverse shear resistance and are not optimally suited for the cores of edge supported sandwich panels subjected to high intensity loading. While honeycomb structures with square [Xue and Hutchinson 2006] or triangular [Gibson and Ashby 1997] cell topologies have shown promise for this application, (the webs resist compression and in the in-plane stretching), they are difficult to fabricate from the high performance alloys needed for many applications. Achieving the robust nodal connections between the core and face sheets is also problematic because of the small nodal contact area. It is difficult to independently vary, and thus tailor, the through-thickness and in-plane properties.

Here we investigate core topologies based upon 3D arrangements of square cross section, extruded tubes made from a heat treatable aluminum alloy. The tubes can be assembled in a 2D cross-ply, or 3D

orthogonal geometry. The in-plane tubes provide stretch resistance while the through thickness tubes resist compression. By using different wall thicknesses for the in-plane and through thickness tubes, it is possible to independently control the in-plane stretch resistance and the through thickness crush strength. The large nodal contact areas also improve load transfer within the core and between cores and face sheets. The topology affords multifunctionality [Evans et al. 2001] such as cross flow heat exchange via the open channels that extend within the structure [Tian et al. 2007]. We describe a simple method for the fabrication of tube core topology structures, and investigate their mechanical response under quasistatic compression loading. We find that a 3D orthogonal arrangement of tubes offers effective crushing resistance and appears well suited for impact energy absorbing applications.

2. Cell geometries and fabrication

To explore the design and fabrication of tube-bonded cellular structures we have investigated two rectangular cell topologies with and without tubes oriented in the loading direction and develop a method for their manufacture from extruded aluminum tubes.

2.1. Cell geometry. Rectilinear cellular tube structures can be assembled from square cross-section tubes to create the two topologies shown in Figure 2. The 2D structure in Figure 2(a) can be assembled by laying down a colinear layer of tubes each spaced a tube width apart. A second similarly spaced layer is then orthogonally placed on the first layer, and the assembly sequence repeated until a desired thickness is achieved. The 3D topology in Figure 2(c) can be assembled from the 2D structure by inserting additional

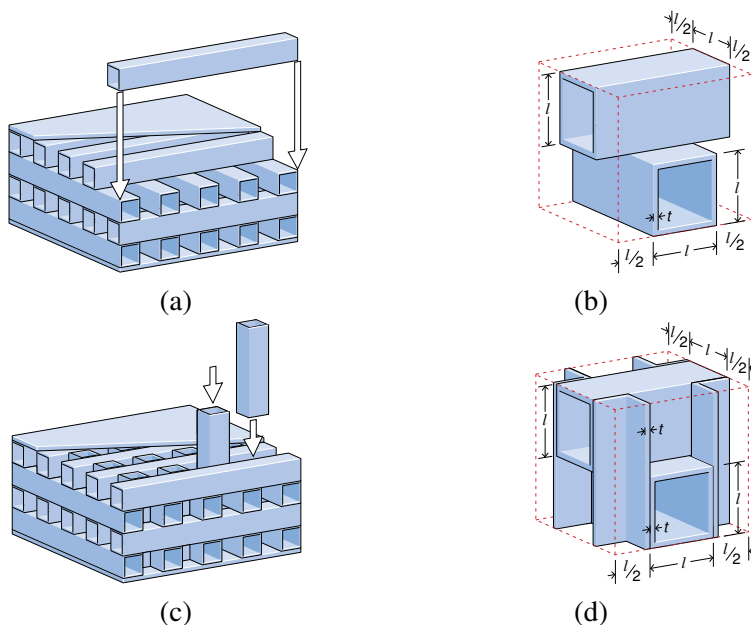


Figure 2. Examples of cellular structures fabricated from square extruded tubes. (a) 2D structure made by bonding 0/90 layers of colinear tubes. (b) The unit cell of the 2D structure. (c) A 3D tube structure where the through thickness gaps in the 0/90 assembly are filled with vertical tubes. (d) Unit cell of the 3D tube structure.

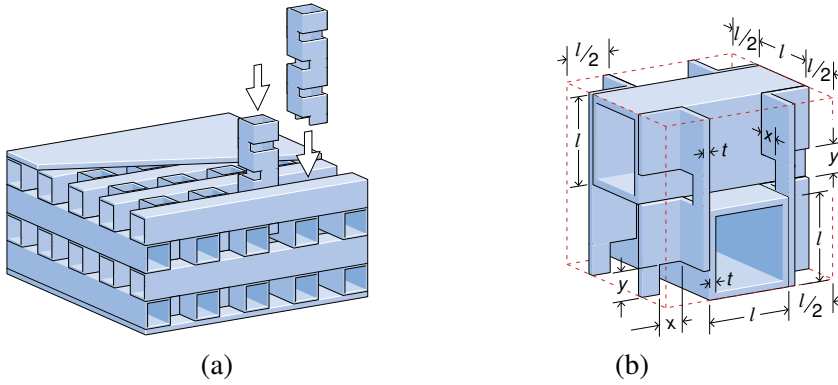


Figure 3. (a) A modified 3D structure in which the vertical tubes were notched to allow removal of salts used for dip braze bonding. (b) The unit cell of the modified 3D structure with the notch geometry incorporated. For all experiments reported here, $x = y = 6.35$ mm.

tubes in the out of plane (vertical) void space between the cross-ply oriented tubes. The tubes can be bonded with polymeric adhesives or more robustly by dip or vacuum brazing. To facilitate complete fluid penetration during dip braze bonding of the structure to face sheets, the vertically inserted tubes can be notched as shown in Figure 3. In principle, the wall thicknesses of the tubes in each orthogonal direction can be different, enabling tuning of properties in the various directions.

The structures are periodic and their unit cells are shown in Figures 2(b), 2(d) and 3(b). The relative density, $\bar{\rho}$, of each topology is defined as the fraction of volume occupied by solid in each unit cell. The relationship between $\bar{\rho}$, the tube wall thickness (t), and outer tube width (l) for the 2D topology is given by

$$\bar{\rho} = \frac{2(l-t)t}{l^2}. \quad (1)$$

The 3D topology assembled from identical tubes in all three directions has a relative density

$$\bar{\rho} = \frac{3(l-t)t}{l^2}. \quad (2)$$

However, use of notched vertical tubes, with rectangular notches of length x and height y , results in a reduced relative density for the 3D assemblies

$$\bar{\rho} = \frac{2 * t_v^2 (y - 2l) - t_v (2xy + l(y - 4l)) - 8t_h (t_h - l)l}{4l^3} \quad (3)$$

where the in-plane and through thickness oriented tubes can have different wall thicknesses of t_h and t_v , respectively. Figure 2 shows that when the cellular tube structures are bonded to face sheets to create sandwich panels, they have a large core to face sheet interfacial area with potentially beneficial consequences for the robustness of intensely loaded panels.

2.2. Cellular tube structure fabrication. Initial investigations of the mechanical response of a 2D core (described in Section 4) revealed unstable collapse and poor energy absorption characteristics during compressive loading. Only the 3D geometry is therefore examined in detail. The 3D orthogonal geometry

Topology	Average in-plane tube wall thickness (mm)	Average in-plane tube width (mm)	Average out of plane tube wall thickness (mm)	Average out of plane tube width (mm)	Relative density, $\bar{\rho}$
3D	3.47	19.05	3.47	19.05	42.7
3D	3.27	19.05	1.52	19.05	35.1
3D	1.53	19.05	3.30	19.05	28.6
3D	1.45	19.05	1.45	19.05	20.1
3D	0.74	11.48	0.74	11.48	11.6
3D, not notched	1.44	19.05	1.44	19.05	21.0
2D	1.70	19.05	-	-	16.3
1D array	-	-	1.52	19.05	6.7

Table 1. Tube geometries and predicted relative densities for tube-based cellular structures.

assembled from tubes of the same size, behaved well under compressive loading, and so samples were also assembled from tubes of various wall thickness and outer tube widths to investigate the effect of these geometric parameters upon energy absorption and collapse mechanisms. The geometries of all the structures investigated are summarized in Table 1. Since there was variability in the wall thickness, the wall thickness of fifty tubes was measured and the mean thickness was calculated and reported in the table. The standard deviation in tube wall thickness was ± 0.14 mm. These wall thickness variations were accounted for by the introduction of imperfections in the FE models described later (Section 5).

Samples of each cell topology were fabricated from square cross-section, 6061-T6 aluminum alloy extrusions using a simple dip brazing process followed by an aging heat treatment. Square cross-sectional extruded 6061-T6 aluminum alloy tubes were obtained from Argyle Industries Inc. (Branchburg, NJ, USA). To facilitate compression testing, a face sheet was attached to opposing sides of the samples to create sandwich panels. The 4.76 mm thick 6061-T6 aluminum alloy face sheet material was supplied by BMG Metals (Richmond, VA, USA).

A schematic illustration of the fabrication process for making the 3D orthogonal topology structure is shown in Figure 4. An analogous sequence was used for the 2D topology. All the test structures were dip brazed using a facility and process developed at Coleman Microwave Co. (Edinburg, VA, USA). This process involves a prebrazing cleaning, dip brazing, and a postbrazing heat treatment [ASM 2003]. The AA 6061-T6 parts were first subjected to a degreasing/chemical deoxidation process to remove the thick oxide films that form during extrusion processing and subsequent heat treatments. This involved soaking the tubes in a degreasing solution (Hurrifsafe 950 supplied by PCI of America of Rockville, Md, USA) at 65° to 82°C to remove hydrocarbon residues. After rinsing in warm water, the parts were dipped in a caustic bath (Isoprep 35 supplied by MacDermid of Denver, CO) for 30 seconds to lightly etch the surface. After a second warm water rinse, the parts were dipped for 30 seconds in a neutralizing acid bath (Gil-Sparkle C solution diluted 50% with de-ionizing water). The parts were again rinsed in a warm water bath before dipping for 45 seconds in a deoxidizing solution containing ferric sulfate, sulfuric acid, and nitric acids followed by rinsing in warm water and air drying. Once cleaned, the extrusions were assembled into the appropriate sandwich geometry. During assembly, Lynch Metal (Union, NJ) grade 4047 Al-Si filler foil was applied to the surfaces of the cellular structure as shown in Figure 4.

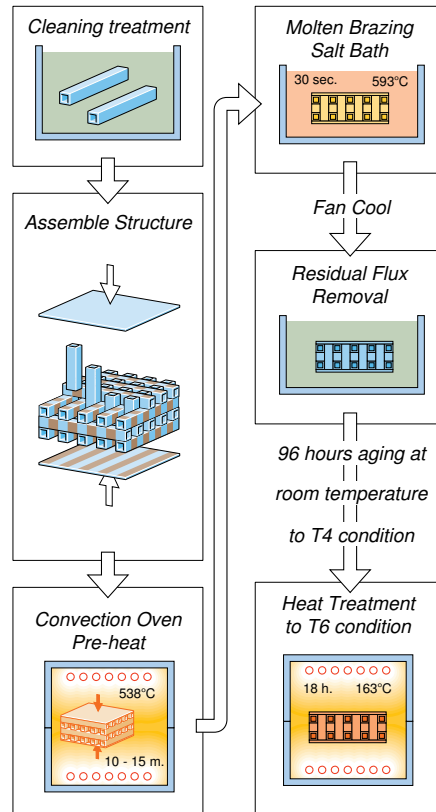


Figure 4. A process flow chart for the manufacturing sequence used to fabricate the cellular tube structures.

Filler alloy 4047 was used due to its improved fluidity (wetting action) and for minimizing solidification cracking. A bead of AA 4145 filler paste (Omni/Lucas Milhaupt grade LTB 37-SSK) was also applied to any small gaps within the assembly. In the case of the 3D structures, it is assumed that AA 4145 was used in very limited quantities and only along small joints at the edge of the 3D structure. [Table 2](#) summarizes the compositions of the AA 6061, AA 4047, and AA 4145 alloys, whose compositions and braze process conditions governed the microstructure [[Fleming et al. 2012](#)]. It should be noted that perfect tube alignment for all tested structures was difficult to maintain with the fabrication method used here. The tubes slid and it was difficult to attain perfect alignment even with clamping the face sheets. Both tube wall thickness variability and misalignment are imperfections that trip tube buckling modes during subsequent compression testing.

After assembly, the cellular structure was clamped to the top and bottom face sheets and the entire assembly mounted on a rack for dip brazing. The assembly was preheated for 10–15 minutes at 538°C (just slightly below the brazing temperature) in a hot air convection oven to remove moisture [[ASM 2003](#)]. The structures were then quickly transferred to a 593°C bath of molten brazing flux (Alu-braze 960, Park Metallurgical, Detroit, MI) for approximately 30 seconds, this acted as both a heating medium and deoxidizer. During this emersion, the molten braze alloy flowed (by capillary action) to fill the joints. After removal

Material	Composition (wt%)							
	Si	Cu	Mg	Mn	Fe	Cr	Zn	Mg/Si
AA 6061	0.4–0.8	0.15–0.4	0.8–1.2	0–0.15	0–0.7	0.04–0.35	0–0.25	0.5–1.5
AA 4047	11.0–13.0	0.3	0.1	0.15	0–0.8	0	0–0.2	0.009max
AA 4145	9.3–10.7	3.3–4.7	0.15	0–0.15	0–0.8	0	0–0.2	0.016max

Table 2. Composition of extruded material (AA 6061) and filler materials used to braze the tube profiles [Hatch 1984; Braithwaite 2008].

from the molten flux bath, molten salt was drained from the structure, and it was fan cooled to room temperature at rates ranging from 0.08 to 0.32 K/s, depending on the size of the structure. The structure was then soaked in hot-agitated water and Gil-Sparkle C solution with a 50% de-ionized water. After these fabrication steps, the structure was slow-aged at room temperature for 96 hours to the T4 condition and then peak hardened (to the T6 condition) by ageing at 163°C for 18 hours followed by water quenching.

3. Materials characterization

3.1. Microstructure characterization. Micrographs of the parent alloy and brazed regions of one of the structures studied here are shown in Figure 5, all samples were electropolished [Fleming et al. 2012] prior to imaging. Figure 5(a) shows a backscattered SEM micrograph of the tube wall material for a region more than 125 μm from a brazed joint. In the post brazed and heat treated condition, the tube wall

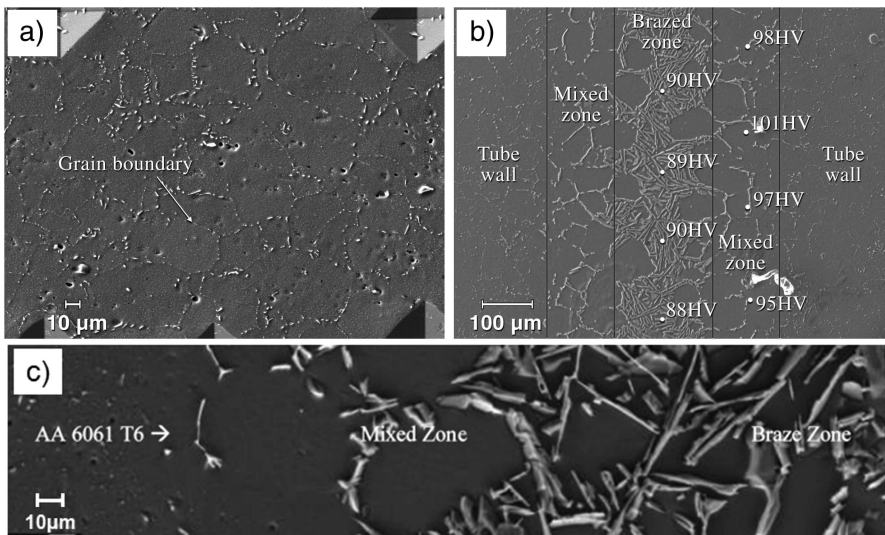


Figure 5. SEM images of the post-brazed and heat treated AA 6061-T6 material. (a) Backscatter electron image of the extruded tube wall showing precipitate phases decorating the grain boundaries. (b) The brazed region between two tubes showing silicon rich phases. Microhardness values are shown within the brazed and mixed zones. (c) A higher magnification view of the brazed and mixed zone regions.

material has an average grain size of $20\ \mu\text{m}$. The grain boundaries were decorated by large $\beta\text{-Mg}_2\text{Si}$ and $\text{Q-Al}_4\text{Cu}_2\text{Mg}_8\text{Si}_7$ phase precipitates, as predicted in [Chakrabarti and Laughlin 2004]. Fleming et al. [2012] has conducted a detailed examination of the microstructure evolutions accompanying the dip braze bonding process used here. The large β -phase grain boundary particles are consistent with the time-temperature transformation curves calculated by Fleming and the slower than normal rate of cooling after brazing. The brazed regions between the tubes, Figure 5(b) consisted of a eutectic structured region and a transition zone to the parent alloy microstructure. Within the brazed joint, the AA 4047 braze foil had fully melted and an fcc aluminum solid solution and diamond cubic silicon eutectic microstructure had formed upon cooling. Both β and $\text{Q-Al}_4\text{Cu}_2\text{Mg}_8\text{Si}_7$ phases were predicted [Fleming et al. 2012] to be responsible for the strengthening in this region. The Vickers microhardness in the brazed and mixed regions was measured to be approximately 90 HV30 and 98 HV30, respectively; equivalent to tensile strengths of 285 and 300 MPa. In the mixed zone on either side of the original braze foil location, Figure 5(c), resolidified AA 6061 formed coarse grains with Al-Si eutectic at solidification boundaries. Kinetic models and composition profiles [ibid.] have shown that significant outward diffusion of silicon and inward diffusion of magnesium had occurred in a zone that extended $125\ \mu\text{m}$ from the edge of the brazed zone. Strengthening in this region resulted from precipitated Si, as well as β , and Q phase precipitation in Al-rich phase [ibid.]

3.2. Alloy mechanical properties. An optical image of a polished cross section cut from a 3D structure is shown in Figure 6. Microhardness measurements were made at various locations (all further than $125\ \mu\text{m}$ from any brazed region) to investigate the local strength of the post brazed/artificially age hardened

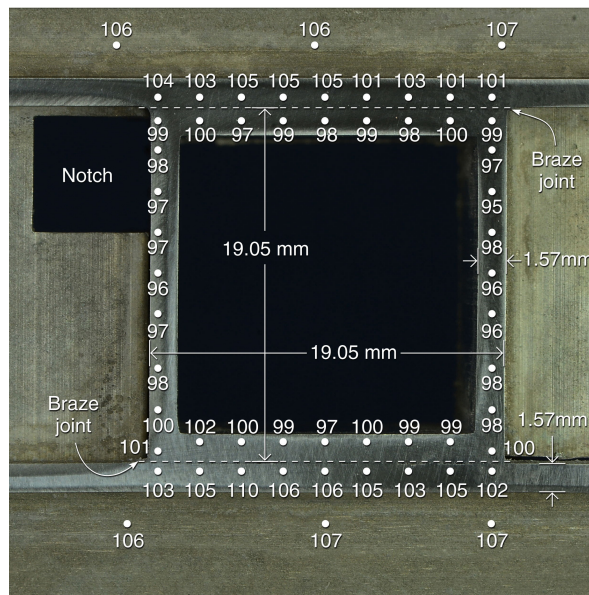


Figure 6. A photograph of a polished cross sectional slice through the 3D tube structure with measured Vickers microhardness values superimposed. A notch in one of the vertically oriented tubes can be seen in the upper left. All microhardness measurements are located in the AA 6061-T6 extrusion region.

extrusion region of the structure. These hardness values and approximate location of the measurement are shown in [Figure 6](#). The measured Vickers microhardness lay in the range of 102 ± 7.5 HV30; equivalent to an alloy tensile strength of approximately 330 MPa, which is consistent with the T6 condition of the 6061 alloy. Indents made in the outer surface of the tube wall, indicated a hardness that deviated very little from 107 HV. However, when measured on a plane transverse to the extruded direction, the microhardness was roughly 10 HV smaller, and fluctuated between 95 HV and 102 HV. The microhardness indentation diameter was about 0.1 mm, while half the tube wall thickness was 0.8 mm. As a result the distance to the free surface from the middle of the tube wall was about eight times the indent diameter, and proximity to the free surface may have reduced lateral constraint during indentation. Hardness measured in the same orientation near the two (horizontal) brazed joints, indicated a hardness that varied between 101 and 110 HV consistent with better lateral constraint. We conclude that the strength of the tube wall alloy after brazing was approximately isotropic and independent of orientation.

Quasistatic tensile tests were used to determine the stress-strain response of the post-brazed and T6 aged 6061 tube wall alloy. The tensile test specimens were cut so that the loading direction was in the axial (extrusion) direction of the orthotropic tube material. The test coupons were prepared according to ASTM standard B557-06 and tested on a 50 kN screw driven universal testing machine (Instron Model 4208, Instron Corp, Canton, MA, USA) at 25°C at a strain rate $\dot{\epsilon}$ of 10^{-4} s^{-1} . The specimen's axial displacement was determined with a laser extensometer (Electronic Instrument Research, Model LE-01, Irwin, PA, USA). The specimens were tested to failure and the Cauchy stress, σ_c and the logarithmic strain ϵ_L , up to diffuse necking were calculated from

$$\sigma_c = \frac{F}{A_0(1 + \epsilon)}, \quad \epsilon_L = \ln \frac{L_2}{L_1} \quad (4)$$

where F is the force, A_0 is the initial cross section of the tensile coupon, ϵ is the engineering strain, L_1 the initial gauge length and L_2 the extended length.

To verify that material in the post brazed 3D orthogonal assembly had the same mechanical properties throughout its interior, tests were performed on material extracted from the walls of tubes located at the surface and the interior of the sample. Two samples from each location within a 3D cellular structure were obtained and tested. In addition, the AA 6061-T6 face sheet material was also tested in the rolling and transverse directions. [Figure 7](#) shows the cauchy stress-logarithmic strain curve for one of the tube wall material samples. This curve was subsequently used to deduce the material properties for the numerical simulations of the 3D orthogonal assembly. A summary of the mechanical test results for all the samples is shown in [Table 3](#). It is evident that there is little variation in the mechanical properties within the tube structure, and the ultimate strengths are consistent with the microhardness measurements.

The mechanical response of the brazed joint was also investigated using a lap shear test in accordance with test standards specified by ASTM D1002-05. The test specimens were cut in the length direction of the extruded tube and underwent the same brazing and age-hardening process described in [Section 2.2](#). Tests were conducted at a strain rate of 10^{-5} s^{-1} in the specimens gauge area. In three tests, the AA 6061-T6 material failed prior to the braze joint near the grips at a tensile stress of 247 MPa. The corresponding shear stress within the joint at the point of material failure was measure to be 165 MPa. Since no nodal fracture was observed at the brazed lap joint during these tests, the nodes of the adjacent tubes in the FE models ([Section 5](#)) were merged prior to simulations.

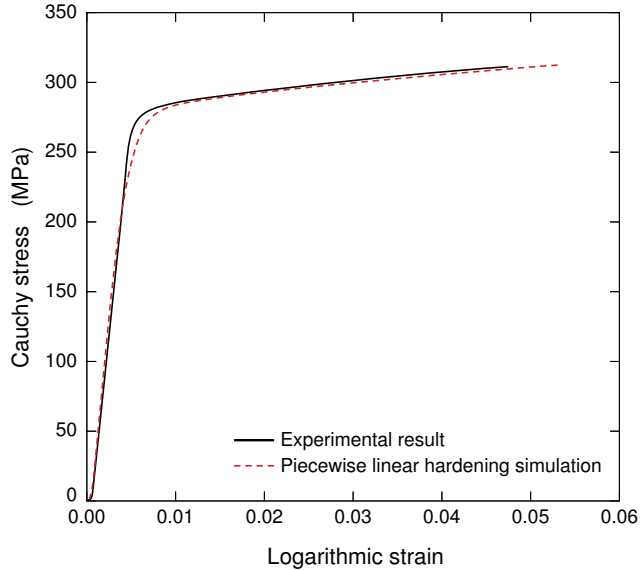


Figure 7. Measured true stress-logarithmic strain curve for post-brazed and fully age hardened AA 6061-T6 tube wall material tested in uniaxial tension to fracture at room temperature. The stress-strain curve predicted by a piecewise linear hardening constitutive model used in subsequent simulations is also included.

Direction	Modulus, E_s (GPa)	Yield strength, σ_{02} (MPa)	Ultimate strength, σ_u (MPa)	Total strain to failure ϵ_f (%)
Exterior region of 3D structure				
Axial	70.5	278.2	310.5	5.3
Axial	69.9	280.9	311.5	5.1
Interior region of 3D structure				
Axial	68.5	284.5	313.6	4.9
Axial	68.3	283.2	312.8	4.9
Face sheet material				
Transverse	69.4	265.9	346.8	12.5
Rolling	71.4	281.4	344.3	12.7

Table 3. Mechanical properties of 3D orthogonal structure and face sheet.

4. Compressive response of cellular structures

The compressive stress strain response of the cellular structures were measured following the guidelines of ASTM C 365/C for sandwich panel testing at an applied engineering strain rate of 10^{-4} s^{-1} . A laser extensometer was used to measure the compressive displacement and thus nominal strain.

4.1. The 2D cellular structure. The out of plane compressive response of the 2D structure with $\bar{\rho} = 16.3\%$ is shown in Figure 8. The stress linearly increased with an elastic modulus (measured during

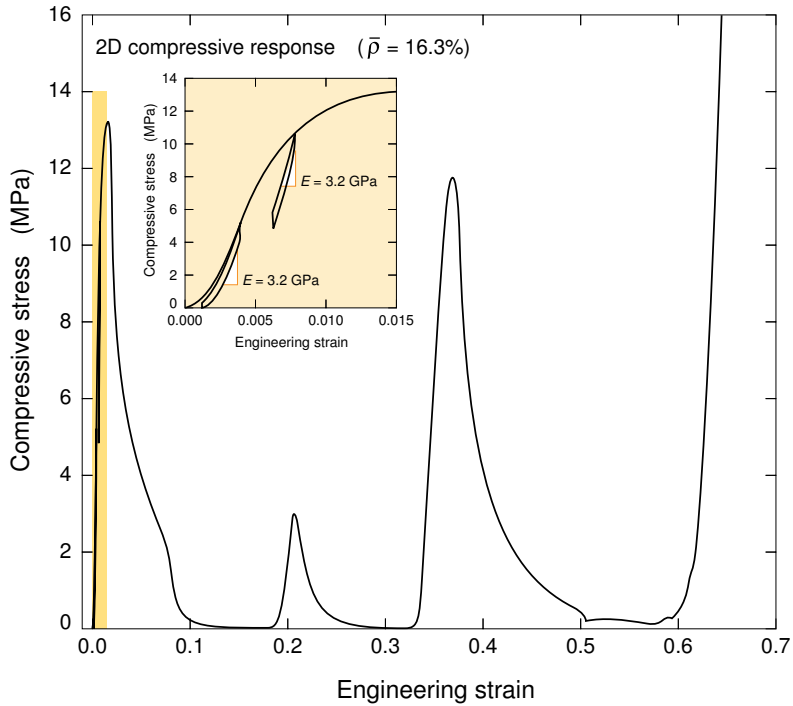


Figure 8. The compressive stress-strain response of a 2D cellular structure with a relative density of 16.3%. The inset shows an expanded view of the nominally elastic loading region of the test where the unloading modulus was measured.

unloading) of 3.2 GPa until reaching an initial peak of 13.2 MPa. Continued loading resulted in rapid softening and a significant period of compression at almost no stress. This was then followed by a second

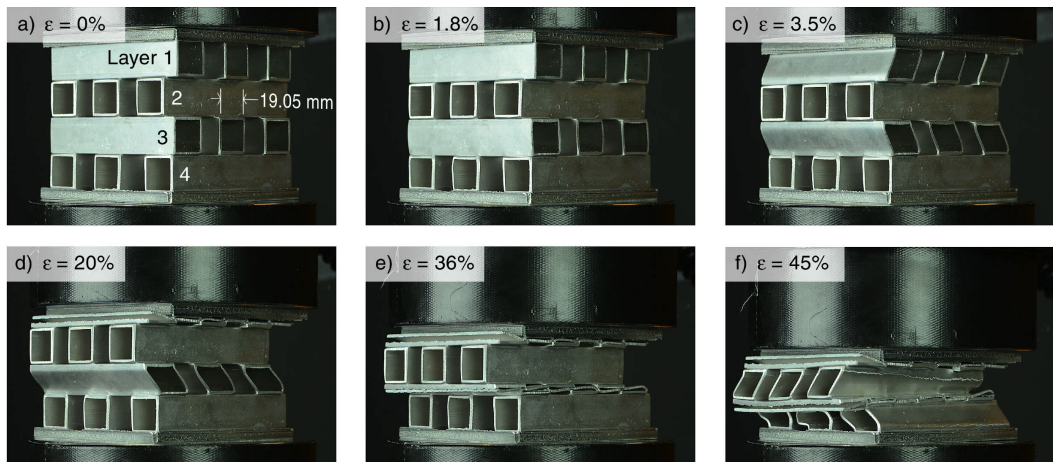


Figure 9. A photographic sequence showing the unstable collapse modes of a 2D cellular structure with a relative density of 16.3%.

rise in stress to a peak value of 3.1 MPa at a strain of 0.19 followed again by rapid softening. A third stress peak was observed with a maximum stress of 11.8 MPa at a strain of 0.35. Further loading again resulted in rapid softening until densification set in at a strain of 0.64.

Figure 9 shows a series of photographs of the 2D structure at various stages of the test. A comparison of parts (a) and (b) shows that the initial peak in strength was controlled by concertina buckling of layers 1 and 3 in which the tubes on either side of a horizontal plane rotate in opposite directions forming a chevron pattern; see Figure 9(c). Part (d) indicates that the second stress peak results from the complete collapse of layer 1. Examination of parts 9(e) and 9(f) show that the third stress peak resulted from collapse of layers 2 and 4 by the concertina buckling mode. Some variability of response was also observed. In some tests, the stress-strain response exhibited only two peaks that resulted from simultaneous collapse of layers 1 and 3, and then layers 2 and 4. Apparently small imperfections in the structure influenced the details of the buckling sequence, but not the generally unstable response of this structure.

The total absorbed (plastically stored) energy per unit volume, E_v , is obtained from the area under the stress-strain curve shown in Figure 8. The integration is usually terminated at the densification strain, ϵ_D defined here as the strain where the flow stress reaches the initial yield stress ($\epsilon_D = 0.64$ for this sample). This gave an energy absorbed per volume, $E_v = 1.2 \times 10^6 \text{ J/m}^3$. Dividing this by the core density $\bar{\rho}\rho_s = 0.163 \cdot 2.7 \times 10^3 \text{ kg}\cdot\text{m}^{-3} = 440.1 \text{ kg}\cdot\text{m}^{-3}$ (where ρ_s is the density of the solid) gave an energy absorbed per unit mass, $E_m = 2.72 \text{ J/g}$. If the stress achieved at the first peak had remained constant until densification, the energy absorbed per unit mass in the 2D structure would have been the theoretical limit, $E_m = 19.1 \text{ J/g}$. Defining the energy absorbing efficiency as the ratio of measured energy absorption, E_m , versus the theoretical estimate for E_m , the 2D structure has an energy absorption efficiency of 14.2%. The low efficiency is a result of the unstable buckling response of the structure and makes the 2D core poorly suited for impact energy absorption applications. It was therefore investigated no further.

4.2. The 3D structure. The 3D cellular structures defined in Table 1 had relative densities of 42.7, 20.1, and 11.6% and were made of tubes of identical wall thickness in each orthogonal direction. The 20.1%

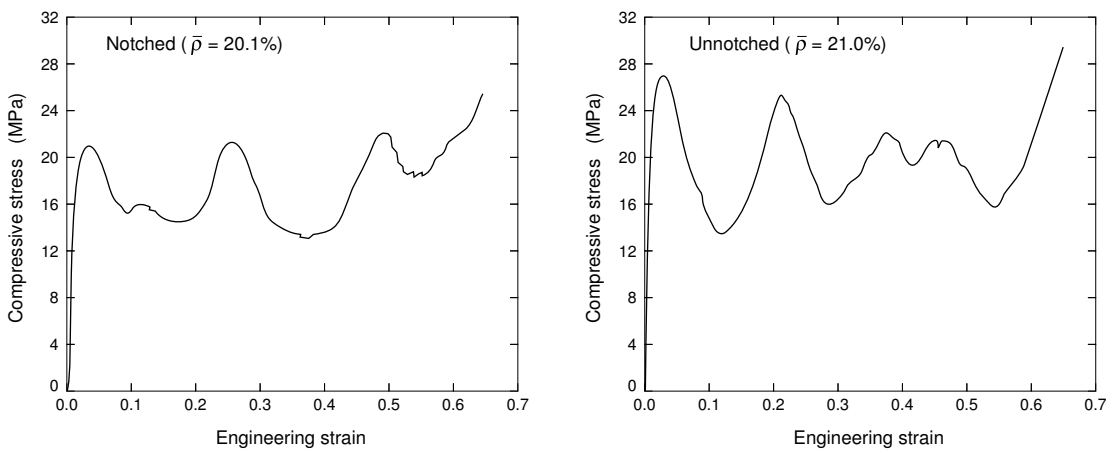


Figure 10. A comparison of the compressive stress-strain responses for 3D cellular structures assembled using notched (left) and unnotched (right) vertical tubes. The small difference in relative density results from removal of the notch material.

relative density structure represents the 2D structure in [Section 4.1](#), but with a notched tube inserted into the void of the colinearly aligned tubes, [Figure 3\(a\)](#). Its out of plane compressive response is shown in [Figure 10](#), left. The structures unload modulus during initial loading was 3.1 MPa. It reached an initial peak in strength of 20.9 MPa and then underwent moderate softening before hardening twice more to reach a strength about equal to that of the first peak. The sample then began to densify at a strain $\epsilon_D = 0.61$. The notched structure had an absorbed energy per unit volume, $E_v = 10 \times 10^6 \text{ J/m}^3$ and an energy absorbed per unit mass of $E_m = 19.2 \text{ J/g}$. Its energy absorption efficiency was 81.0%.

To ascertain the effect of the notching, an otherwise identical cellular structure to that with a relative density of 20.1% was fabricated without notches in the through thickness tubes, and its compressive stress-strain response is shown in [Figure 10\(b\)](#). The slightly higher relative density of the unnotched structure (21.0%) was due to additional mass of the unnotched vertical tubes. It can be seen that notching

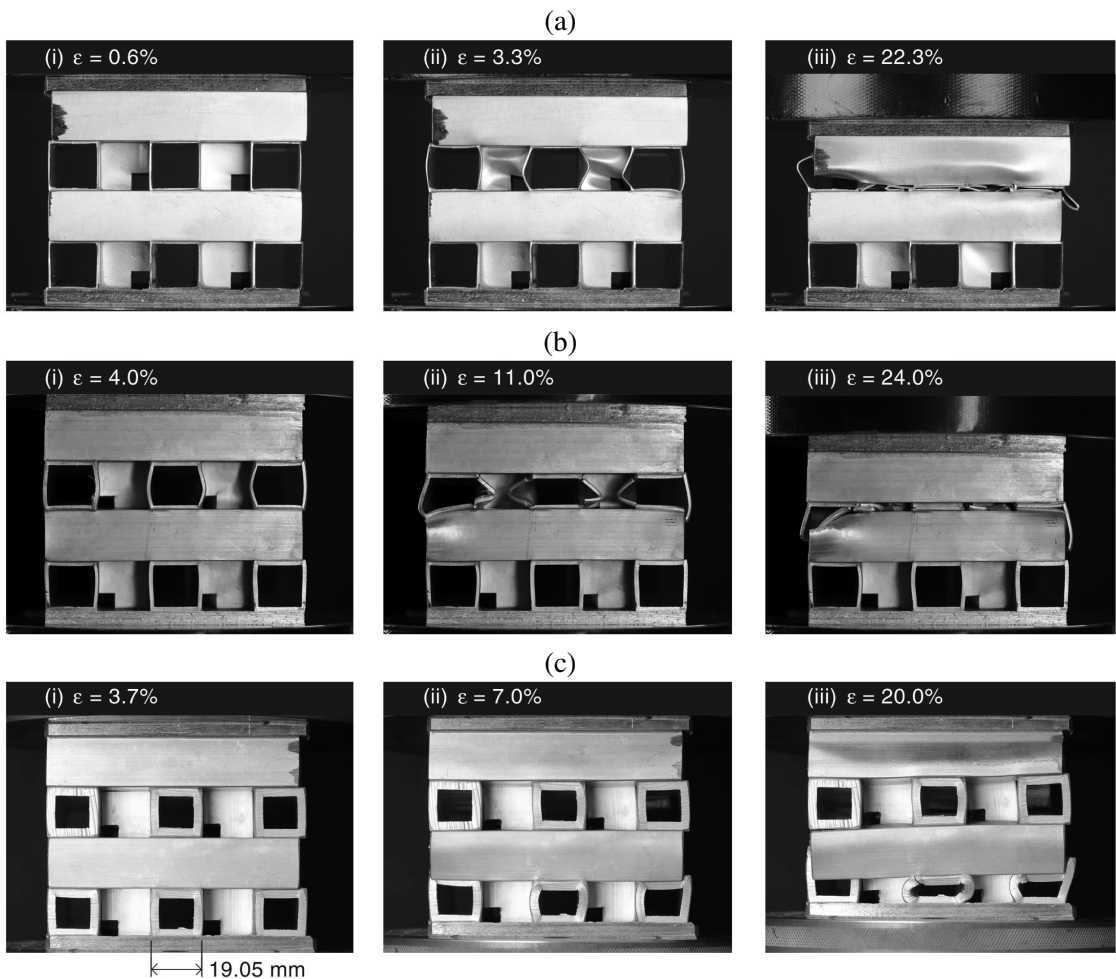


Figure 11. Photograph sequence of the collapse modes for 3D structures with relative densities of (a) 11.6, (b) 20.1, and (c) 42.7%. The strains at which each photograph was taken are indicated on [Figure 12](#).

reduced the initial peak strength of the 3D structure from 27.1 MPa to 20.9 MPa but also reduced the amplitude of the stress fluctuations. The energy absorbed per unit volume for the unnotched sample $E_v = 12.45 \times 10^6 \text{ J/m}^3$ while $E_m = 21.94 \text{ J/g}$, which were both higher than those of the notched structure. However, the large stress drops observed in the sample with no axial tube notches reduced its energy absorption efficiency from 81.0 to 72.3%.

A photograph of the notched 3D structure with a relative density of 20.1% taken at the first peak in stress (at a strain of 0.04) is shown in Figure 11(b)(i). The drop in strength at the first peak resulted from the onset of buckling of the set of tubes oriented in the through thickness direction. This was nucleated at the notches in the tubes shown in the photographs of Figure 11(b). Continued loading resulted in softening to a relatively constant stress of approximately 15 MPa, Figure 12. At this stage, the buckles were fully formed in the through thickness tubes, and the side walls of the cross-ply tubes then began to buckle, Figure 11(b)(ii). This was accompanied by a second rise in stress at a strain of 0.21 that reached a peak value of 21.8 MPa as densification of layer 2 occurred, Figure 11(b)(iii). This process was repeated until each of the four cross-ply tube layers had densified at a strain $\epsilon_D = 0.61$.

The out of plane compressive response for cores with three different relative densities is compared in Figure 12. The ultimate peak strength of the 42.7, 20.1, and 11.6% relative density structures were

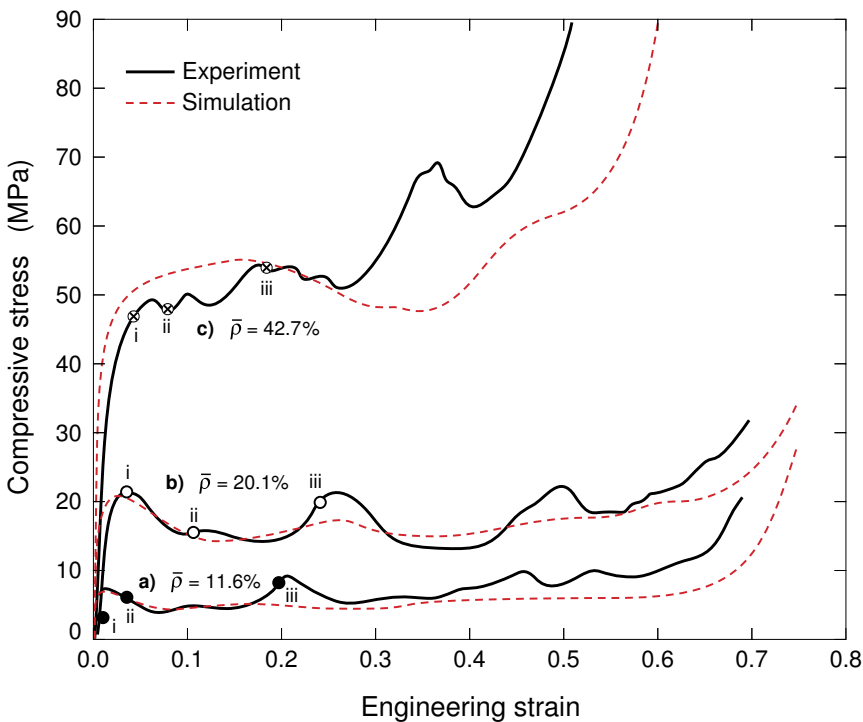


Figure 12. The compressive stress-strain responses of notched 3D cellular structures made from uniform wall thickness tubes with relative densities of 11.6, 20.1 and 42.7%. The structures exhibit a relatively flat stress-strain response after initial yield until attainment of a density dependent “densification strain” whereupon the stress rises sharply. The dashed curves correspond to FEA simulations discussed later.

Topology	Relative Density, $\bar{\rho}$	Peak stress, σ_p (MPa)	ϵ_D	E_v (MJ/m ³)	E_m (J/g)	Theoretical E_m (J/g)	Energy absorbing efficiency
3D	42.7	69.1	0.45	24.4	21.2	29.4	0.73
3D	35.1	53.3	0.51	23.8	25.1	27.5	0.91
3D	28.6	36.8	0.50	14.7	19.0	23.1	0.82
3D	20.1	21.8	0.61	10.4	19.2	23.7	0.81
3D	11.6	9.7	0.59	3.9	12.7	13.7	0.92
3D, no notch	21.0	27.1	0.63	12.5	21.9	30.1	0.72
2D	16.3	13.2	0.64	1.2	2.7	19.1	0.14
1D array	6.7	4.7	0.72	1.7	18.0	35.2	0.51

Table 4. Energy absorption values for tested tubular cellular structures.

69.1, 21.8, and 9.7 MPa respectively, and was controlled by buckling of the through thickness tubes, [Figure 11\(a\)–\(c\)](#). This buckling is clearly seen in [Figure 11\(a\)\(ii\)](#). Further collapse results from the folds in the vertical tube walls buckling into the cross-ply oriented tubes. The stress-strain curves of all three structures exhibit relatively constant stress until their (density dependent) densification strain was reached. [Table 4](#) summarizes the measured mechanical properties for all the samples.

4.3. Effect of tube wall thickness. [Figure 13\(a\)](#) shows the stress-strain responses of 3D structures in which the wall thicknesses of the in- and out-of-plane tubes were different. Recall that the 3D structure with equal tube thickness in all directions had a relative density of 42.7%. Its stress-strain response was shown in [Figure 11\(c\)](#). The wall thickness of just the out-of-plane tubes was reduced by a half, and the relative density decreased to 35.1% (82% of the isotropic structure), but the strength dropped by only 5%, [Figure 13\(a\)](#). A larger decrease in strength occurred when only the in-plane tube wall thicknesses were reduced by one half (while keeping the out-of-plane tubes at the original wall thickness). In this case, the relative density decreased to 28.6% (66% of the isotropic structure) and the peak strength was reduced by approximately 54%. From the images in [Figure 13\(b\)](#) and (c), the initial peak strength is seen to be controlled by a similar mechanism to that observed in isotropic samples with identical tube wall thicknesses. We also note that the structures with relative densities of 35.1% and 28.6% had excellent energy absorbing characteristics, with efficiencies of 91% and 82%, respectively; see [Table 4](#).

4.4. Tube interactions. To experimentally investigate possible interactions between tubes in the in- and out-of-plane directions, only the colinearly aligned (in-plane) tubes from the 3D structure with a relative density of 16.3% were tested in out-of-plane compression, [Figure 14\(a\)](#). The vertical notched tubes in this colinear tube structure were then also tested in (axial) compression. The response of this 1D array structure is shown in [Figure 14\(b\)](#). The stress-strain response for a 3D structure made by combining both sets of tubes is shown in [Figure 14\(c\)](#). The in-plane and out-of-plane tube cells have initial peak strengths of 13.2 and 4.7 MPa, respectively. The addition of these strengths (17.9 MPa) is seen to be less than that of the fully assembled 3D structures first peak (20.8 MPa). The experiment indicates the existence of a synergistic interaction between the colinear aligned and vertical tubes. In the same way that the peak strength of the 3D assembly cannot be reproduced by summation of the colinear and vertical

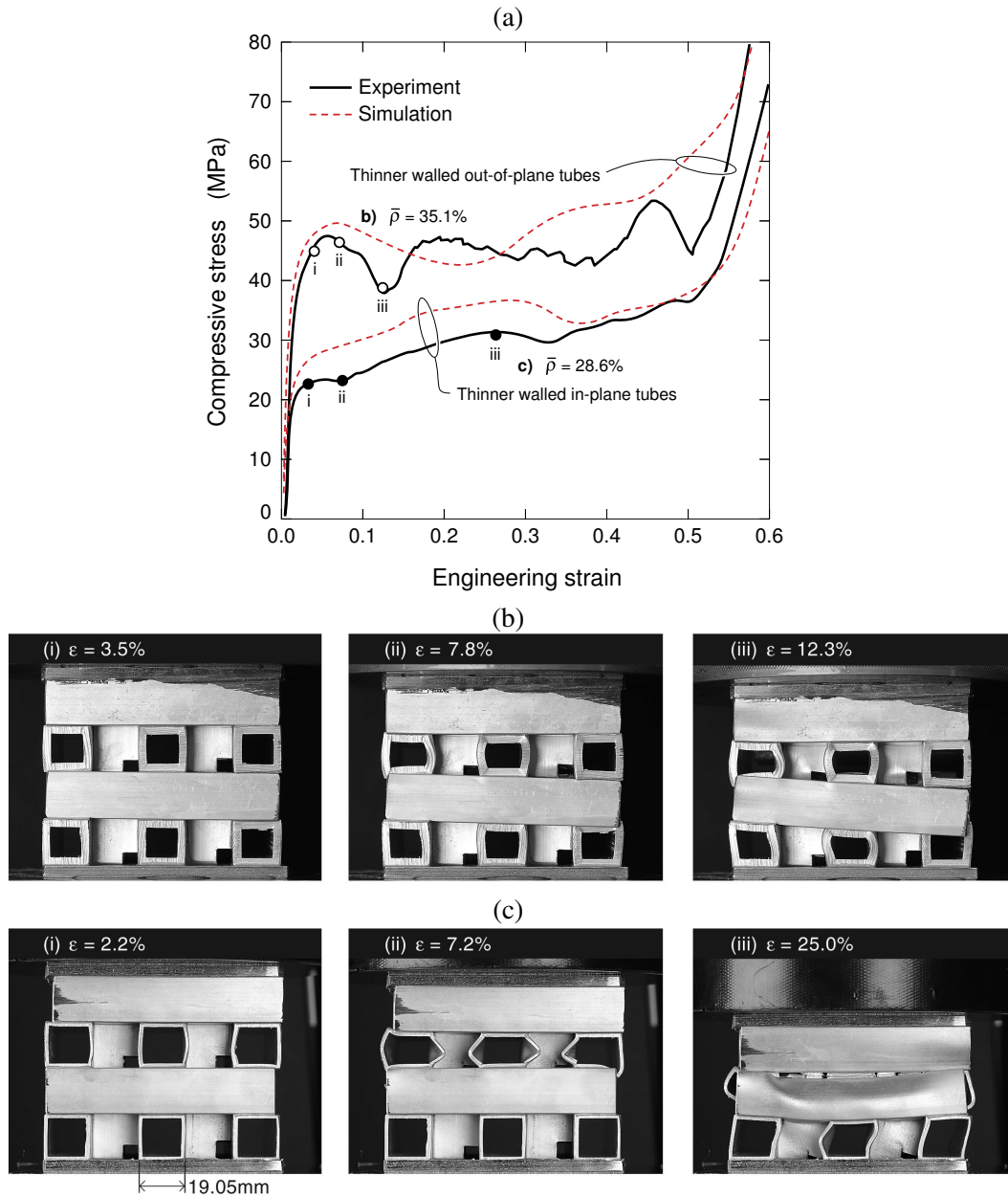


Figure 13. (a) The compressive stress-strain responses for notched 3D cellular structures in which the tube wall thicknesses in the vertical and horizontal directions were different. (c) The sample with a relative density of 28.6% density used in-plane tubes with a reduced wall thickness (of 1.57 mm). (b) The sample with a relative density of 35.1% was constructed using vertical tubes with a reduced thickness of 1.57 mm. The dashed curves correspond to FEA simulations discussed later. (b) and (c) show the collapse modes of the two structures. The in-plane tubes buckle first in (c) while the vertical tubes initiate failure in (b).

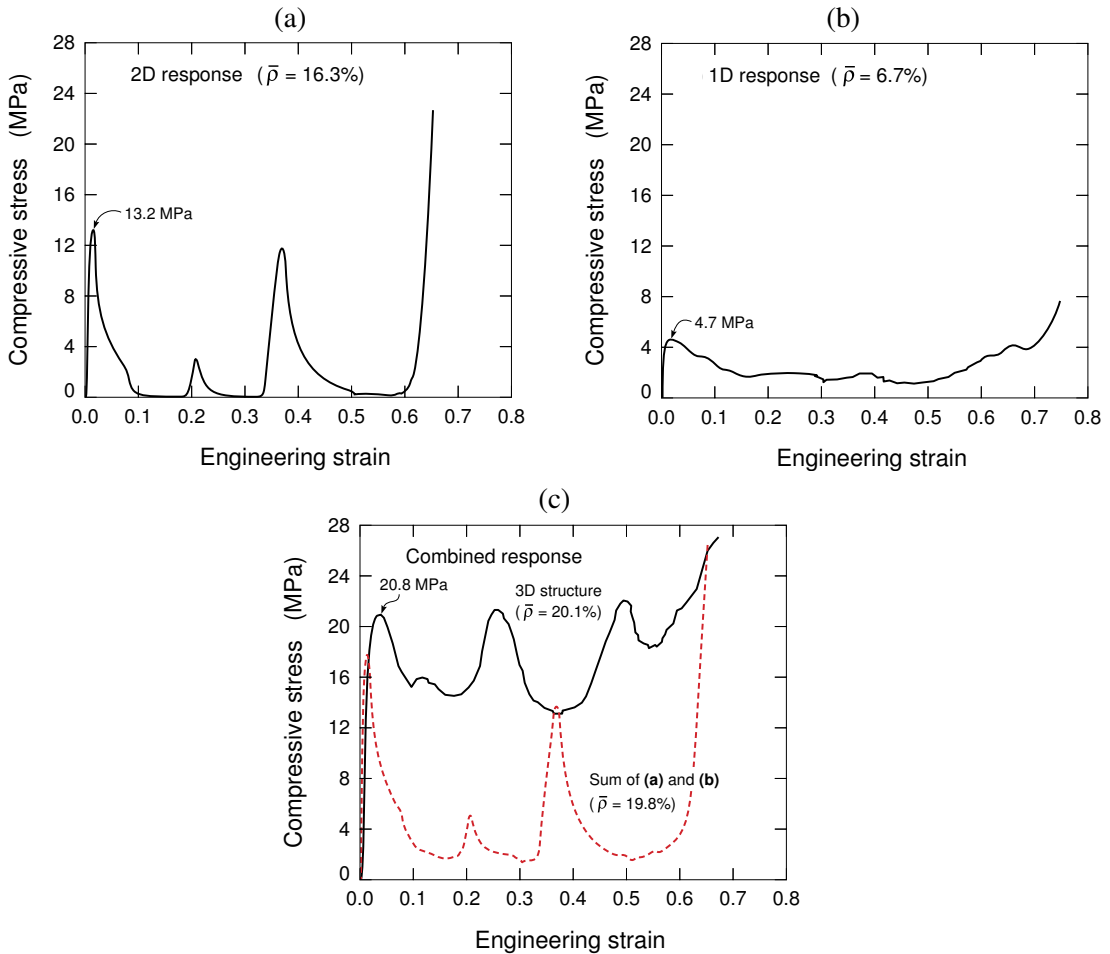


Figure 14. Measured stress-strain curves for a structure composed of (a) colinear aligned (0/90) tubes and (b) only the vertical tubes used in the 3D assembly. (c) Compares the summed response of (a) and (b) with that measured for the 3D structure. Note the considerable increase in energy storage of the 3D structure.

tubes acting separately, the energy absorbed per unit volume for the 3D assembly also cannot be achieved by summing that of its components. The energy absorption per unit volume is increased in the 3D core by more than the summed energy absorbing capacities for the 1D array and 2D cores (from 2.79 MJm^{-3} to 10.4 MJm^{-3}), [Figure 14\(c\)](#). The energy absorbed per unit mass is also increased in the 3D core compared to the summed 1D array and 2D cores (from 5.21 J/g to 19.2 J/g), [Figure 14\(c\)](#). [Table 4](#) summarizes the energy absorption values for the individual cores examined in this aspect of the study.

4.5. Energy absorption comparisons. The energy absorbed per unit mass for the 3D structures is plotted against the peak stress and compared to a selection of aluminum foams [[Chen 2001](#); [Miyoshi et al. 2000](#); [Hall et al. 2000](#)] and the upper bound limit for axially compressed square cross section tubes of various

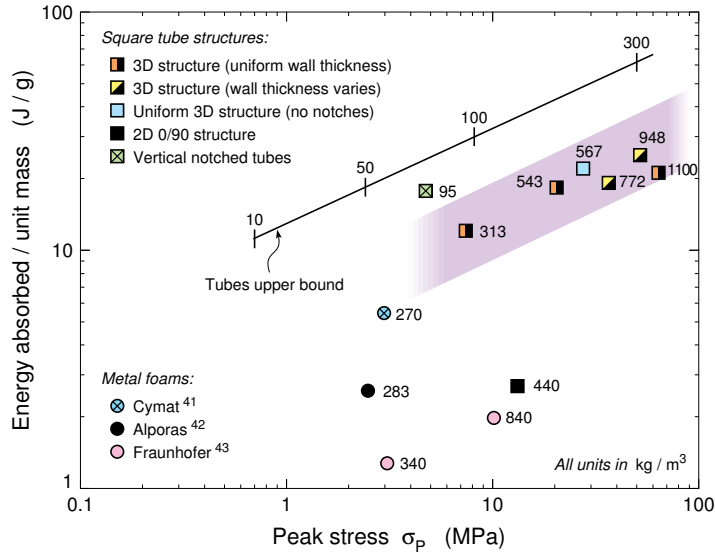


Figure 15. The energy absorbed per unit mass by the cellular structures investigated in this study compared to commercially available aluminum foams. Each cellular metal foam is labeled with its density in kg/m^3 . The wall thickness to tube width ratio is shown for the tube upper bound relation.

wall thicknesses to tube width ratios; see Figure 15.¹ The line for the upper bound absorbed energy per unit mass, E_m , has been derived (see Appendix A) from the average crush force of tubular extrusions calculated in [Hanssen et al. 2001] as

$$E_m = \sigma_p \left[\rho_s \frac{\sigma_p}{C_0 \sigma_0} \right]^{3/5} \quad (5)$$

where $\sigma_0 = 0.5(\sigma_{02} + \sigma_u)$ is the extruded tube strength, $\sigma_{02} = 278.2 \text{ MPa}$ is the nominal stress at 0.2% offset strain, $\sigma_u = 310.5 \text{ MPa}$ is the ultimate tensile stress, $\rho_s = 2700 \text{ kg}\cdot\text{m}^{-3}$ is the solid density of aluminum, and $C_0 = 1.30$ is a coefficient for square tubes. Using the measured uniaxial tensile test results for the material studied here gives, $\sigma_0 = 294.4 \text{ MPa}$. Examination of Figure 15 shows that the 3D structures outperform all metal foams and falls just below the tube upper bound curve. It should be noted that the energy absorbed per unit mass for the unnotched vertical tubes fell just under the tube upper bound in Figure 15. We also note that unlike metal foams and arrays of axially compressed tubes which resist only crushing, the 3D structure has both excellent crush and stretch resistance.

5. Finite element investigation

Finite element techniques have been used to investigate the failure mechanisms responsible for the mechanical responses of the cellular structures.

¹The energy absorption for the 3D structures and metal foams was always calculated by measuring the area under the stress-strain curve until the onset of densification (defined as the strain at which the stress reached that of the peak in crush strength).

5.1. FE model. All the finite element simulations were conducted using the explicit version of the commercial, nonlinear finite element package IMPETUS Afea Solver® [IMPETUS 2013]. The geometry and relative density of the modeled tube specimens was identical to those reported in Table 1. The initial models did not incorporate the defects in alignment and tube wall thickness seen in the experiments. The FE models were constructed using cubic hexahedral elements. A mesh sensitivity study indicated an in-plane nodal spacing approximately equal to the wall thickness (t) was sufficient to provide converged solutions. One cubic hexahedral element was therefore used through the thickness of each tube wall. The nodes of the adjacent tubes were merged prior to the simulation, thus representing a perfect braze zone with no interface failure criterion. The contact formulation in the software is based on a penalty formulation. All the simulations used rigid front face sheets constrained by the general boundary condition option of IMPETUS Afea Solver to move only in the through thickness direction while the rigid back face sheet was clamped in all directions. The simulations were conducted by applying an out-of-plane velocity-time function, $v(t)$, to the front face sheet given by

$$v(t) = \frac{w}{t_{\text{end}}} \left(1 - \cos \frac{360t}{t_{\text{end}}} \right) \quad (6)$$

where w is the crushing displacement of the sample (6 cm) and t_{end} is the end time for the loading (1 ms), which results in a maximum initial displacement rate of 6 m/s.

5.2. Material properties. The experimentally recovered Cauchy stress-true strain response of the 6061-T6 alloy undergoing uniaxial tensile testing was presented in Figure 7. The Cauchy stress, σ_c , versus true strain, ϵ , relation for an elastic-plastic material under uniaxial straining can be written as

$$\epsilon = \epsilon_e + \epsilon_p = \frac{\sigma_c}{E} + \epsilon_p \quad (7)$$

where ϵ_e and ϵ_p are the elastic and plastic components of strain and E is Young's modulus. Having performed the uniaxial tensile test shown by Figure 7, the true stress vs. plastic strain curve was tabulated. From the true stress versus plastic strain curve, the hardening curve used for all FE simulations was extracted, and the true stress at 230.7 MPa was calibrated to zero plastic strain for the isotropic hardening assumption. This hardening tabulation was applied in IMPETUS Afea Solver using the general piecewise linear constitutive model prescription given by

$$\sigma_y = f(\epsilon_{\text{eff}}^P) \left(1 - \left(\frac{T - T_0}{T_m - T_0} \right)^m \right) \left(1 + \frac{\dot{\epsilon}_{\text{eff}}^P}{\epsilon_0} \right)^c \quad (8)$$

The piecewise linear hardening constitutive model option for IMPETUS-Afea Solver defined by Equation (8) includes thermal softening and strain rate hardening parts; however, these gave negligible contributions to the response and so for all tests, the yield stress was only defined by $f(\epsilon_{\text{eff}}^P)$, a piecewise linear function of the effective deviatoric strain, which was obtained from the hardening behavior. The 6061-T6 alloys constitutive response was modeled using a multiaxial von Mises yield criterion assuming isotropic hardening. The solid density $\rho_s = 2700 \text{ kg}\cdot\text{m}^{-3}$, Young's modulus $E = 70.5 \text{ GPa}$, and Poisson ratio $\nu = 0.3$. Using the material model described above, a uniaxial tensile test was simulated and compared to the measured Cauchy stress-logarithmic strain curve in Figure 7. The fit was good and these material properties were then used for all further simulations.

To account for softening created by tube wall fracture on the tensile side of severe buckles, the Cockcroft–Latham failure criterion [Cockcroft and Latham 1968] was implemented for all the compression simulations. This failure criterion is defined by a damage parameter, $D = 1$, calculated as

$$D = \frac{1}{W_c} \int_0^{\epsilon_{\text{eff}}^P} \max(0, \sigma_1) d\epsilon_{\text{eff}}^P \quad (9)$$

where σ_1 is the first principle stress. The critical damage parameter, $W_c = 85$ MPa was obtained by fitting the simulated measured stress-strain response of a single tube lateral compression test (Appendix B). The general node splitting feature in the IMPETUS code was turned on with the damage card and enabled failed nodes to split.

The 3D tube structure models were each built from 3,106 cubic hexahedra elements with 107,348 nodes. The wall thicknesses were homogenous throughout the meshed structures and their dimensions were set to match the 3D topologies in Table 1 with $\bar{\rho} = 11.6\%$, $\bar{\rho} = 20.1\%$, $\bar{\rho} = 28.6\%$, $\bar{\rho} = 35.1\%$, and $\bar{\rho} = 42.7\%$. The perfectly aligned models gave much higher strengths than those seen in the experiments and so imperfections to the geometry of the FE models were introduced to trip buckling and provide a better fit to the measured stress-strain curves. The imperfections were modeled as a displacement of the lowest order measured eigenmode. The eigenmode amplitudes were altered by collecting all the internal tube wall faces with the general IMPETUS command used to define a surface from a seed node, and then pressurizing the 3D profiles from their inside walls using the general load pressure option of IMPETUS Afea Solver.

5.3. Simulation results. The simulated stress-strain curves are compared to the measured stress-strain compressive curves in Figures 12 and 13. First order eigenmode amplitudes of 2, 1.5, 2.6, 1.4 and 1.4 times the tube wall thickness were employed to trip buckling for the 11.6%, 20.1%, 28.6%, 35.1% and 42.7% relative density structures, respectively. These imperfection amplitudes are consistent with: (1) the significant misalignment of the 2D tubes at the boundary regions, (2) variations of tube wall thickness throughout the cellular structure, and (3) other random alignment errors as a result of tube slippage during dip brazing preparation. The laterally compressed tube simulations shown in Appendix B indicate that by alleviating these fabrication errors the need for large eigenmode amplitude imperfections can be avoided.

The collapse modes for each of the relative density samples are shown by Figure 16. The large initial eigenmode amplitudes are apparent in the early stages of strain, Figure 16(a)(i), (b)(i), and (c)(i). The strains in Figure 16 correspond to those shown in Figure 11, which also provide support for the large eigenmode imperfections introduced to the FE simulations. The buckling phenomenon observed during experiments (where the initial stress peak is controlled by through thickness tube buckling into a series of folds that initiate at the top of the tubes) is clearly observed in the simulations. Figure 17, for the 20.1% relative density structure, shows the buckling modes of the through thickness tubes in more detail by hiding two colinear tubes that block their view in Figure 16. In regions where the vertical tubes are not confined by the colinear tubes, the vertical tube walls buckle into the cavity spaces with a first order eigenmode in Figure 17(a). The notches at each through thickness layer nucleate the buckling of the through thickness tubes due to material failure (node splitting), shown in detail by Figure 18 (green tube at a strain of 3.7%). Figure 17(b) and (c) show that the vertical tubes buckle most intensely in the bottom

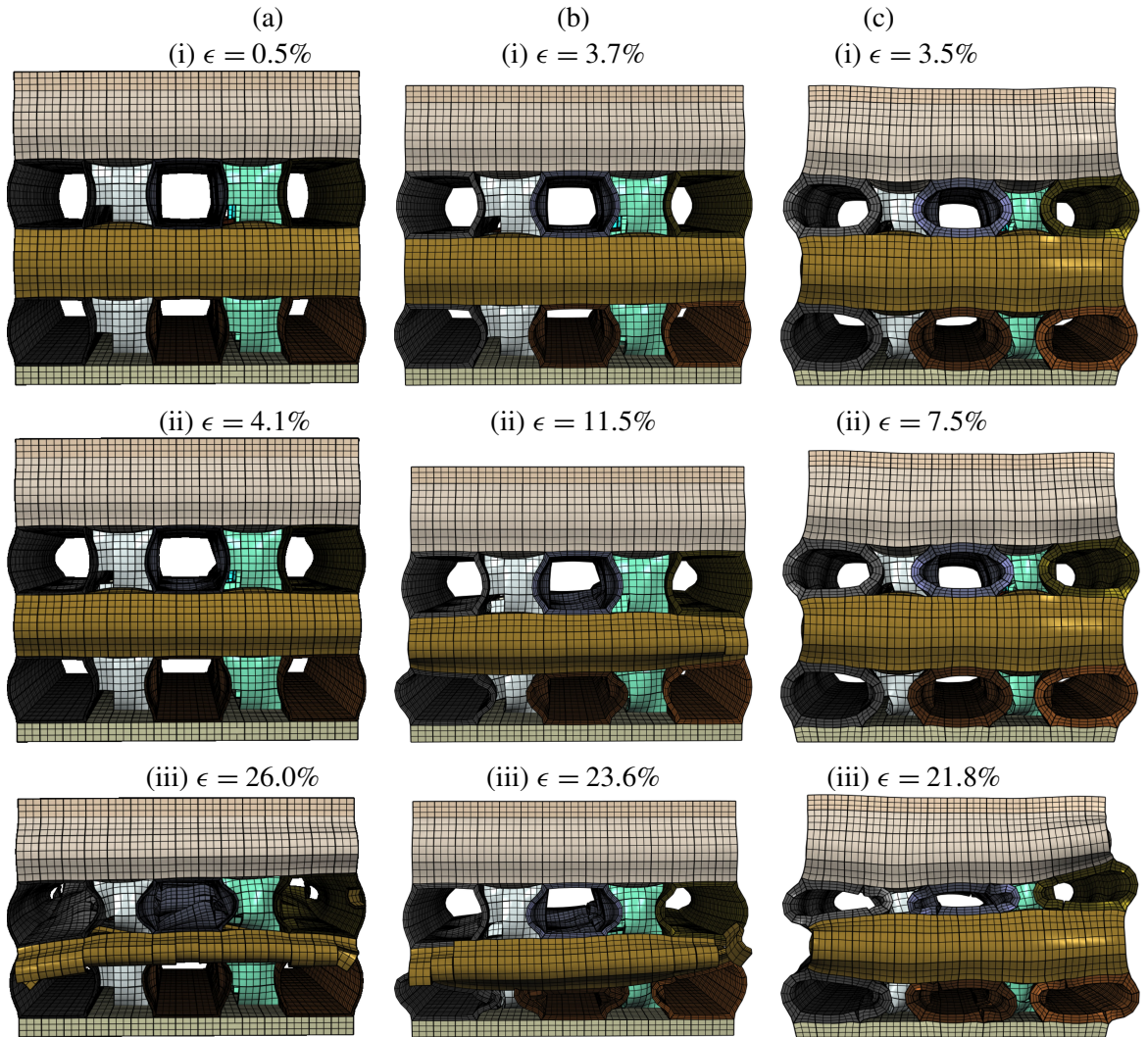


Figure 16. Images of the simulated collapse modes for 3D cellular structures with relative densities of (a) 11.6%, (b) 20.1%, and (c) 42.7%. The strain sequence corresponds to that of [Figure 11](#). The colors are used only to aid visualization of the deformations of each tube.

two layers of the structure, causing densification at this location first. As the vertical walls fold into the cavity spaces, the folds aid in crushing the colinear tubes below the folds.

The collapse modes in the void spaces (plane A in [Figure 18\(a\)](#)) can be seen in [Figure 18\(b\)](#), where all the walls buckle uniformly towards the void center as a result of reduced confinement. However, when all tube walls are brazed together at plane B ([Figure 18a](#)), nonuniform buckling of the colinear tubes side wall occurs on the side connected to the notch as a result of the notch collapse, [Figure 18\(c\)](#). The side of the colinear tube opposite the notch has a uniform collapse, but its first order eigenmode amplitude is less

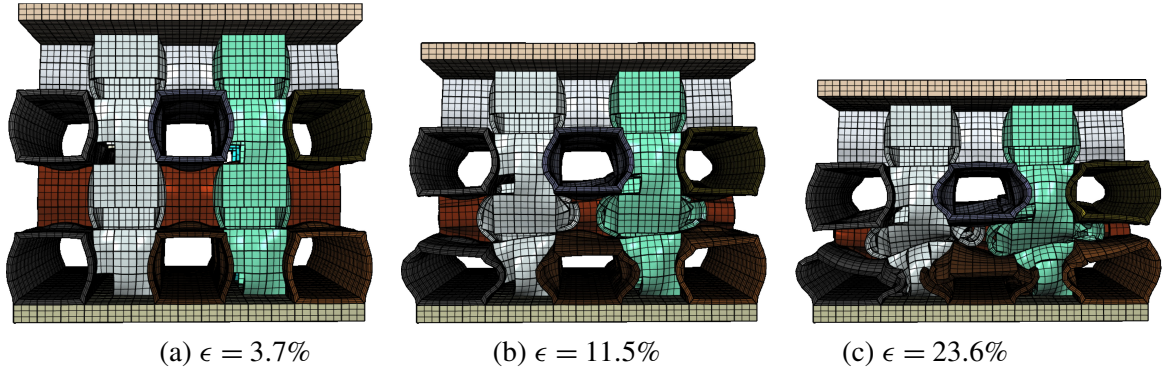


Figure 17. Images of the simulated collapse modes for 3D cellular structures with a relative density of 20.1%. Two colinear tubes have been hidden to show the collapse mode of the axial aligned tubes more clearly. The colors are used to improve visualization of the core deformations.

than the colinear tube that is not contained by the vertical tube, due to increased mass. In addition, the simulated densification strains exhibit a polynomial relationship upon relative density, by Equation (6).

The strength, modulus, and energy absorption of cellular foams was shown by Maiti et al. [1984], to be controlled by the relative density of the structure. This could be altered here by varying the tube wall thicknesses. Figure 19 shows that for relative densities between 11 and 42% the measured and predicted modulus of the 3D structures, E_{cell} scaled by that of the aluminum alloy, E_s , has a linear dependence upon relative density

$$E_{\text{cell}}/E_s = 3.6\bar{\rho}. \quad (10)$$

This is consistent with an initially stretch-dominated response [Hanssen et al. 1999]. The modulus of 3D orthogonal tube structures studied here is significantly higher than that of bending governed metal foams of similar relative density and material.

The peak strength of the 3D structure, σ_{cell} , scaled by the strength of the alloy from which it is made, σ_s , has a power dependence upon relative density

$$\sigma_{\text{cell}}/\sigma_s = 1.05(\bar{\rho})^{5/3}. \quad (11)$$

Using an energy balance argument, Wierzbicki and Abramowicz [1983] showed that the average axial crushing stress for an array of vertical tubes scaled with relative density to the power 5/3. This seems to agree well with both the experimental data and FE predictions presented here for the 3D structures whose response is dominated by the vertical tubes. We note that the 2D structure (which contains no vertical tubes aligned with the loading direction) deforms by transverse tube crushing and is expected to be a bending dominated system whose strength will scale with relative density to the power 3/2 like open cell foams, which are also bending dominated structures [Maiti et al. 1984].

Table 5 summarizes the energy absorption for the simulated 3D structures. A comparison of Tables 4 and 5 shows only small differences between the measured and simulated energy absorptions. The insignificant deviations demonstrate the good predictive accuracy of the simulations. However, the energy absorption efficiency showed more significant variability between measurements and simulations. This

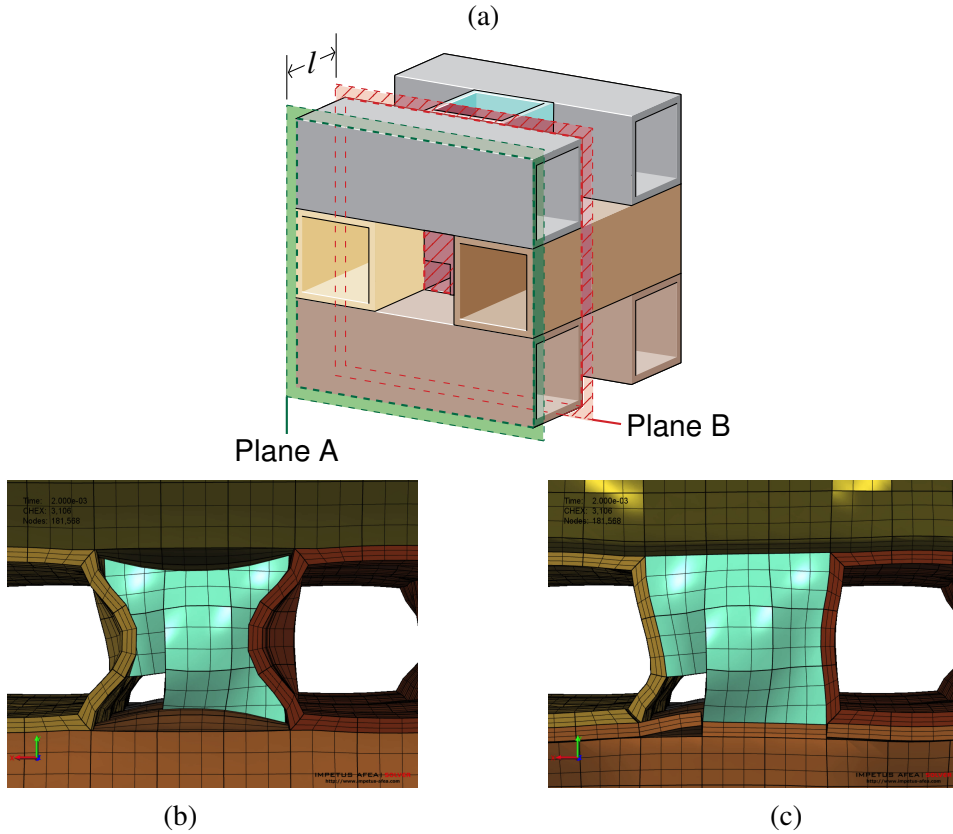


Figure 18. Simulated images of the collapse mode of a notched 3D cellular structure with a relative density of 20.1%. (a) Location of image planes. (b) In-plane tube wall buckling at Plane A. (c) Buckling on Plane B located deeper within the sample. Note the constraint imposed by the vertical tube upon the amplitude of the in-plane tube buckling mode.

Topology	Relative density, $\bar{\rho}$	Peak stress, σ_p (MPa)	ϵ_D	E_v (MJ/m ³)	E_m (J/g)	Theoretical E_m (J/g)	Energy absorbing efficiency
3D	42.7	62.0	0.49	25.7	22.3	22.7	0.97
3D	35.1	53.8	0.45	21.0	22.1	23.1	0.95
3D	28.6	36.0	0.47	15.7	20.3	20.6	0.98
3D	20.1	20.7	0.64	10.9	20.3	23.6	0.85
3D	11.6	7.3	0.70	3.5	11.2	16.4	0.68

Table 5. Energy absorption values for simulated 3D structures.

arose because of the *product* of the simulated densification strain and peak strength was less accurately estimated.

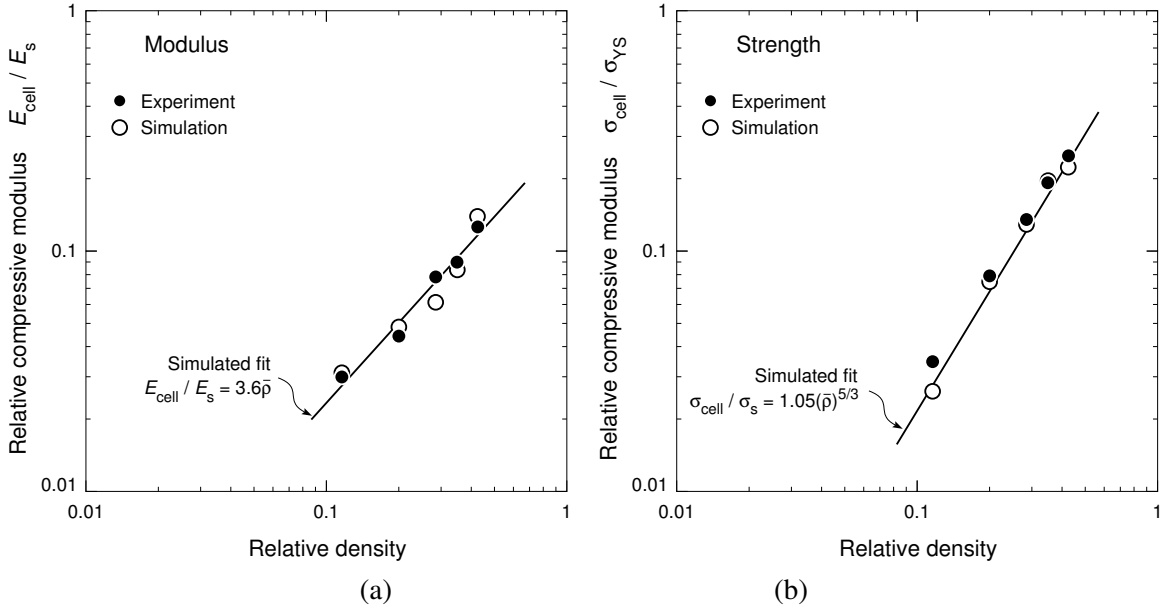


Figure 19. Dependence of (a) compressive modulus and (b) compressive strength upon relative density. Empirical fits to the data are also shown.

6. Summary

Three-dimensional orthogonal tube cellular structures for impact mitigation applications have been manufactured by dip brazing square extruded tubes made of aluminum alloy 6061 and heat treating the structure to the peak aged condition. The 3D structures material is orthotropic and the out-of-plane compressive response of structures with relative densities between 10 and 40% was measured and numerically simulated to investigate the mechanisms of plastic collapse and mechanical energy storage. We find that:

- (1) The elastic modulus has an approximately linear dependence on relative density, given by $E_{\text{cell}}/E_s = 3.6\bar{\rho}$, consistent with an initially stretch dominated response. The modulus of 3D orthogonal tube structures is significantly higher than metal foams of similar relative density and material.
- (2) The peak strength exhibits a power law dependence upon relative density, given by $\sigma_{\text{cell}}/\sigma_s = 1.05(\bar{\rho})^{5/3}$. In-situ experimental observations and finite element simulations reveal the crush strength to be controlled by buckling of tubes oriented in the applied load direction.
- (3) The specific energy absorption increased with compressive strength from about 10 kJ/kg at a compressive strength of about 10 MPa to 30 kJ/kg at strengths of about 60 MPa. This was slightly less than the specific strength of arrays of vertical tubes, but this was off-set by the existence of a nonzero in-plane compressive strength. In addition, the colinear aligned tubes should provide the structure with good stretch resistance, which is equally important for impact applications.

Appendix A. Tube upper bound derivation

The axial crushing of both square [Hanssen et al. 1999] and circular [Hanssen et al. 2000b] tubes has been widely studied. The expression for the average crush force for a hollow extrusion is given by the design formula [Jones 1989]

$$F_{\text{avg}}^0 = C_0 \phi^{2/3} \sigma_0 A_s. \quad (12)$$

The parameters involved are:

C_0 : cross section dependent dimensionless constant.

$\phi = A_s/A_f$: solidity ratio, where A_s is the solid (net) extrusion cross section and A_f the gross cross section area.

$\sigma_0 = 0.5(\sigma_{02} + \sigma_u)$: characteristic stress of extrusion material, where σ_{02} is the nominal stress at 0.2% plastic strain, and σ_u is the ultimate nominal stress.

The compressive peak stress for a crushed extruded tube is described as the average crush force over the tubes gross cross sectional area. Starting from Equation (12), the compressive peak stress is defined by

$$\sigma_p = \frac{F_{\text{avg}}^0}{A_f} = C_0 \phi^{5/3} \sigma_0. \quad (13)$$

Parameters in Equation (13) can be organized to redefine ϕ , with measurable values, as

$$\phi = \left(\frac{\sigma_p}{C_0 \sigma_0} \right)^{3/5}. \quad (14)$$

The energy absorbed (E) by the crushed extruded tube is dependent on the average crush force and the tubes axial displacement (w), and is written as

$$E = F_{\text{avg}}^0 w. \quad (15)$$

This energy absorbed per unit crush mass (E_m) is described by

$$E_m = \frac{F_{\text{avg}}^0 w}{\rho_s A_s w} = \frac{F_{\text{avg}}^0}{\rho_s A_s} \quad (16)$$

where ρ_s is the density of the tube material. The ratio for the tube energy absorbed per unit mass, Equation (16), over the tube peak stress, Equation (13), is expressed by

$$\frac{E_m}{\sigma_p} = \frac{F_{\text{avg}}^0 / (\rho_s A_s)}{F_{\text{avg}}^0 / A_f} = \frac{A_f}{\rho_s A_s} = \frac{1}{\rho_s \phi}. \quad (17)$$

Rearranging (17) to define the tube energy absorbed per unit mass (E_m) with respect to the tube peak stress (σ_p) and substituting ϕ with (14) results in the expression used to graphically obtain the tube upper limit shown in Figure 15 as

$$E_m = \frac{\sigma_p}{\rho_s \phi} = \sigma_p \left(\rho_s \frac{\sigma_p}{C_0 \sigma_0} \right)^{3/5}. \quad (18)$$

	Measured	Numerical model
Top wall thickness (mm)	1.59	1.575
Right wall thickness (mm)	1.57	1.575
Left wall thickness (mm)	1.58	1.575
Bottom wall thickness (mm)	1.58	1.575
Right to left wall outer width (mm)	18.99	19.05
Top to bottom wall outer width (mm)	18.95	19.05
Relative density, $\bar{\rho}$	28.74	30.34
Peak stress, σ_p (MPa)	48.83	49.15

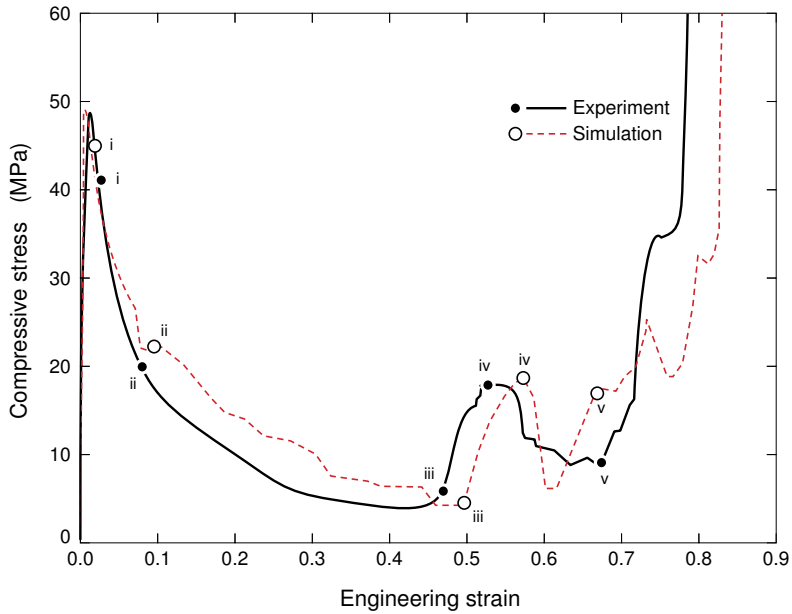
Table 6. Measured dimensions of single tube profile sample studied under quasistatic compressive lateral loading.

Appendix B. Lateral compression of a single tube

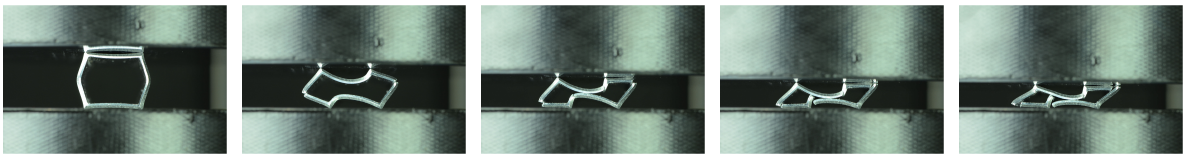
To test the validity of the modeling approach prior to simulating quasistatic compression of the 3D topologies we set up a simple single square tube compression experiment and compared the measured and simulated response using the material model described above. We also tuned the critical damage parameter (W_c) with this simulation to 85 MPa, which was applied to all 3D simulations to initiate node splitting.

The dimensions of the measured and modeled tube are outlined in [Table 6](#). The tested tube underwent the same thermal processes as outlined in [Section 2.2](#), rendering an age-hardened AA 6061-T6 tube. The Specimen was compressed in a 50 kN Instron universal testing machine (Instron Corporation, Model 4208, Canton, MA, USA) at a strain rate of $\dot{\epsilon} = 4 \times 10^{-3} \text{ s}^{-1}$ and temperature of 25°C. A laser extensometer (Electronic Instrument Research, Model LE-01, Irwin, PA, USA) was used to measure the displacement of the tube walls. It should be noted that the tube was not brazed to a face sheet material like the 3D orthogonal tube samples in the study. Instead, the tube walls directly contacted the load platens, which resulted in a different collapse mode to that of tubes that were brazed to face sheets.

The meshed tube structure was built from 3,240 cubic hexahedra elements with 112,112 nodes. The simulated stress-strain curve in [Figure 19](#) demonstrates a good fit to the measured sample. A comparison of [Figure 20\(b\)](#) and (c) shows near identical collapse mode predictions for the experimental and simulated single tube profiles. Thus, the material properties were deemed satisfactory for the 3D orthogonal tube assemblies. Besides providing verification of the material approach, this model also provided evidence of the sensitivity between tube wall thickness and predicting the force curves. No imperfections were necessary with a single tube since the wall thickness of the numerical models fell within 1% or less of each other. This observation suggests that there was a combination of 1) variability in the thickness of each tube that formed the 3D structure and 2) the misalignment caused by fabrication resulted in the large imperfections that were required to trip the simulated 3D structures buckling.



(a)



(i)

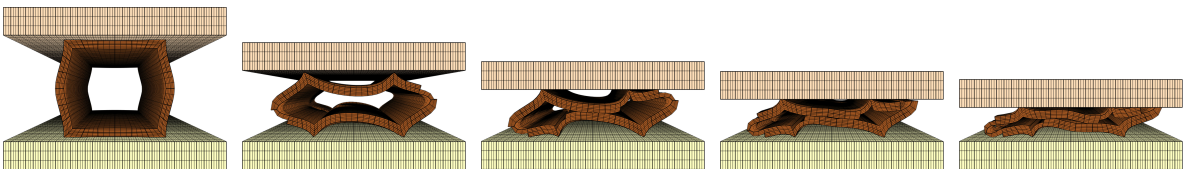
(ii)

(iii)

(iv)

(v)

(b)



(i)

(ii)

(iii)

(iv)

(v)

(c)

Figure 20. (a) A stress-strain curve for a single tube under lateral compression. (b) The experimentally observed sequence of the tested collapse modes. (c) The sequence of simulated collapse modes.

Acknowledgements

The authors are grateful to the U.S. Office of Naval Research (ONR grant number N00014-07-1-0764) for financial support of this research.

References

- [Allen 1969] H. G. Allen, *Analysis and design of structural sandwich panels*, Pergamon, Oxford, 1969.
- [ASM 2003] *Brazing of aluminum alloys*, pp. 627–1067, ASM International, Materials Park, OH, 2003.
- [Baumeister et al. 1997] J. Baumeister, J. Banhart, and M. Weber, “Aluminium foams for transport industry”, *Mater. Des.* **18**:4-6 (1997), 217–220.
- [Bitzer 1997] T. Bitzer, *Honeycomb technology*, Chapman and Hall, London, 1997.
- [Braithwaite 2008] D. Braithwaite, 2008, <http://www.colemanmw.com>. Personal communication.
- [Chakrabarti and Laughlin 2004] D. J. Chakrabarti and D. E. Laughlin, “Phase relations and precipitation in Al-Mg-Si alloys with Cu additions”, *Prog. Mater. Sci.* **49**:3-4 (2004), 389–410.
- [Chen 2001] W. Chen, “Experimental and numerical study on bending collapse of aluminum foam-filled hat profiles”, *Int. J. Solids Struct.* **38**:44-45 (2001), 7919–7944.
- [Cockcroft and Latham 1968] M. G. Cockcroft and D. J. Latham, “Ductility and workability of metals”, *J. Inst. Met.* **96** (1968), 33–39.
- [Dharmasena et al. 2008] K. P. Dharmasena, H. N. G. Wadley, Z. Xue, and J. W. Hutchinson, “Mechanical response of metallic honeycomb sandwich panel structures to high intensity dynamic loading”, *Int. J. Impact Eng.* **35** (2008), 1063–1074.
- [Elzey and Wadley 2001] D. M. Elzey and H. N. G. Wadley, “The limits of solid state foaming”, *Acta Mater.* **49** (2001), 849–859.
- [Evans et al. 2001] A. G. Evans, J. W. Hutchinson, N. A. Fleck, M. F. Ashby, and H. N. G. Wadley, “The topological design of multifunctional cellular metals”, *Prog. Mater. Sci.* **46** (2001), 309–327.
- [Finnegan et al. 2007] K. Finnegan, G. Kooistra, H. N. G. Wadley, and V. S. Deshpande, “The compressive response of carbon fiber composite pyramidal truss sandwich cores”, *Int. J. Mater. Res.* **12** (2007), 1264–1272.
- [Fleming et al. 2012] K. Fleming, A. Zhu, and J. Scully, “Corrosion of AA6061 brazed with an Al-Si alloy: effects of Si on metallurgical and corrosion behavior”, *Corros. J. Sci. Eng.* **68**:12 (2012), 1126–1145.
- [Gibson and Ashby 1988] L. J. Gibson and M. F. Ashby, *Cellular solids: structure and properties*, Pergamon, Oxford, 1988.
- [Gibson and Ashby 1997] L. J. Gibson and M. F. Ashby, *Cellular solids: structure and properties*, 2nd ed., Cambridge University Press, Cambridge, 1997.
- [Hall et al. 2000] I. W. Hall, M. Guden, and C.-J. Yu, “Crushing of aluminum closed cell foams: density and strain rate effects”, *Scr. Mater.* **43** (2000), 515–521.
- [Hanssen et al. 1999] A. G. Hanssen, M. Langseth, and O. S. Hopperstad, “Static crushing of square aluminium extrusions with aluminium foam filler”, *Int. J. Mech. Sci.* **41** (1999), 967–993.
- [Hanssen et al. 2000a] A. G. Hanssen, M. Langseth, and O. S. Hopperstad, “Static and dynamic crushing of square aluminium extrusions with aluminium foam filler”, *Int. J. Impact Eng.* **24**:4 (2000), 347–383.
- [Hanssen et al. 2000b] A. G. Hanssen, M. Langseth, and O. S. Hopperstad, “Static and dynamic crushing of circular aluminium extrusions with aluminium foam filler”, *Int. J. Impact Eng.* **24**:5 (2000), 475–507.
- [Hanssen et al. 2001] A. G. Hanssen, O. S. Hopperstad, and M. Langseth, “Design of aluminium foam-filled crash boxes with square and circular cross sections”, *Int. J. Crashworthiness* **6**:2 (2001), 177–188.
- [Hatch 1984] J. E. Hatch (editor), *Aluminum: properties and physical metallurgy*, pp. 226–293, American Society for Metals, Metals Park, OH, 1984.
- [Hutchinson and Xue 2005] J. W. Hutchinson and Z. Y. Xue, “Metal sandwich plates optimized for pressure impulses”, *Int. J. Mech. Sci.* **47**:4-5 (2005), 545–556.
- [IMPETUS 2013] IMPETUS, “IMPETUS Afea Solver®”, 2013, <http://www.impetus-afea.com>.
- [Jones 1989] N. Jones, *Structural impact*, Cambridge University Press, Cambridge, 1989. 2nd ed. in 2012.
- [Kooistra et al. 2004] G. W. Kooistra, V. S. Deshpande, and H. N. G. Wadley, “Compressive behavior of age hardenable tetrahedral lattice truss structures made from aluminium”, *Acta Mater.* **52**:14 (2004), 4299–4237.

- [Kooistra et al. 2008] G. W. Kooistra, D. T. Queheillalt, and H. N. G. Wadley, “Shear behavior of aluminum lattice truss sandwich panel structures”, *Mater. Sci. Eng. A* **472** (2008), 242–250.
- [Laurin and Vizzini 2005] F. Laurin and A. J. Vizzini, “Energy absorption of sandwich panels with composite-reinforced foam core”, *J. Sandw. Struct. Mater.* **7** (2005), 113–132.
- [Liang et al. 2007] Y. Liang, A. V. Spuskanyuk, S. E. Flores, D. R. Hayhurst, J. W. Hutchinson, R. M. McMeeking, and A. G. Evans, “The response of metallic sandwich panels to water blast”, *J. Appl. Mech. (ASME)* **74** (2007), 81–99.
- [Maiti et al. 1984] S. K. Maiti, L. J. Gibson, and M. F. Ashby, “Deformation and energy absorption diagrams for cellular solids”, *Acta Metall.* **32**:11 (1984), 1963–1975.
- [McShane et al. 2007] G. J. McShane, D. D. Radford, V. S. Deshpande, and N. A. Fleck, “The dynamic compressive response of square-honeycombs”, *J. Appl. Mech. (ASME)* **74** (2007), 658–667.
- [Mills 2007] N. J. Mills, “Polyurethane foams: processing and microstructure”, Chapter 2, pp. 19–37 in *Polymer foams handbook: engineering and biomechanics applications and design guide*, Butterworth-Heinemann, Amsterdam, 2007.
- [Miyoshi et al. 2000] T. Miyoshi, M. Itah, S. Akiyama, and A. Kitahara, “ALPORAS aluminum foam: production process, properties, and applications”, *Adv. Eng. Mater.* **2**:4 (2000), 179–183.
- [Moongkhamklang and Wadley 2010] P. Moongkhamklang and H. N. G. Wadley, “Titanium alloy lattice structures with millimeter scale cell sizes”, *Adv. Eng. Mater.* **12**:11 (2010), 1111–1116.
- [Queheillalt et al. 2000] D. T. Queheillalt, B. W. Choi, H. N. G. Wadley, and D. S. Schwartz, “Creep expansion of porous Ti-6Al-4V sandwich structures”, *Metall. Trans. A* **31** (2000), 261–273.
- [Queheillalt et al. 2008] D. T. Queheillalt, Y. Murty, and H. N. G. Wadley, “Mechanical properties of an extruded pyramidal lattice truss sandwich structure”, *Scr. Mater.* **58**:1 (2008), 76–79.
- [Reid 1993] S. R. Reid, “Plastic deformation mechanisms in axially compressed metal tubes used as impact energy absorbers”, *Int. J. Mech. Sci.* **35**:12 (1993), 1035–1052.
- [Reyes 2008] G. Reyes, “Static and low velocity impact behavior of composite sandwich panels with an aluminum foam core”, *J. Compos. Mater.* **42**:16 (2008), 1659–1670.
- [Rimoli et al. 2011] J. J. Rimoli, B. Talamini, J. J. Wetzel, K. P. Dharmasena, R. Radovitzky, and H. N. G. Wadley, “Wet-sand impulse loading of metallic plates and corrugated core sandwich panels”, *Int. J. Impact Eng.* **38** (2011), 837–848.
- [Russell et al. 2008] B. Russell, V. S. Deshpande, and H. N. G. Wadley, “Quasistatic deformation and failure modes of composite square honeycombs”, *J. Mech. Mater. Struct.* **3**:7 (2008), 1315–1340.
- [Tian et al. 2007] J. Tian, T. J. Lu, H. P. Hodson, D. T. Queheillalt, and H. N. G. Wadley, “Cross flow heat exchange of textile cellular metal core sandwich panels”, *Int. J. Heat Mass Transf.* **50** (2007), 2521–2536.
- [Tilbrook et al. 2006] M. T. Tilbrook, V. S. Deshpande, and N. A. Fleck, “The impulsive response of sandwich beams: analytical and numerical investigation of regimes of behavior”, *J. Mech. Phys. Solids* **54** (2006), 2242–2280.
- [Vaziri et al. 2007] A. Vaziri, Z. Xue, and J. W. Hutchinson, “Performance and failure of metal sandwich plates subjected to shock loading”, *J. Mech. Mater. Struct.* **2**:10 (2007), 1947–1963.
- [Vinson 2001] J. R. Vinson, “Sandwich structures”, *Appl. Mech. Rev. (ASME)* **54**:3 (2001), 201–214.
- [Wadley 2006] H. N. G. Wadley, “Multifunctional periodic cellular metals”, *Phil. Trans. R. Soc. A* **364**:1838 (2006), 31–68.
- [Wadley et al. 2007] H. N. G. Wadley, K. P. Dharmasena, D. T. Queheillalt, Y. Chen, P. Dudt, D. Knight, K. Kiddy, Z. Xue, and A. Vaziri, “Dynamic compression of square honeycomb structures during underwater impulsive loading”, *J. Mech. Mater. Struct.* **2**:10 (2007), 2025–2048.
- [Wei et al. 2007] Z. Wei, K. P. Dharmasena, H. N. G. Wadley, and A. G. Evans, “Analysis and interpretation of a test for characterizing the response of sandwich panels to water blast”, *Int. J. Impact Eng.* **34** (2007), 1602–1618.
- [Wei et al. 2008] Z. Wei, V. S. Deshpande, A. G. Evans, K. P. Dharmasena, D. T. Queheillalt, H. N. G. Wadley, Y. Murty, R. K. Elzey, P. Dudt, Y. Chen, D. Knight, and K. Kiddy, “The resistance of metallic plates to localized impulse”, *J. Mech. Phys. Solids* **56** (2008), 2074–2091.
- [Wicks and Hutchinson 2001] N. Wicks and J. W. Hutchinson, “Optimal truss plates”, *Int. J. Solids Struct.* **38** (2001), 5165–5183.

[Wierzbicki and Abramowicz 1983] T. Wierzbicki and W. Abramowicz, “On the crushing mechanics of thin-walled structures”, *J. Appl. Mech. (ASME)* **50** (1983), 727–739.

[Xue and Hutchinson 2006] Z. Xue and J. W. Hutchinson, “Crush dynamics of square honeycomb sandwich cores”, *Int. J. Numer. Methods Eng.* **65** (2006), 2221–2245.

[Zenkert 1995] D. Zenkert, *An introduction to sandwich construction*, Chameleon, London, 1995.

Received 4 Sep 2012. Revised 19 Oct 2012. Accepted 30 Oct 2012.

RYAN L. HOLLOMAN: rlh5v@virginia.edu

Department of Materials Science and Engineering, University of Virginia, Charlottesville, VA 22903, United States

VIKRAM DESHPANDE: vsd20@cam.ac.uk

Engineering Department, University of Cambridge, Trumpington Street, Cambridge, CB2 1PZ, United Kingdom

ARVE G. HANSEN: arve@impetus.no

IMPETUS Afea AS, Strandgaten 32, N-4400 Flekkefjord, Norway

KATHERINE M. FLEMING: kmf2m@virginia.edu

Department of Materials Science and Engineering, University of Virginia, Charlottesville, VA 22903, United States

JOHN R. SCULLY: jrs8d@virginia.edu

Department of Materials Science and Engineering, University of Virginia, Charlottesville, VA 22903, United States
<http://www.virginia.edu/cese/>

HAYDN N. G. WADLEY: haydn@virginia.edu

Department of Materials Science and Engineering, University of Virginia, Charlottesville, VA 22903, United States
<http://www.ipm.virginia.edu/>

REFLECTION OF PLANE LONGITUDINAL WAVES FROM THE STRESS-FREE BOUNDARY OF A NONLOCAL, MICROPOLAR SOLID HALF-SPACE

AARTI KHURANA AND SUSHIL K. TOMAR

This work is concerned with plane waves propagating through an isotropic nonlocal micropolar solid. Two longitudinal waves and two sets of coupled transverse waves propagating with distinct speeds may travel in the medium. All these waves are found to be dispersive in nature. Reflection coefficients and energy ratios are presented for when a longitudinal displacement wave strikes at the stress-free boundary. The dispersion curves of various waves for a silicon crystal are computed numerically and depicted graphically. The effect of nonlocality on the reflection coefficients and energy ratios is observed. The energy balance law has been verified at each angle of incidence.

1. Introduction

The theory of nonlocal elasticity, developed in [Eringen 1972a; 1972b; 2002; Eringen and Edelen 1972], states that the nonlocal stress tensor at any reference point \mathbf{x} of the body depends not only on the strain at the point \mathbf{x} but also on the strains at all other points \mathbf{x}' of the body. This observation is in accordance with the atomic theory of lattice dynamics and experimental observations on phonon dispersion [Chen et al. 2004]. In the limiting case, when the effects of strains at points other than \mathbf{x} are neglected, one recovers the classical (local) theory of elasticity. The most general form of the constitutive relation in the nonlocal elasticity-type representation involves an integral over the entire region of interest. This integral contains a nonlocal kernel function, which describes the relative influence of the strains at various locations on the stress at a given location.

Polar theories, in principle, are nonlocal theories (see [Eringen 1999]) where the nonlocality is achieved through moment tensors associated with each point of the body. However, as the wavelengths of the waves transmitted become shorter, the number of moment tensors to be employed must be increased to provide sufficient accuracy in the prediction of the physical phenomena. The response of a body depends heavily on the ratio of the external characteristic length (L) to the internal characteristic length (l). In classical field theories, a ratio of $L/l \gg 1$ will yield reliable predictions. However, when $L/l \approx 1$, the classical field theories (local) fail and we must resort to nonclassical theories (nonlocal). One of the theories in which $L \approx l$ is the micropolar theory of elasticity. Some of the relevant papers on nonlocal theories are [Eringen 1984; Erbay et al. 1992; Wang and Dhaliwal 1993; Lazar and Kirchner 2006; Zeng et al. 2006; Najafi et al. 2012] among others.

In this paper, we have extended the work proposed in [Eringen 1984] by exploring the possibility of the propagation of plane elastic waves in a linear isotropic nonlocal micropolar solid. It is seen that there

Valuable suggestions provided by the anonymous reviewers are gratefully acknowledged.

Keywords: nonlocal, micropolar, reflection, frequency, elastic waves.

may exist four waves comprising of two coupled transverse waves and two independent longitudinal waves analogous to those existing in a local micropolar solid. In local micropolar elasticity, the longitudinal displacement wave is frequency independent, while the longitudinal microrotational wave and two sets of coupled transverse waves are frequency dependent. In nonlocal micropolar elasticity, all the longitudinal and transverse waves are frequency dependent. The reflection phenomena of a longitudinal displacement wave incident obliquely at a stress-free flat boundary of a nonlocal micropolar elastic half-space are investigated in detail. Reflection coefficients and their corresponding energy ratios are obtained analytically and depicted graphically for a silicon crystal against the angle of incidence. The reflection coefficients and energy ratios have been plotted for two values of the nonlocal parameter, namely $e_0 = 0$ and $e_0 = 0.39$. The parameter $e_0 = 0$ corresponds to the local micropolar medium. The sum of energy ratios is found to be unity at each angle of incidence which shows that there is no dissipation of energy during reflection at the free boundary surface of a nonlocal micropolar solid.

2. Basic equations and constitutive relations

For a linear anisotropic nonlocal micropolar solid, the strain energy density function W is given as [Eringen 2002]

$$W = \frac{1}{2} \iint \{A_{klmn}(\mathbf{x}, \mathbf{x}') \epsilon_{kl}(\mathbf{x}') \epsilon_{mn}(\mathbf{x}) + B_{klmn}(\mathbf{x}, \mathbf{x}') \gamma_{kl}(\mathbf{x}') \gamma_{mn}(\mathbf{x}) + C_{klmn}(\mathbf{x}, \mathbf{x}') (\epsilon_{kl}(\mathbf{x}') \gamma_{mn}(\mathbf{x}) + \epsilon_{kl}(\mathbf{x}) \gamma_{mn}(\mathbf{x}')\} dv(\mathbf{x}') dv(\mathbf{x}), \quad (1)$$

where $\epsilon_{kl} = u_{l,k} - \epsilon_{klm} \phi_m$ denotes the relative distortion tensor and $\gamma_{kl} = \phi_{k,l}$ is the curvature or wryness tensor. The nonlocal constitutive moduli possess the symmetries

$$A_{klmn}(\mathbf{x}, \mathbf{x}') = A_{mnlk}(\mathbf{x}', \mathbf{x}) \quad \text{and} \quad B_{klmn}(\mathbf{x}, \mathbf{x}') = B_{mnlk}(\mathbf{x}', \mathbf{x}).$$

In local micropolar elasticity, the force stress tensor ($t_{kl}(\mathbf{x})$) and couple stress tensor ($m_{kl}(\mathbf{x})$) are given in integral form by the nonlocal constitutive relations [Eringen 2002]

$$t_{kl}(\mathbf{x}) = \int \{A_{klmn}(\mathbf{x}, \mathbf{x}') \epsilon_{mn}(\mathbf{x}') + C_{klmn}(\mathbf{x}, \mathbf{x}') \gamma_{mn}(\mathbf{x}')\} dv(\mathbf{x}'), \quad (2)$$

$$m_{kl}(\mathbf{x}) = \int \{B_{klmn}(\mathbf{x}, \mathbf{x}') \gamma_{mn}(\mathbf{x}') + C_{mnlk}(\mathbf{x}, \mathbf{x}') \epsilon_{mn}(\mathbf{x}')\} dv(\mathbf{x}'). \quad (3)$$

For an isotropic micropolar solid, the nonlocal elastic moduli are [Eringen 2002]

$$A_{klmn}(\mathbf{x}, \mathbf{x}') = \lambda \delta_{kl} \delta_{mn} + (\mu + K) \delta_{km} \delta_{ln} + \mu \delta_{kn} \delta_{lm},$$

$$B_{klmn}(\mathbf{x}, \mathbf{x}') = \alpha \delta_{kl} \delta_{mn} + \gamma \delta_{km} \delta_{ln} + \beta \delta_{kn} \delta_{lm} \quad \text{and} \quad C_{klmn}(\mathbf{x}, \mathbf{x}') = 0,$$

where the material moduli λ , μ , K , α , β , and γ depend on \mathbf{x} and \mathbf{x}' through $|\mathbf{x} - \mathbf{x}'|$, that is,

$$\{\lambda, \mu, K, \alpha, \beta, \gamma\} = \{\lambda', \mu', K', \alpha', \beta', \gamma'\} G(|\mathbf{x} - \mathbf{x}'|),$$

with λ' , μ' , K' , α' , β' , and γ' as local micropolar elastic constants, of which λ' and μ' correspond to the classical Lamé constants, and $G(|\mathbf{x} - \mathbf{x}'|)$ as the nonlocal kernel. The function $G(|\mathbf{x} - \mathbf{x}'|)$ represents the effect of distant interactions of material points \mathbf{x}' on the material point \mathbf{x} . Since the long-range effects

quickly die out with distance, this function should attain its maximum at $\mathbf{x}' = \mathbf{x}$. Eringen has shown that the function G happens to be the Green's function for the infinite plane, that is, it satisfies [Eringen 1984]

$$(1 - \epsilon^2 \nabla^2)G = \delta(|\mathbf{x}' - \mathbf{x}|), \quad (4)$$

where $\epsilon = e_0 a$, a being the internal characteristic length (for example, the atomic lattice parameter in crystals, the average granular distance in granular solids, etc.), and e_0 is a material constant.

Using these expressions of the elastic moduli, the constitutive relations (2) and (3) become

$$t_{kl}(\mathbf{x}) = \int \{\lambda \delta_{kl} \epsilon_{rr}(\mathbf{x}') + (\mu + K) \epsilon_{kl}(\mathbf{x}') + \mu \epsilon_{lk}(\mathbf{x}')\} dv(\mathbf{x}'), \quad (5)$$

$$m_{kl}(\mathbf{x}) = \int \{\alpha \delta_{kl} \gamma_{rr}(\mathbf{x}') + \beta \gamma_{kl}(\mathbf{x}') + \gamma \gamma_{lk}(\mathbf{x}')\} dv(\mathbf{x}'). \quad (6)$$

The equations of motion for a nonlocal isotropic micropolar solid are given by [Eringen 2002]

$$t_{kl,k} + \rho(f_l - \ddot{u}_l) = 0, \quad (7)$$

$$m_{kl,k} + \epsilon_{lmn} t_{mn} + \rho(l_l - j \ddot{\phi}_l) = 0. \quad (8)$$

Applying the operator $(1 - \epsilon^2 \nabla^2)$ to (5) and (6) and using the property (4) together with

$$\int f(x) \delta(x - a) dx = f(a), \quad (9)$$

we obtain

$$(1 - \epsilon^2 \nabla^2) t_{kl} = \sigma_{kl} = \lambda' \delta_{kl} \epsilon_{rr}(\mathbf{x}) + (\mu' + K') \epsilon_{kl}(\mathbf{x}) + \mu' \epsilon_{lk}(\mathbf{x}), \quad (10)$$

$$(1 - \epsilon^2 \nabla^2) m_{kl} = \mu_{kl} = \alpha' \delta_{kl} \gamma_{rr}(\mathbf{x}) + \beta' \gamma_{kl}(\mathbf{x}) + \gamma' \gamma_{lk}(\mathbf{x}). \quad (11)$$

We can see from the expressions of the above equations that σ_{kl} and μ_{kl} are the force stress and couple stress tensors of local micropolar elasticity.

Now, using (10) and (11) in the field equations (7) and (8), we obtain

$$(\lambda' + \mu') u_{k,kl} + (\mu' + K') u_{l,kk} + K' \epsilon_{klm} \phi_{k,m} + (1 - \epsilon^2 \nabla^2) \rho(f_l - \ddot{u}_l) = 0, \quad (12)$$

$$(\alpha' + \beta') \phi_{k,kl} + \gamma' \phi_{l,kk} + K' \epsilon_{lmn} u_{n,m} - 2K' \phi_l + (1 - \epsilon^2 \nabla^2) \rho(l_l - j \ddot{\phi}_l) = 0. \quad (13)$$

These are the equations of small motion in a nonlocal micropolar elastic medium. It is clear that in the absence of nonlocality, that is, when $e_0 = 0$, these equations reduce to the well-known equations of a uniform micropolar solid. Since $\epsilon = e_0 a$, the parameter ϵ may be called the nonlocal parameter.

3. Wave propagation

Introducing the scalar potentials (q, ξ) and vector potentials $(\mathbf{U}, \mathbf{\Pi})$ through the Helmholtz decomposition theorem as

$$\mathbf{u} = \nabla q + \nabla \times \mathbf{U}, \quad \boldsymbol{\phi} = \nabla \xi + \nabla \times \mathbf{\Pi}; \quad \nabla \cdot \mathbf{U} = \nabla \cdot \mathbf{\Pi} = 0, \quad (14)$$

and plugging them into (12) and (13), we obtain the following equations of motion, in the absence of body forces and body couples:

$$(\lambda' + 2\mu' + K')\nabla^2 q - \rho(1 - \epsilon^2\nabla^2)\ddot{q} = 0, \quad (15)$$

$$(\mu' + K')\nabla^2 \mathbf{U} + K'\nabla \times \mathbf{\Pi} - \rho(1 - \epsilon^2\nabla^2)\ddot{\mathbf{U}} = \mathbf{0}, \quad (16)$$

$$(\alpha' + \beta' + \gamma')\nabla^2 \xi - 2K'\xi - \rho j(1 - \epsilon^2\nabla^2)\ddot{\xi} = 0, \quad (17)$$

$$\gamma'\nabla^2 \mathbf{\Pi} + K'\nabla \times \mathbf{U} - 2K'\mathbf{\Pi} - \rho j(1 - \epsilon^2\nabla^2)\ddot{\mathbf{\Pi}} = \mathbf{0}. \quad (18)$$

It can be seen that (16) and (18) are coupled in vector potentials \mathbf{U} and $\mathbf{\Pi}$ and (15) and (17) are independent in scalar potentials q and ξ . It is also noted that in the absence of nonlocality, that is, when $\epsilon = 0$, (15)–(18) reduce completely to the wave equations of a linear micropolar solid.

For plane waves propagating in the positive direction of a unit vector \mathbf{n} , we have

$$\{q, \xi, \mathbf{U}, \mathbf{\Pi}\} = \{a, b, \mathbf{A}, \mathbf{B}\} \exp\{ik(\mathbf{n} \cdot \mathbf{r} - Vt)\}, \quad (19)$$

where a and b are scalar constants, \mathbf{A} and \mathbf{B} are vector constants, and V is the phase speed. The circular frequency ω is defined by $\omega = kV$, k being the wavenumber. Inserting the expression of q from (19) into (15), we obtain

$$V_1^2 = (\lambda' + 2\mu' + K')\rho^{-1} - \epsilon^2\omega^2. \quad (20)$$

This is the speed of the longitudinal displacement wave representing the longitudinal acoustic branch. We see that the speed of the longitudinal displacement wave in the nonlocal micropolar solid is equal to the speed of the longitudinal wave in the local micropolar solid decreased by an amount $\epsilon^2\omega^2$. Next, inserting the expression of ξ from (19) into (17), we obtain

$$V_2^2 = \left(\frac{\alpha' + \beta' + \gamma'}{\rho j} - \epsilon^2\omega^2\right) \left(1 - \frac{2K'}{\rho j\omega^2}\right)^{-1}. \quad (21)$$

This is the speed of the longitudinal microrotational wave representing the longitudinal optic branch. Similarly, inserting the expressions of \mathbf{U} and $\mathbf{\Pi}$ from (19) into (16) and (18), we obtain

$$\mathbf{A}\{(\mu' + K')k^2 - \rho\omega^2 - \rho\omega^2\epsilon^2k^2\} - ikK'\mathbf{n} \times \mathbf{B} = \mathbf{0}, \quad (22)$$

$$ikK'\mathbf{n} \times \mathbf{A} - \mathbf{B}\{k^2\gamma' + 2K' - \rho j\omega^2 - \rho j\omega^2\epsilon^2k^2\} = \mathbf{0}. \quad (23)$$

Elimination of \mathbf{A} or \mathbf{B} from (22) and (23) yields a quadratic equation in V^2 given by

$$AV^4 + BV^2 + C = 0. \quad (24)$$

The roots of this equation are given by

$$V_3^2 = \frac{1}{2A}(-B + \sqrt{B^2 - 4AC}), \quad V_4^2 = \frac{1}{2A}(-B - \sqrt{B^2 - 4AC}), \quad (25)$$

where

$$A = 1 - \Omega, \quad B = \omega^2\epsilon^2 - c_4^2 - \frac{1}{2}c_3^2\Omega + (1 - \Omega)(\omega^2\epsilon^2 - c_2^2 - c_3^2), \quad C = (\omega^2\epsilon^2 - c_2^2 - c_3^2)(\omega^2\epsilon^2 - c_4^2),$$

$$\Omega = \frac{2\omega_0^2}{\omega^2}, \quad \omega_0^2 = \frac{K'}{\rho j}, \quad c_2^2 = \frac{\mu'}{\rho}, \quad c_3^2 = \frac{K'}{\rho}, \quad c_4^2 = \frac{\gamma'}{\rho j}.$$

When $\epsilon = 0$, the expressions of the coefficients A , B , and C exactly match with those obtained in [Parfitt and Eringen 1969] for micropolar elasticity. These authors showed:

- (i) For $A > 0$, and keeping in mind the restrictions imposed on elastic moduli, the quantity B is always negative and the quantity C is always positive. Thus, the discriminant is $B^2 - 4AC > 0$ and hence the value of V_3^2 is finite and positive.
- (ii) For $A < 0$, the quantity $B^2 - 4AC$ is finite and positive, since C is already a positive quantity. Also, $\sqrt{B^2 - 4AC} > |-B|$, which makes the value of V_3^2 negative. This shows that $V_3^2 < 0$ or > 0 for $A < 0$ or > 0 , respectively.
- (iii) V_4^2 is a finite and positive quantity for $A > 0$ as well as for $A < 0$. Thus, a wave propagating with phase speed V_4 exists for all values of ω .

In the present case, that is, when $\epsilon \neq 0$ and $A > 0$, the quantity C will have a negative value if ω/ω_0 lies between $(c_4/c_3)(\sqrt{j}/\epsilon)$ and $\sqrt{(1 + c_2^2/c_3^2)(j/\epsilon^2)}$. Outside this range, we find that the quantity $C > 0$. Thus, it is seen that V_3^2 is finite and positive provided $C < 0$, that is, when

$$\min \left\{ \sqrt{\left(1 + \frac{c_2^2}{c_3^2}\right) \frac{j}{\epsilon^2}}, \frac{c_4}{c_3} \frac{\sqrt{j}}{\epsilon} \right\} < \frac{\omega}{\omega_0} < \max \left\{ \sqrt{\left(1 + \frac{c_2^2}{c_3^2}\right) \frac{j}{\epsilon^2}}, \frac{c_4}{c_3} \frac{\sqrt{j}}{\epsilon} \right\}.$$

Even for $A < 0$, one can show that the value of V_3^2 is finite and positive, provided $C < 0$. Thus, a wave propagating with phase speed V_3 exists only when $C < 0$. This means that the value of ω/ω_0 must lie between $(c_4/c_3)(\sqrt{j}/\epsilon)$ and $\sqrt{(1 + c_2^2/c_3^2)(j/\epsilon^2)}$ for the existence of a wave propagating with speed V_3 .

The quantity V_4^2 will be finite and positive for $A < 0$, that is, when $\omega < \sqrt{2}\omega_0$. Beyond this critical value of ω , a wave propagating with phase speed V_4 will degenerate into distance-decaying sinusoidal vibrations. Thus, we conclude that the nonlocality in an isotropic micropolar medium results in the wave speed V_3 behaving like the wave speed V_4 of local micropolar elasticity (see [Parfitt and Eringen 1969]), but oppositely/adversely.

The quantity V_3 is the speed of a set of coupled transverse waves and represents the transverse acoustic branch, while the quantity V_4 is also the speed of another set of coupled transverse waves and represents the transverse optic branch.

In the absence of nonlocality, all the phase speeds of longitudinal and transverse waves of a linear isotropic micropolar solid are recovered.

4. Reflection phenomena

Let $M = \{(x, z); -\infty < x < \infty, -\infty < z \leq 0\}$ be the region occupied by an isotropic nonlocal micropolar solid. Let $z = 0$ be the plane boundary surface of M that is assumed to be free from stresses. We discuss a two-dimensional problem in the x - z plane, so we take

$$\mathbf{u} = (u_1, 0, u_3), \quad \boldsymbol{\phi} = (0, \phi_2, 0), \quad \frac{\partial}{\partial y} \equiv 0.$$

From (14), we have

$$u_1 = q_{,x} - U_{2,z}, \quad u_3 = q_{,z} + U_{2,x}, \quad \phi_2 = \Pi_{1,z} - \Pi_{3,x},$$

where U_2 is the y -component of \mathbf{U} and Π_1 and Π_3 are the x and z -components of $\boldsymbol{\Pi}$.

Let a train of longitudinal displacement waves having amplitude A_0 and speed V_1 be made incident at an angle θ_0 on the free surface $z = 0$. We postulate the existence of the following reflected waves to satisfy the boundary conditions at the free plane surface:

- (i) a longitudinal wave of amplitude A_1 with speed V_1 , making an angle θ_1 with the normal,
- (ii) a set of coupled transverse waves of amplitude A_{3y} propagating with speed V_3 , making an angle θ_3 with the normal, and
- (iii) a similar set of coupled transverse waves of amplitude A_{4y} propagating with speed V_4 , making an angle θ_4 with the normal.

The complete geometry of the problem is shown in [Figure 1](#). Thus, the total wave field is given by

$$q = A_0 \exp\{ik_1(\sin \theta_0 x + \cos \theta_0 z) - i\omega_1 t\} + A_1 \exp\{ik_1(\sin \theta_1 x - \cos \theta_1 z) - i\omega_1 t\}, \quad (26)$$

$$U = \sum_{p=3,4} A_{py} \hat{e}_y \exp\{ik_p(\sin \theta_p x - \cos \theta_p z) - i\omega_p t\}, \quad (27)$$

$$\Pi = \sum_{p=3,4} (B_{px} \hat{e}_x + B_{pz} \hat{e}_z) \exp\{ik_p(\sin \theta_p x - \cos \theta_p z) - i\omega_p t\}, \quad (28)$$

where $\omega_l = k_l V_l$ ($l = 1, 3, 4$) have been defined earlier and \hat{e}_x , \hat{e}_y , and \hat{e}_z are the Cartesian unit base vectors along the x , y , and z directions, respectively.

Comparing the x and z components of (18) and then using (27) and (28), we obtain

$$B_p = \frac{i\omega_0^2}{k_p(c_4^2 + 2\omega_0^2/k_p^2 - V_p^2 - \epsilon^2\omega_p^2)} (\cos \theta_p \hat{e}_x + \sin \theta_p \hat{e}_z) A_{py}. \quad (29)$$

This gives us the relation between the coefficients A_p and B_p .

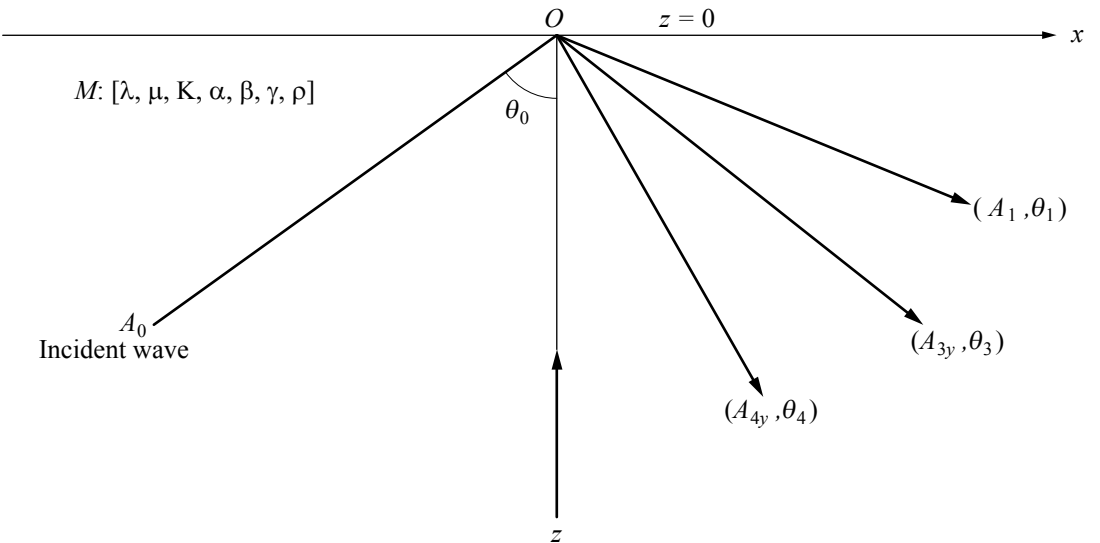


Figure 1. The geometry of the problem.

Since the boundary of the half-space M is mechanically stress-free, the appropriate boundary conditions are the vanishing of the force stress and the couple stress. Mathematically, these boundary conditions can be written as:

$$\sigma_{33} = \sigma_{31} = \mu_{32} = 0 \quad \text{at} \quad z = 0. \quad (30)$$

The requisite components of stresses are given by

$$\begin{aligned} \sigma_{33} &= \lambda' q_{,xx} + (\lambda' + 2\mu' + K') q_{,zz} + (2\mu' + K') U_{2,xz}, \\ \sigma_{31} &= (2\mu' + K') q_{,xz} + \mu' U_{2,xx} - (\mu' + K') U_{2,zz} - K' \phi_2, \quad \mu_{32} = \gamma' \phi_{2,z}. \end{aligned} \quad (31)$$

We shall also assume that at the boundary surface, all frequencies are equal, that is, $\omega_1 = \omega_3 = \omega_4 = \omega$, say, and Snell's law holds, which gives $k_1 \sin \theta_0 = k_1 \sin \theta_1 = k_3 \sin \theta_3 = k_4 \sin \theta_4$. The potentials given in (26)–(28) will satisfy the above boundary conditions (30) at $z = 0$, if

$$\sum_{p=0,1} [\lambda' + (2\mu' + K') \cos^2 \theta_p] k_1^2 A_p - (2\mu' + K') \sum_{p=3,4} \sin \theta_p \cos \theta_p k_p^2 A_{py} = 0, \quad (32)$$

$$\begin{aligned} &(2\mu' + K') \sin \theta_0 \cos \theta_0 k_1^2 A_0 - (2\mu' + K') \sin \theta_1 \cos \theta_1 k_1^2 A_1 \\ &- \sum_{p=3,4} \left[\mu' \cos 2\theta_p + K' \cos^2 \theta_p - K' \omega_0^2 k_p^{-2} \left(c_4^2 + \frac{2\omega_0^2}{k_p^2} - \epsilon^2 \omega_p^2 - V_p^2 \right)^{-1} \right] k_p^2 A_{py} = 0, \end{aligned} \quad (33)$$

$$\sum_{p=3,4} \gamma' \omega_0^2 \cos \theta_p k_p A_{py} \left(c_4^2 + \frac{2\omega_0^2}{k_p^2} - \epsilon^2 \omega_p^2 - V_p^2 \right)^{-1} = 0. \quad (34)$$

These equations enable us to provide the amplitude ratios of various reflected waves. Equations (32)–(34) can be written in matrix form as

$$[a_{ij}][Z] = [M], \quad (35)$$

where $[a_{ij}]$ is a 3×3 matrix, $[Z] = [Z_1, Z_3, Z_4]^t$ is a column matrix (where superscript t denotes the transpose), and $Z_1 = A_1/A_0$ and $Z_p = A_{py}/A_0$ ($p = 3, 4$) are the reflection coefficients. All the entries of the matrix $[a_{ij}]$ together with the column matrix $[M]$ are given in the [Appendix](#). Following [[Achenbach 1973](#)], the rate of energy transmission per unit area is given by

$$P^* = \sigma_{33} \dot{u}_3 + \sigma_{31} \dot{u}_1 + \mu_{32} \dot{\phi}_2. \quad (36)$$

The expressions of the energy ratios E_i ($i = 1, 3, 4$) corresponding to various reflected waves are

$$E_1 = -Z_1^2, \quad E_p = \frac{1}{P_1} \left[\mu' + K' - \frac{\omega_0^2}{k_p^2 D_p} \left(K' + \frac{\gamma' \omega_0^2}{D_p} \right) \right] k_p^3 \cos \theta_p Z_p^2, \quad p = 3, 4,$$

where $P_1 = -k_1^3 \cos \theta_0 (\lambda' + 2\mu' + K')$ and $D_p = c_4^2 + 2\omega_0^2/k_p^2 - \epsilon^2 \omega_p^2 - V_p^2$.

5. Numerical results and discussion

For a silicon crystal, the following values of the relevant parameters are taken for an isotropic nonlocal micropolar solid [[Zeng et al. 2006](#)]: $\lambda = 0.1055 \times 10^{13}$ dyne/cm², $\mu = 0.2518 \times 10^{12}$ dyne/cm², $K = 0.1 \times 10^{12}$ dyne/cm², $e_0 = 0.39$, $j = 9.21 \times 10^{-12}$ cm², $\rho = 2.330$ gm/cm³, $\gamma = 0.1423 \times 10^{13}$ dyne, and

$a = 0.5 \times 10^{-7}$ cm, while for a local micropolar solid, $\lambda = 0.7431 \times 10^{12}$ dyne/cm², $\mu = 0.1373 \times 10^{12}$ dyne/cm², $K = 0.1 \times 10^{12}$ dyne/cm², $j = 9.21 \times 10^{-12}$ cm², $\rho = 2.330$ gm/cm³, $\gamma = 0.1275 \times 10^{13}$ dyne, $a = 0.5 \times 10^{-7}$ cm, and $e_0 = 0$.

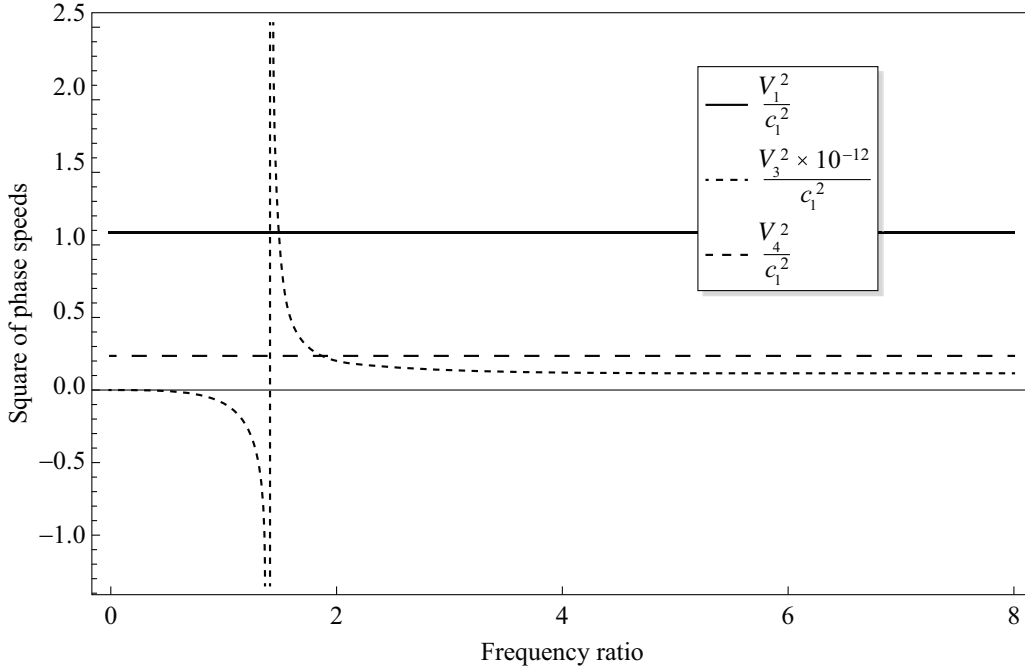


Figure 2. Variation of square of phase speeds V_i^2/c_1^2 ($i = 1, 3, 4$) with frequency ratio.

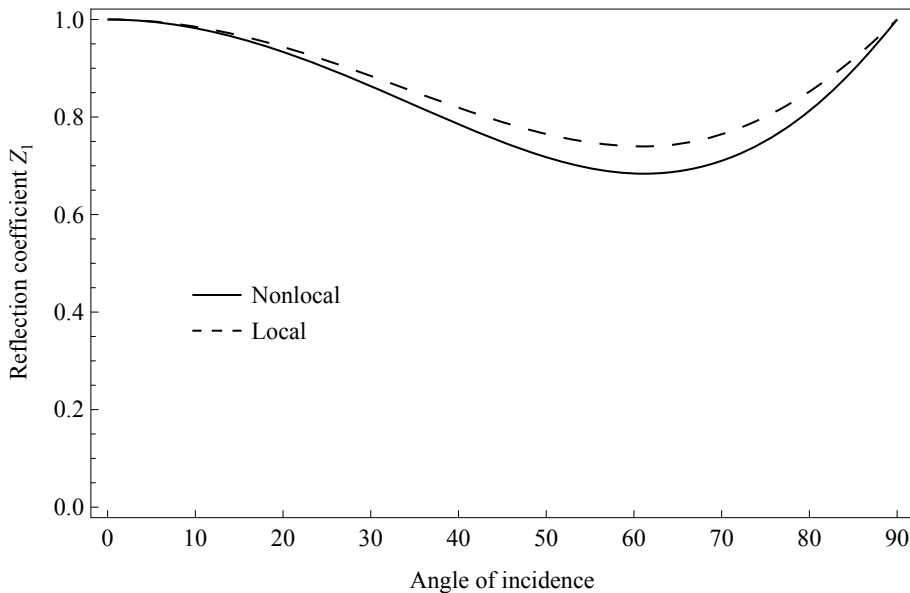


Figure 3. Variation of modulus of reflection coefficient Z_1 with angle of incidence.

In Figure 2, we have shown the variation of the square of phase speeds (nondimensional) V_i^2/c_1^2 ($i = 1, 3, 4$) in the nonlocal micropolar solid, with the frequency ratio (ω/ω_0). It is seen that the values of V_1^2/c_1^2 and V_4^2/c_1^2 remain almost constant in the considered range $0 \leq \omega/\omega_0 \leq 8$. We have plotted the curve of V_3^2/c_1^2 after magnifying it by a factor of 10^{-12} as its value was large enough in comparison

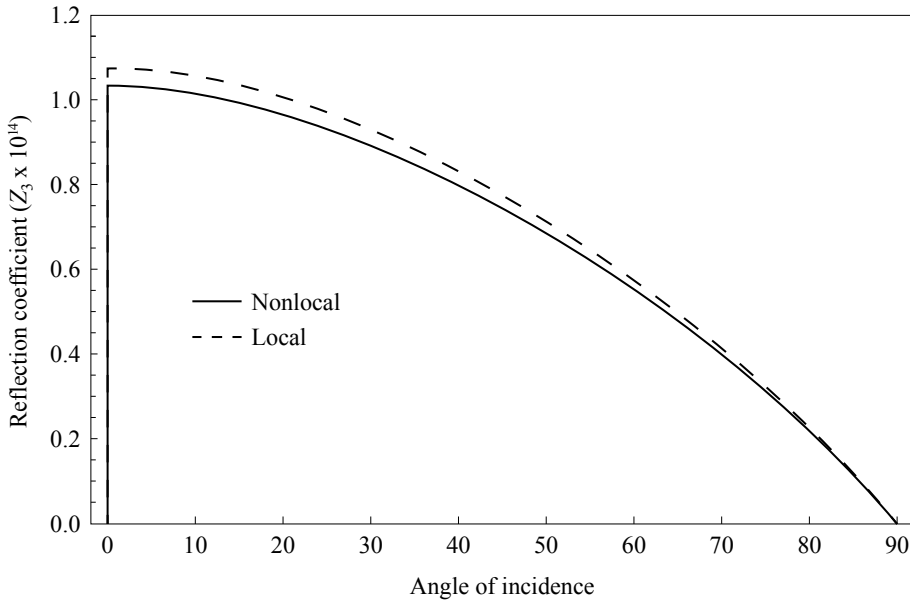


Figure 4. Variation of modulus of reflection coefficient Z_3 with angle of incidence.

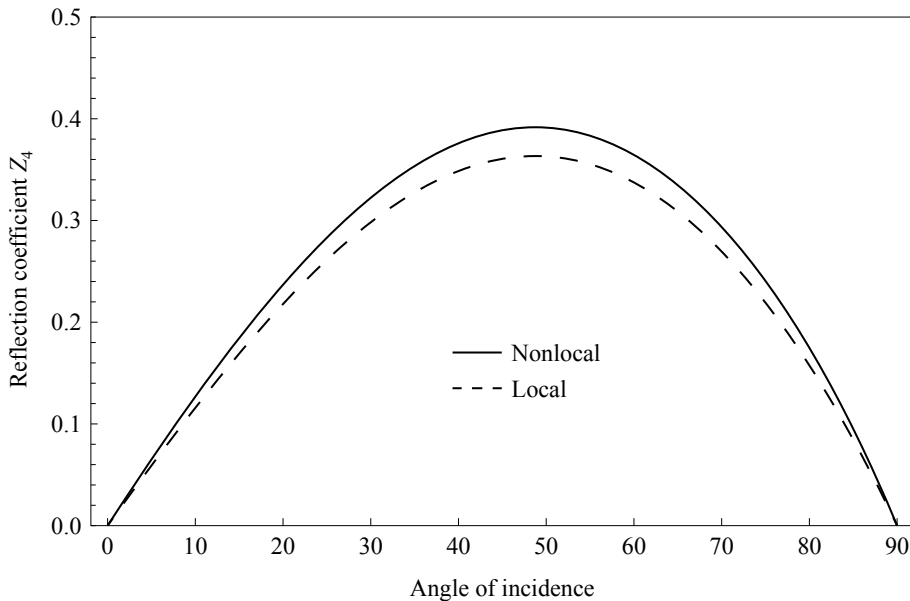


Figure 5. Variation of modulus of reflection coefficient Z_4 with angle of incidence.

with the values of other quantities. It can be seen through this figure that $\omega_c = \sqrt{2}\omega_0$ is the critical frequency for a wave propagating with phase speed V_3 , that is, before $\omega_c = \sqrt{2}\omega_0$ the quantity V_3^2/c_1^2 has negative values while later on it remains positive. Moreover, it has also been observed that the effect of the nonlocality parameter on phase speed depends heavily on the value of characteristic length a . At higher values of a , the phase speeds of waves are found to be more dispersive.

Figures 3–5 depict the comparison between the nonlocal and local micropolar solids for modulus values of reflection coefficients Z_1 , Z_3 , and Z_4 with angle of incidence of the longitudinal displacement wave propagating with phase speed V_1 . The solid curve is for the nonlocal micropolar solid, that is, when $e_0 = 0.39$, while the dotted curve is for the local micropolar solid.

In Figure 3, the modulus value of the reflection coefficient Z_1 has a maximum value equal to unity at normal incidence in both the cases. Then, its value decreases till $\theta_0 = 58^\circ$. Thereafter it increases with the increase of θ_0 to attain its maximum value at grazing incidence. The pattern is similar for the nonlocal micropolar solid and the local micropolar solid.

In Figure 4, we have plotted the variation of modulus values of the reflection coefficient $Z_3 \times 10^{14}$ as the value of Z_3 is negligibly small. The value of the reflection coefficient Z_3 is maximal at normal incidence. This value decreases with an increase of θ_0 throughout the range and approaches zero as θ_0 approaches 90° . Figure 5 depicts the variation of the absolute values of the reflection coefficient Z_4 . It is seen that the value increases with increase in θ_0 in the range $0^\circ \leq \theta_0 \leq 52^\circ$, and thereafter it decreases and vanishes at $\theta_0 = 90^\circ$.

In Figures 3–5, we have seen that at each angle of incidence the modulus value of the reflection coefficients Z_1 and Z_3 for the local micropolar solid is bigger than the corresponding values for the nonlocal micropolar solid. However, the value of Z_4 for the nonlocal micropolar solid is bigger at each angle of incidence than the value for the local micropolar solid.

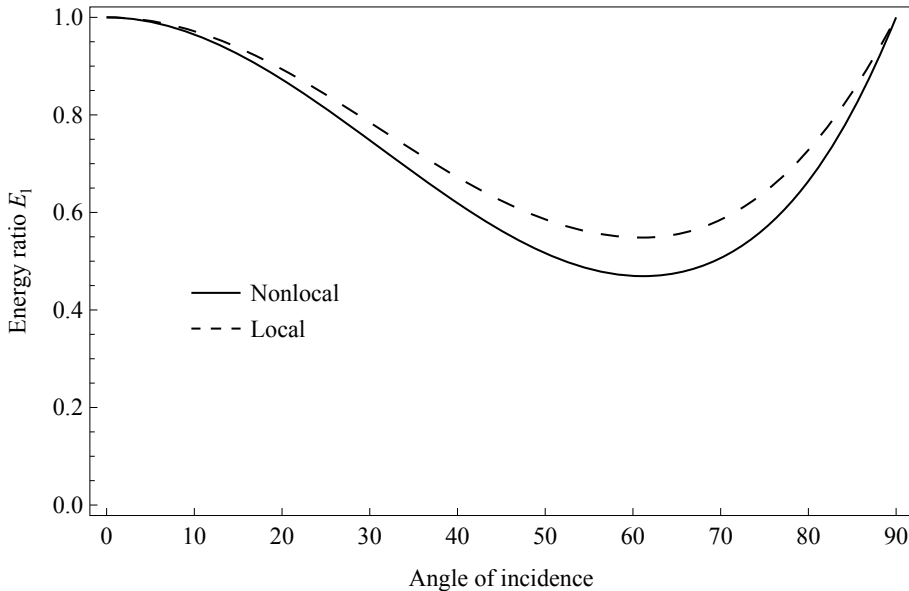


Figure 6. Variation of modulus of energy ratio E_1 with angle of incidence.

Figures 6–8 depict the variation of the modulus values of the energy ratios with the angle of incidence. At the free boundary surface, the sum of the energy ratios is equal to unity during reflection at each angle of incidence of a longitudinal displacement wave propagating with speed V_1 . The formulae for reflection coefficients and their corresponding energy ratios are obtained analytically and numerically. This shows that there is no dissipation of energy at the free boundary surface.

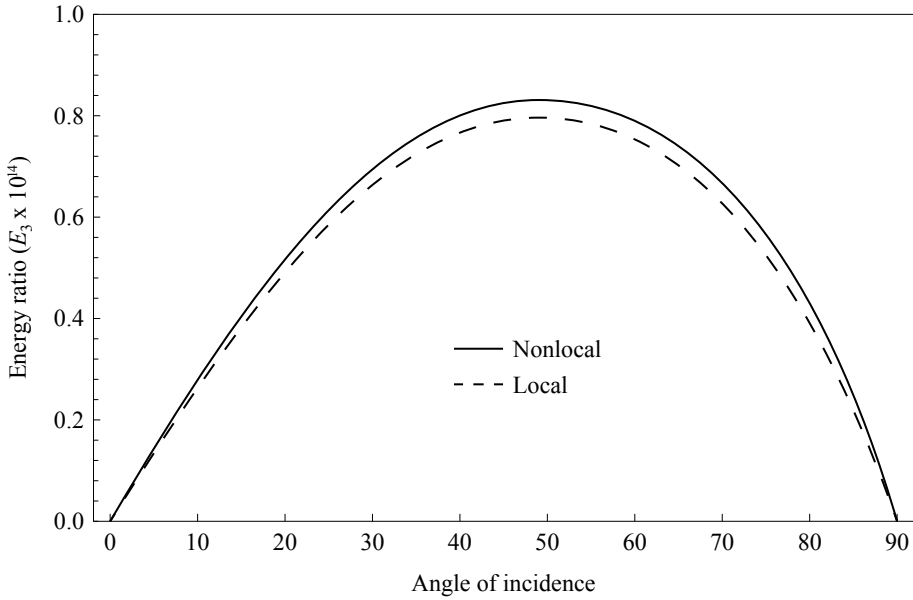


Figure 7. Variation of modulus of energy ratio E_3 with angle of incidence.

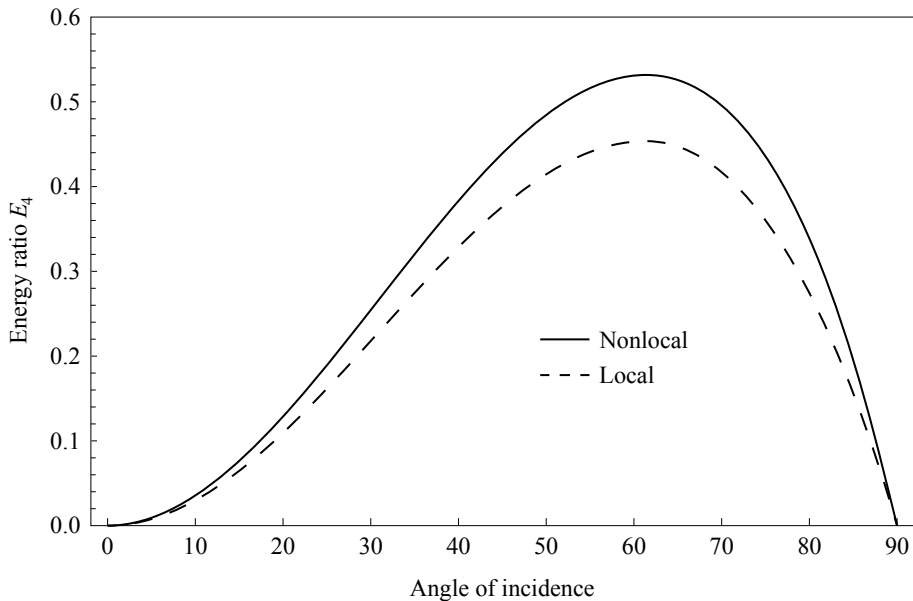


Figure 8. Variation of modulus of energy ratio E_4 with angle of incidence.

6. Conclusions

This paper deals with the possibility of plane-wave propagation in an isotropic nonlocal micropolar solid. The reflection phenomena of a plane wave striking obliquely at the free boundary surface is also discussed. The following is concluded.

- (i) Four waves may travel with distinct speeds in a nonlocal micropolar solid: a longitudinal displacement wave, a longitudinal microrotational wave, and two sets of coupled transverse waves. All the waves are dispersive in nature.
- (ii) The effect of the nonlocality parameter on the reflection coefficients (as well as on the energy ratios) is found to be maximal at some intermediate angle of incidence of a longitudinal displacement wave. However, there is no significant difference seen at the grazing incidence and the normal incidence on the reflection coefficients and energy ratios.
- (iii) The balance of energy law has been verified at each angle of incidence of a longitudinal displacement wave at the free boundary surface.

Appendix

Entries of the matrices $[a_{ij}]$ and $[M]$:

$$a_{11} = -1, \quad a_{12} = \frac{(2\mu' + K') \sin \theta_0}{[\lambda' + (2\mu' + K') \cos^2 \theta_0] v_{31}} \sqrt{1 - v_{31}^2 \sin^2 \theta_0},$$

$$a_{13} = \frac{(2\mu' + K') \sin \theta_0}{[\lambda' + (2\mu' + K') \cos^2 \theta_0] v_{41}} \sqrt{1 - v_{41}^2 \sin^2 \theta_0}, \quad a_{21} = \sin \theta_0 \cos \theta_0,$$

$$a_{22} = \frac{1}{(2\mu' + K') v_{31}^2} \left[\mu' (1 - 2v_{31}^2 \sin^2 \theta_0) + K' (1 - v_{31}^2 \sin^2 \theta_0) - \frac{K' \omega_0^2}{k_3^2 D_3} \right],$$

$$a_{23} = \frac{1}{(2\mu' + K') v_{41}^2} \left[\mu' (1 - 2v_{41}^2 \sin^2 \theta_0) + K' (1 - v_{41}^2 \sin^2 \theta_0) - \frac{K' \omega_0^2}{k_4^2 D_4} \right],$$

$$a_{31} = 0, \quad a_{32} = \frac{\Omega \sqrt{1 - v_{31}^2 \sin^2 \theta_0}}{2v_{31}^3 \left(1 + \frac{\epsilon^2 \omega_3^2}{V_3^2} - \frac{2\omega_0^2}{\omega_3^2} - \frac{c_4^2}{V_3^2} \right)}, \quad a_{33} = \frac{\Omega \sqrt{1 - v_{41}^2 \sin^2 \theta_0}}{2v_{41}^3 \left(1 + \frac{\epsilon^2 \omega_4^2}{V_4^2} - \frac{2\omega_0^2}{\omega_4^2} - \frac{c_4^2}{V_4^2} \right)},$$

$$M_1 = 1, \quad M_2 = \sin \theta_0 \cos \theta_0, \quad M_3 = 0,$$

$$\text{where } v_{31} = \frac{V_3}{V_1} \text{ and } v_{41} = \frac{V_4}{V_1}.$$

References

- [Achenbach 1973] J. D. Achenbach, "Plane harmonic waves in elastic half-spaces", Chapter 5, pp. 165–201 in *Wave propagation in elastic solids*, Applied Mathematics and Mechanics **16**, Elsevier, Amsterdam, 1973.
- [Chen et al. 2004] Y. Chen, J. D. Lee, and A. Eskandarian, "Atomistic view point of the applicability of microcontinuum theories", *Int. J. Solids Struct.* **41** (2004), 2085–2097.
- [Erbay et al. 1992] S. Erbay, H. A. Erbay, and S. Dost, "Nonlinear wave interactions in a micropolar elastic medium", *Wave Motion* **16** (1992), 163–172.

- [Eringen 1972a] A. C. Eringen, “Nonlocal polar elastic continua”, *Int. J. Eng. Sci.* **10** (1972), 1–16.
- [Eringen 1972b] A. C. Eringen, “Linear theory of nonlocal elasticity and dispersion of plane waves”, *Int. J. Eng. Sci.* **10** (1972), 425–435.
- [Eringen 1984] A. C. Eringen, “Plane waves in nonlocal micropolar elasticity”, *Int. J. Eng. Sci.* **22** (1984), 1113–1121.
- [Eringen 1999] A. C. Eringen, *Microcontinuum field theories, I: Foundations and solids*, Springer, New York, 1999.
- [Eringen 2002] A. C. Eringen, *Nonlocal continuum field theories*, Springer, New York, 2002.
- [Eringen and Edelen 1972] A. C. Eringen and D. G. B. Edelen, “On nonlocal elasticity”, *Int. J. Eng. Sci.* **10** (1972), 233–248.
- [Lazar and Kirchner 2006] M. Lazar and H. O. K. Kirchner, “The Eshelby tensor in nonlocal elasticity and in nonlocal micropolar elasticity”, *J. Mech. Mater. Struct.* **1** (2006), 325–337.
- [Najafi et al. 2012] A. Najafi, M. Eghtesad, and F. Daneshmand, “Boundary stabilization of vibration of nonlocal micropolar elastic media”, *Appl. Math. Model.* **36**:8 (2012), 3447–3453.
- [Parfitt and Eringen 1969] V. R. Parfitt and A. C. Eringen, “Reflection of plane waves from the flat boundary of a micropolar elastic half-space”, *J. Acoust. Soc. Am.* **45** (1969), 1258–1272.
- [Wang and Dhaliwal 1993] J. Wang and R. S. Dhaliwal, “On some theorems in the nonlocal theory of micropolar elasticity”, *Int. J. Solids Struct.* **30**:10 (1993), 1331–1338.
- [Zeng et al. 2006] X. Zeng, Y. Chen, and J. D. Lee, “Determining material constants in nonlocal micromorphic theory through phonon dispersion relations”, *Int. J. Eng. Sci.* **44** (2006), 1334–1345.

Received 11 Sep 2012. Revised 18 Oct 2012. Accepted 18 Nov 2012.

AARTI KHURANA: aarti_maths@yahoo.com

Department of Mathematics, DAV College, Sector 10, Chandigarh 160 011, India

SUSHIL K. TOMAR: sktomar66@gmail.com

Department of Mathematics, Panjab University, Sector 14, Chandigarh 160 014, India

SUBMISSION GUIDELINES

ORIGINALITY

Authors may submit manuscripts in PDF format online at the Submissions page. Submission of a manuscript acknowledges that the manuscript is original and has neither previously, nor simultaneously, in whole or in part, been submitted elsewhere. Information regarding the preparation of manuscripts is provided below. Correspondence by email is requested for convenience and speed. For further information, write to one of the Chief Editors:

Daive Bigoni bigoni@ing.unitn.it
Iwona Jasiuk ijasiuk@me.concordia.ca
Yasuhide Shindo shindo@material.tohoku.ac.jp

LANGUAGE

Manuscripts must be in English. A brief abstract of about 150 words or less must be included. The abstract should be self-contained and not make any reference to the bibliography. Also required are keywords and subject classification for the article, and, for each author, postal address, affiliation (if appropriate), and email address if available. A home-page URL is optional.

FORMAT

Authors can use their preferred manuscript-preparation software, including for example Microsoft Word or any variant of \LaTeX . The journal itself is produced in \LaTeX , so accepted articles prepared using other software will be converted to \LaTeX at production time. Authors wishing to prepare their document in \LaTeX can follow the example file at www.jomms.net (but the use of other class files is acceptable). At submission time only a PDF file is required. After acceptance, authors must submit all source material (see especially Figures below).

REFERENCES

Bibliographical references should be complete, including article titles and page ranges. All references in the bibliography should be cited in the text. The use of Bib \TeX is preferred but not required. Tags will be converted to the house format (see a current issue for examples); however, for submission you may use the format of your choice. Links will be provided to all literature with known web locations; authors can supply their own links in addition to those provided by the editorial process.

FIGURES

Figures must be of publication quality. After acceptance, you will need to submit the original source files in vector format for all diagrams and graphs in your manuscript: vector EPS or vector PDF files are the most useful. (EPS stands for Encapsulated PostScript.)

Most drawing and graphing packages—Mathematica, Adobe Illustrator, Corel Draw, MATLAB, etc.—allow the user to save files in one of these formats. Make sure that what you're saving is vector graphics and not a bitmap. If you need help, please write to graphics@mshp.org with as many details as you can about how your graphics were generated.

Please also include the original data for any plots. This is particularly important if you are unable to save Excel-generated plots in vector format. Saving them as bitmaps is not useful; please send the Excel (.xls) spreadsheets instead. Bundle your figure files into a single archive (using zip, tar, rar or other format of your choice) and upload on the link you been given at acceptance time.

Each figure should be captioned and numbered so that it can float. Small figures occupying no more than three lines of vertical space can be kept in the text (“the curve looks like this:”). It is acceptable to submit a manuscript with all figures at the end, if their placement is specified in the text by means of comments such as “Place Figure 1 here”. The same considerations apply to tables.

WHITE SPACE

Forced line breaks or page breaks should not be inserted in the document. There is no point in your trying to optimize line and page breaks in the original manuscript. The manuscript will be reformatted to use the journal's preferred fonts and layout.

PROOFS

Page proofs will be made available to authors (or to the designated corresponding author) at a Web site in PDF format. Failure to acknowledge the receipt of proofs or to return corrections within the requested deadline may cause publication to be postponed.

Numerical and experimental investigation of the dynamic characteristics of cable-supported barrel vault structures	SUN GUO-JUN, CHEN ZHI-HUA and RICHARD W. LONGMAN	1
When beam theories fail	PAUL R. HEYLIGER	15
Transient 3D singular solutions for use in problems of prestressed highly elastic solids	LOUIS MILTON BROCK	37
Wave velocity formulas to evaluate elastic constants of soft biological tissues	PHAM CHI VINH and JOSE MERODIO	51
Tubular aluminum cellular structures: fabrication and mechanical response	RYAN L. HOLLOMAN, VIKRAM DESHPANDE, ARVE G. HANSEN, KATHERINE M. FLEMING, JOHN R. SCULLY and HAYDN N. G. WADLEY	65
Reflection of plane longitudinal waves from the stress-free boundary of a nonlocal, micropolar solid half-space	AARTI KHURANA and SUSHIL K. TOMAR	95